Study of Thermal Power Plant Flexible Operation via Integration of Thermal and Compressed Air Energy Storage

by

Decai Li

A thesis submitted to the University of Warwick for the degree of

Doctor of Philosophy in Engineering

University of Warwick, School of Engineering

Nov 2019

Table of contents

List of Figures

List of Tables

Acknowledgements

I would like to express my thanks firstly to my parents for their love throughout all of my life.

I would like to express my gratitude to my supervisor Prof. Jihong Wang who guided me during my research, and I appreciate her patience and advice. Her encouragement and support were great motivation for me. I have benefited from each minute of discussion with Prof. Jihong Wang. The suggestions, criticisms and the guidance I received from her were valuable which made this thesis possible.

I am addressing my thanks as well to all the members in the Power and Control Systems Research Laboratory for their support and help.

I would like to acknowledge the support of the Engineering and Physical Research Council (EPSRC) for their support for the project - Flexible and Efficient Power Plant: Flex-E-Plant and also the grant support from EPSRC. I also thank the following partners for their the valuable contributions: GE Energy, Doosan Babcock Limited, Centrica plc., EDF Energy (West Burton Power) Limited., Uniper Technologies Limited, Goodwin Steel Castings Limited, NPL Management Limited, R-MC Power Recovery Limited., RWE Generation UK plc., Scottish and Southern Energy (SSE) plc., Siemens Industrial Turbomachinery, and TWI Limited. I wish to thank the China Scholarship Council (CSC) for the PhD scholarship.

Declarations

I hereby declare that the material in this thesis has not been submitted for a higher degree at any other university. This thesis entirely contains research work carried out by Mr Decai Li under the supervision of Professor Jihong Wang, unless references are given.

Some parts of this thesis were included in the following published papers:

Decai Li, Yukun Hu, Wei He, Jihong Wang, "Dynamic modelling and simulation of a combined-cycle power plant integration with thermal energy storage," in Automation and Computing (ICAC), 2017 23rd International Conference on, 2017, pp. 1-6.

Decai Li, Wenbin Zhang, Jihong Wang, "Flexible Operation of Supercritical Power Plant via Integration of Thermal Energy Storage," Power Plants in the Industry. InTech, 2018.

Decai Li, Jihong Wang, "Study of supercritical power plant integration with high temperature thermal energy storage for flexible operation," Journal of Energy Storage, vol. 20, pp. 140-152, 2018.

Decai Li, Yukun Hu, Dacheng Li, Jihong Wang, "Combined-cycle gas turbine power plant integration with cascaded latent heat thermal storage for fast dynamic responses," Energy Conversion and Management, vol. 183, pp. 1-13, 2019.

Decai Li

2019

Abstract

The utilisation of renewable energy sources for power generation has increased dramatically in the last decade. Due to the unpredictable feature of power generation from renewable energy sources, the high penetration of renewable energy greatly imposes the impact on power system reliability and stability as the balance of power generation and load demand becomes extremely challenging. Currently, the balance is mainly maintained by fossil-fuelled thermal power plants, especially, gas-fired power plants in the UK. In reality, almost all the thermal power plants are designed for base load but they are often required to operate as balance service plants, that is, they frequently change the generation and operation in order to follow the demand changes. This causes three main issues: low operation efficiency, low load factor and short lifetime.

The previous studies focused on the optimisation of control strategies to enhance the operational flexibility of power plants. This thesis explores the potential of integrating energy storage into power plants to achieve flexible operation. The key idea behind is to allow the power plant generation following the electrical load demand but having relatively stable thermal or mechanical energy generation. The main strategy is to integrate energy storage into the power plant energy conversion cycle to create an energy buffer before electricity generation. The thesis investigates the potential of integration of thermal energy storage (TES) with supercritical power plant water-steam cycle and the feasible thermal energy charging and discharging points; studies the strategies for integrating TES and adiabatic compressed air energy storage (A-CAES) with combined cycle gas turbine (CCGT) power plants; and examines the effects on flexible operation for both types of power plants while energy storage process is integrated.

The investigation of integration strategies for supercritical coal-fired power plant with TES is carried out by using a 600 MW power plant simulation platform named SimuEngine. Three TES charging strategies, and two TES discharging strategies are investigated. With the TES integration, the power plant could operate in the range of 520 MW to 644.4 MW under the condition of rated boiler heat generation.

Moreover, supercritical coal-fired power plant shows faster dynamic responses to the load demand variations and performs better in grid frequency control.

A 420 MW CCGT power plant dynamic model is developed in the software platform of Aspen Plus. The integration strategies of the CCGT power plant with TES or A-CAES are studied and presented by using Aspen Plus with the incorporation of FORTRAN subroutines. The dynamic simulation results demonstrate that the proposed integration strategies of the CCGT power plant with TES during the plant start-up, load-following and standby operations is technically feasible. With the TES integration, the steam turbine section could operate in the range of 66 MW to 143 MW, meanwhile, the gas turbine section is still running at the rated load condition. The operation flexibility of the CCGT power plant is significantly enhanced via A-CAES integration. The operation range of the CCGT power plant studied in this thesis is extended to 83-600 MW from 200-430 MW. A case study is carried out to illustrate how the CCGT power plant with A-CAES integration operates flexibly to smooth the gap between wind power generation and load demand.

Nomenclature

Symbols

A	Area
c_p	Heat capacity
$c_{p,l}$	Heat capacity of liquid phase
$c_{p,m}$	Heat capacity of metal
$c_{p,s}$	Heat capacity of solid phase
d	Diameter
D	Load response
e	Power generation
$\dot{E}$	Energy storage rate
$E_{kinetic}$	Kinetic energy
$\dot{E}_x$	Exergy change rate
f	Frequency/weighting factor
f_0	Norma grid frequency
$fuel$	Fuel supply
$fuel_n$	Normal fuel supply
G	Flow rate
h	Enthalpy
h_0	Reference enthalpy
h_{amb}	Heat transfer coefficient between cavern air and cavern wall
h_v	Volumetric convective heat transfer coefficient
H	Inertia constant/enthalpy
J	Inertia
k	Valve opening/heat conduction coefficient
k_s	Thermal conductivity
K	Heat dissipation coefficient
l	Enthalpy of phase change

m	Mass
$\dot{m}$	Mass flow rate
$\dot{m}_t$	Ratio of mass flow rate to its designed value
M	Mass
n	Polytropic exponent/molar flow rate
$\dot{n}_t$	Ratio of rotating speed to its designed value
N	Cells
P	Pressure
P_c	Compressor power
P_{gt}	Gas turbine power
P_{st}	Steam turbine power
P_{tot}	Total output power
$Power_i$	Power of the *i*-th generation unit
$Power_L$	Load demand
$Power_M$	Generated power
q	Heat generation
Q	Heat
$\dot{Q}$	Heat transfer rate
r	Flow resistance/radius
$r_0(k)$	Resistance factor when valve opening is k and temperature is 0^oC
r_{00}	Resistance factor when valve opening is 1 and temperature is 0^oC
R	Ideal gas constant
R_i	Droop constant of the *i*-th generation unit
s	Entropy
s_0	Reference entropy
S_i	Normal power of the *i*-th generation unit

S_{rated}	Nominal power rating
t	Time
T	Temperature
T_{amb}	Cavern wall temperature
T_i	Initial temperature
T_0	Reference temperature
u	Internal energy
U	Heat transfer coefficient
v	Velocity
V	Volume
V'	Specific volume
V_m	Molar volume
W	Work
z	Axial distance

Subscript/superscript

a	Atmosphere
c	Cold
com	Compressor
$cond$	Conduction
CND	Condensation section
da	Drain cooling to atmosphere
de	Drain water entrance
dl	Drain water outlet
DRN	Drain cooling section
DS	Superheat section
f	Final/fluid
h	Hot
i	Branch number/inlet/cell number
in	input

ideal	Ideal condition
lk	Leakage
m	Metal
o	Outlet
out	output
P	Point
pump	Pump
r	Rankine cycle
s	Shell side/steam
sat	Saturated
se	Steam entrance
steam	Steam turbine
tur	Turbine
w	Water
wa	Water to atmosphere
we	Water entrance
wl	Water outlet
0	Previous time step

Greek symbols

ρ	Density
η	Efficiency
η_c	Compressor efficiency
η_t	Turbine efficiency
Δ	Difference
ψ	Specific exergy
ω	Rotation speed
τ_a	Accelerating torque
τ_e	Electrical torque
τ_m	Mechanical torque

γ	Specific heat ratio
α	Fraction of the material experienced the phase change/ratio
θ	Angle
ε	Void fraction
β	Power loss coefficient

List of Abbreviations

A-CAES	Adiabatic Compressed Air Energy Storage
BES	Battery Energy Storage
CAES	Compressed Air Energy Storage
CCGT	Combined Cycle Gas Turbine
CFBC	Circulating Fluidized Bed Combustion
CHP	Combined Heat and Power
CLHS	Cascaded Latent Heat Storage
CSP	Concentrated Solar Power
ECO	Economizer
GB	Great Britain
HP	High Pressure
HPECO	High Pressure Economizer
HPEV	High Pressure Evaporator
HPSH	High Pressure Superheater
HPTB	High Pressure Turbine
HRSG	Heat Recover Steam Generator
HTF	Heat Transfer Fluid
IAPS	International Association for Properties of Steam
IGCC	Integrated Gasification Combined Cycle
IPECO	Intermediate Pressure Economizer
IPEV	Intermediate Pressure Evaporator
IPSH	Intermediate Pressure Duperheater
IPTB	Intermediate Pressure Turbine
LHS	Latent Heat Dtorage
LP	Low Pressure
LPECO	Low Pressure Economizer
LPEV	Low Pressure Evaporator
LPSH	Low Pressure Duperheater
LPTB	Low Pressure Turbine

NG	Natural Gas
PB	Packed Bed
PBS	Packed Bed Sensible
PCM	Phase Change Material
PCMs	Phase Change Materials
PHS	Pumped Hydro Storage
PRBM	Peng Robinson Boston Mathias
STEAMNBS	Steam National Bureau of Standards
RH	Reheater
SHS	Sensible Heat Storage
TES	Thermal Energy Storage

Chapter 1-Introduction

1.1 Background and Motivation

Global Warming is one of the grand challenges faced in this century. It is well recognised that CO_2 emission is a main contributor to the Global Warming. The UK government has set up an ambitious goal to reduce CO_2 emission by 100% by 2050. This is expected to be achieved by decarbonisation of power generation, transportation, and heating. In recent years, the rapid growth in electricity generation from clean renewable energy sources is evidenced. However, the unpredictable feature of power generation from renewable sources challenges the balance of power generation and load demand in power grid and it becomes more costly to match the generation and the demand constantly. If power industry operates the business as usual without making any changes, it will cause the whole electricity system to become unreliable and unsecure and it will no doubt limit the renewable energy penetration. Therefore, it is of foremost important to explore the potential solutions for future operation scenario of power grid in the UK and worldwide.

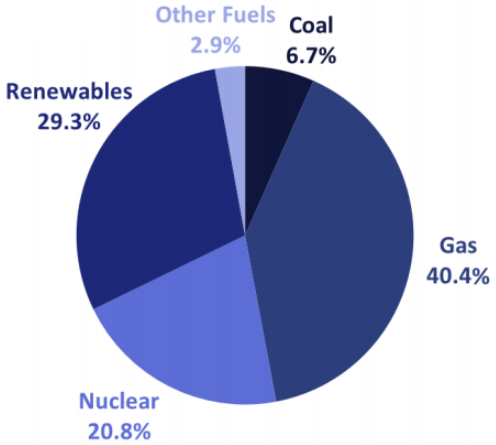

Figure 1.1: 2017 UK electricity generation by energy sources [1].

The shares of UK electricity generation by energy sources in 2017 is plotted in Figure 1.1. It can be seen that the most significant share of electricity is generated by natural gas followed by renewable energy, nuclear, coal and others. Whereas

renewable energies such as wind, solar, tidal and etc. are naturally intermittent and unpredictable. The current load balance in the UK is mainly managed by fossil-fuelled power plants, especially by nature gas-fired power plants. The power plants provide the balance service by regulating the generated power output in accordance with the dynamic changes in load demand. Therefore, although the fossil-fuelled power plants were designed to operate as base load power generation units, they are often required to work more flexibly, respond faster and more frequently start-up and shut-down. This causes several serious issues including low plant operation efficiency, low load factors and short lifetime.

Various technologies are under exploration and have the potential to offer the operational flexibility in response to the grid balance requirement, which can be from the supply side flexible generation, from the demand side management and from energy storage [2, 3]. The demand side management offers ancillary service to the grid by manipulating customers' electricity usage [4]. However, the load demand is difficult to predict and some load types are not schedulable, so the operational flexibility is difficult to achieve from the demand side management alone [3]. Energy storage systems have been used for peak shaving and load shifting in the past, mainly by pumped hydro power plants and a number of new energy storage facilities have recently been built by employing electrochemical battery technologies. Energy storage can provide ancillary services to the grid, such as primary and secondary frequency control reserves. The utilisation of energy storage technologies is limited at the current stage due to lack of technology maturity and uncertainties in cost benefit.

Although power generation from renewable energy increases rapidly, fossil-fuelled power plants would not be phased out soon and will be continuously playing its important role in balance service and maintaining the power grid reliability and stability. This motivated the research into solutions to enable those base load power plants to operate efficiently in flexible mode. This thesis proposes a new concept to integrate thermal or compressed air energy storage into the power plant thermal and mechanical cycle aiming to keep stable thermal or mechanical energy conversion with controllable electrical power output. The thesis reports the work in feasibility

study of the new concept and potential routes of implementation. The concept of the proposed method is shown in Figure 1.2, which illustrates the idea of extracting energy for storage during the off-peak period and discharging the stored energy for power generation to meet the peak demand. It is predicted that the combination of conventional power plants with energy storage not only improves plant dynamic performances, but also enhances energy storage economic gains. Besides, the operation mode of the independent energy storage power plant and the proposed hybrid power plant are shown in Figure 1.3 (a) and (b), respectively.

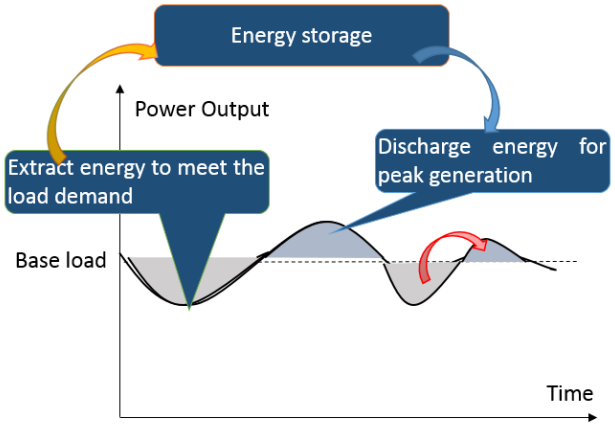

Figure 1.2: Concept of the proposed method.

Currently, most energy storage plants, such as pumped hydro and compressed air energy storage (CAES) power plant, operate on the concept shown in Figure 1.3 (a) [5], where the energy storage system is isolated from the traditional power plant. In the pumped hydro or CAES power plant, the energy undergoes a conversion from electrical energy to mechanical energy then potential energy during the charging process; the stored energy is used for later power generation during the discharging process. The proposed concept is to store the thermal or mechanical energy before they are converted to electrical energy and release the stored energy for power generation when needed, as shown in Figure 1.3 (b). It is predicted that the proposed concept could reduce the capital costs and improve the round trip efficiency while they work in flexible generation mode.

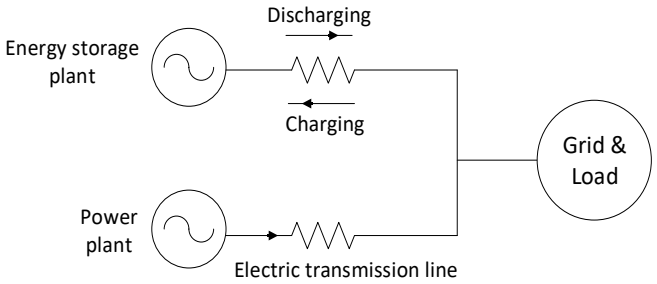

(a)

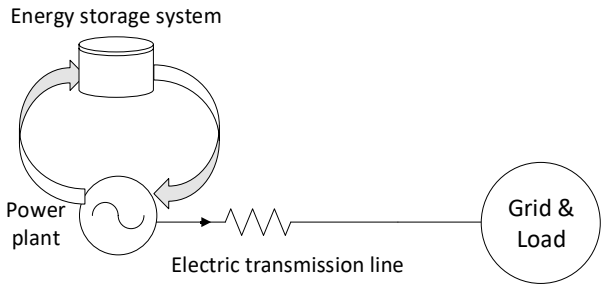

(b)

Figure 1.3: Load shifting through energy storage: (a) existing system; (b) proposed system.

Two types of fossil fuel power plants are studied: supercritical coal-fired power plant and combined-cycle gas turbine (CCGT) power plant. In technological consideration, thermal energy storage (TES) and CAES are selected and studied for integration with thermal power plants. The key factor is that energy storage is used as a buffer of the energy flow to achieve flexible operation.

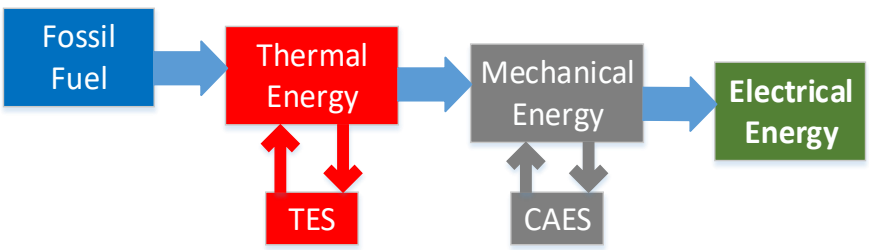

Figure 1.4: Thermal power plant power generation process.

The traditional thermal power plant generation process is shown in Figure 1.4. The first step of the process is to burn fossil fuel to get thermal energy, and the thermal energy is carried by high temperature and high pressure (HTHP) gas or steam. For gas turbine power plants, the HTHP gas is expanded and drives the gas turbine to generate the rotating torque, thus the thermal energy is converted into mechanical energy. For steam turbine power plants, the working fluid becomes superheated steam, so steam turbines are used. The turbine rotating torque drives a shaft which is connected to a generator for electricity generation, so the mechanical energy is converted into electrical energy. In summary, from fuel to electricity generation, the energy is released from combustion and undergoes conversion to thermal and mechanical energy. The thermal power plant dynamic response is relatively slow due to the significant time delay from the fuel supply, heat transfer to the water steam cycle [6]. In the proposed method, thermal energy storage and compressed air energy storage are investigated as the energy buffer. The energy storage unit can store the redundant or release the energy in various time periods when the grid required. Therefore, power plants could manipulate the stored energy for power output regulation without going through the power plant whole energy conversion process from fuel to electricity.

The PhD project conducts two types of power plant dynamic modelling and simulation study to investigate the feasibility of the proposed concept and feasible strategies for integrating energy storage into the thermal power plant energy conversion loop. It improves the understanding to potential influences or impact on power plants while energy storage is integrated in the required manner of charging or discharging energy.

1.2 Overview Energy Storage Technologies for Power System Operation

Pressured by challenges of climate change and energy security, many countries encourage increases in the share of renewable generation. However, high porting

of renewable energy brings the issue of balancing power supply and load demand. To address the challenge, various storage technologies have been implemented or studied for regulating the electricity generation. The most promising technologies include pumped hydro storage (PHS), CAES, TES and battery energy storage (BES).

PHS and CAES are two commercialised energy storage technologies which can offer over 100 MW power with a single unit [7]. Their flexibility and storage capacity enable them to improve grid stability and promote the development of renewable power generation [8, 9]. Currently, PHS power plants are widespread, and two commercialised CAES plants are in operation. These plants can be activated quickly releasing power reserves, to restore the rated frequency of the grid. In addition to the independent power plant, combination with other power sources is another utilisation of PHS and CAES. With the PHS and CAES integration, the plant performance and flexibility are enhanced, especially renewable plants. PHS has been proposed for combination with solar and wind system to mitigate the fluctuation of renewable sources to match the grid requirement [10, 11]. On the other hand, the integration of CAES and wind system has been extensively studied, it is shown that the hybrid system can generate smooth power output under fluctuating wind conditions [12].

The energy storage in the form of the thermal energy has been considered as a mature technology. It has been adopted by thermal power plants to enhance their flexibility, such as solar thermal power plants [13] and combined heat and power (CHP) plants [14]. The simulation study of conventional fossil fuel power plant integration with TES has attracted a lot of researchers' attention [15, 16]. In thermal power plants, the TES system acts as the buffer between the power sources and outputs, allowing the alignment of power or heat generation with the load demand.

Compared with most other types of commercially energy storage technologies, BES has the merits of high energy density, better round-trip efficiency and fast response ability; however they are relatively expensive and immature in large-scale application [17]. All these features determine the role of batteries in power system.

BES systems are able to activate on a millisecond timescale to fast balance the power generation and consumption [18]. Therefore, BES systems can be used to provide primary reserve and then quickly stabilise grid frequency at a certain level, which is called primary frequency control. Apart from short-term primary frequency control, the long-term peak shaving is also an important application of BES systems. For the generator, the capability of black-start is obtained via the support of BES [19]. In addition to all applications mentioned above, integration with renewable generation is a promising application for the BES system. The main concerns and uncertainties are from battery end life disposal and recycling, which remains a challenging unsolved big issue. It is still unknown whether it is a sustainable technology for power systems.

In summary, energy storage is a key enabling technology for the balance of power generation and load consumption. The energy storage systems can either operate independently or coupled with other power generation process. To make energy storage economically viable and technologically competitive, more research effort is needed.

1.3 Research Objectives

The project is proposed to investigate the potential solutions for thermal power plant flexible operation to allow more renewable energy integration. The goal will be realised by achieving the following objectives:

- to study supercritical coal-fired power plant integration with TES for flexible plant operation. A 600 MW supercritical coal-fired power plant simulation platform called SimuEngine will be used to investigate whether it is feasible to integrate the TES with the power plant water-steam cycle. The project needs to determine suitable thermal energy extraction locations, to find out how the energy stored can be discharged back to the power generation process, and to identify the dynamic performance of the power plant during the TES charging and discharging processes.

- to develop a combined-cycle gas turbine (CCGT) power plant dynamic model by using a commercial software, Aspen Plus.
- to investigate the integration strategy for the CCGT power plant with TES. The dynamic simulation study of the CCGT power plant and TES will be conducted to identify the influences of TES charging and discharging processes on the plant dynamic performances.
- to examine the feasibility of the CCGT power plant integration with adiabatic compressed air energy storage (A-CAES). The integration strategy for a CCGT power plant and A-CAES will be explored to improve the operational flexibility of the plant.
- to study how the CCGT power plant flexible operation supports renewable power generation with the help of A-CAES integration.

1.4 Thesis Organization

The thesis is organized into seven chapters.

Chapter 1 gives the introduction to the motivations and objectives. The thesis structure is presented in the chapter.

Chapter 2 reviews the technology and operation of coal-fired and gas-fired power plants. Energy conversion theory of coal-fired and gas-fired power plants is described in the chapter. Then an overview of thermal power plant flexible operation is given.

Chapter 3 reports the work on study of supercritical coal-fired power plant integration with TES for flexible operation. The simulation software named SimuEngine is adopted and a 600 MW supercritical coal-fired power plant model is implemented into the software platform. Three TES charging strategies and two TES discharging strategies are proposed and verified via the simulation study. Further study is conducted to investigate how the TES integration can help the plant operation to provide better support to the power grid frequency control.

Chapter 4 develops a dynamic mathematical model of a 420 MW CCGT power plant. Aspen Plus is used to develop the triple-pressure CCGT power plant model which is the prototype of Chapter 5 and 6 study. The mathematical descriptions of the individual sub-model are presented, which includes a compressor, combustion chamber, gas turbine, heat exchanger, steam turbine, etc. Moreover, a novel method is proposed to conduct whole system dynamic simulation in Aspen Plus by an external FORTRAN subroutine.

Chapter 5 investigates the integration strategy for the CCGT power plant with TES. The mathematical model of the designed cascaded latent heat storage (CLHS) system is introduced. The integration strategies of the CCGT power plant with CLHS are investigated during the plant start-up, load-following, and plant standby operations. Meanwhile, the dynamic simulation results of the CCGT power plant and CLHS are presented and analysed for the different working conditions.

Chapter 6 provides research on the integration strategy for the CCGT power plant and A-CAES. The mathematical models of the designed TES system and air cavern are introduced. The A-CAES charging and discharging strategies are introduced, and the A-CAES charging and discharging mass flow rate is optimised by the Genetic Algorithm for various load conditions. This chapter also presents a case study to show how the hybrid system flexible operation supports wind power generation. Furthermore, the dynamic simulation results of the CCGT power plant, TES and cavern air are presented and analysed.

Chapter 7 summarise the PhD work and the future research directions are recommended.

1.5 Prizes and Publications

Publications and prize during this period are presented as follows.

Prize:

Decai Li, Jihong Wang, “Study of Fossil-fuel Plant Integration with HTTS for Efficient and Flexible Operation” IET Midlands Power Group Prize Award Evening, University of Warwick, 2017 (**Best Poster Prize Award given**).

Conference Paper:

Decai Li, Yukun Hu, Wei He, Jihong Wang, "Dynamic modelling and simulation of a combined-cycle power plant integration with thermal energy storage," in Automation and Computing (ICAC), 2017 23rd International Conference on, 2017, pp. 1-6.

Book Chapter:

Decai Li, Wenbin Zhang, Jihong Wang, "Flexible Operation of Supercritical Power Plant via Integration of Thermal Energy Storage," Power Plants in the Industry. InTech, 2018.

Journal Paper:

Decai Li, Jihong Wang, "Study of supercritical power plant integration with high temperature thermal energy storage for flexible operation," Journal of Energy Storage, vol. 20, pp. 140-152, 2018.

Decai Li, Yukun Hu, Dacheng Li, Jihong Wang, "Combined-cycle gas turbine power plant integration with cascaded latent heat thermal storage for fast dynamic responses," Energy Conversion and Management, vol. 183, pp. 1-13, 2019.

Co-author Paper:

Xing Luo, Jihong Wang, Jacek D Wojcik, Jianguo Wang, **Decai Li**, Mihai Draganescu, Yaowang Li, Shihong Miao, "Review of Voltage and Frequency Grid Code Specifications for Electrical Energy Storage Applications," Energies, vol. 11, pp. 1-26, 2018.

Xing Luo, Mark Dooner, Wei He, Jihong Wang, Yaowang Li, **Decai Li**, Oleh Kiselychnyk, "Feasibility study of a simulation software tool development for dynamic modelling and transient control of adiabatic compressed air energy storage

with its electrical power system applications," Applied Energy, vol. 228, pp. 1198-1219, 2018.

Chapter 2-Introduction to Coal-fired and Gas-fired Power Plants and Their Operation

2.1 Introduction

Coal is currently a dominating fossil fuel for electricity generation in thermal power plant technology and it is relatively an abundant resource on the planet. In 1867, Werner von Siemens developed the first dynamo machine in the world and placed the landmark of the technology in history [20]. Thomas Edison set up the first coal fired central power plant in New York, in 1882 [21], in which one stage of coal-fired steam generator produced low-pressure saturated or slightly superheated steam to power a steam engine then to drive a DC generator [22]. Introduction of AC generator technology by Nicola Tesla provides a new way to enlarge the power of central power stations [23]. The pulverised coal firing technology became so developed, in the 1920s [24]. The technology increased combustion temperature and then improved thermal efficiency and lower the requirement for excess air for combustion [24].

In the 1970s, the subcritical pressure power plants, operating at 120-220 bar [25], were the dominant type of thermal power plant with a thermal efficiency around 35%. After that supercritical pressure power plants were established, operating at around 250 bar [25], which increases thermal efficiency up to 42%. Twenty years later, more efficient ultra-supercritical pressure power plants appeared, operating at around 300 bar [25], which brings the efficiency of coal-fired power plant to over 45% [26].

Natural gas (NG) is the second important fossil fuel for thermal power generation. It has been used as a source for generating electricity since the early part of the 20th century [27]. In the 21st century, gas turbine based power plants became one of the mainstays in power generation industry due to their advantage in flexible operation so they can be activated quickly to provide power reserves [28].

The first gas turbine which is able to produce more power more than the power required to drive its own components was manufactured in 1903 by Aegidius Elling [29]. After 36 years technology development until 1939, the first practical gas turbine used for electricity generation was installed at Neuchatel, Switzerland, which belongs to the Swiss company BBC Brown Boveri [30]. The exploitation of utilisation of gas turbines in power generation started during the 1970s and early 1980s, which was motivated by its capability in providing the services for standby and peak power support on power grid [31]. Now gas turbines in simple open cycle configuration can reach 46% efficiency [32].

With the technology process, combined-cycle gas turbine (CCGT) technology started maturing. CCGT power plants contain two steps of energy production combining two different energy producing cycles. In the first step, electricity is produced using a gas turbine to spin the shaft directly to an attached generator. The exhaust exits the gas turbine still has plenty of energy to utilise, this energy is used to power the second step of electricity generation via a heat recovery steam generator. The first CCGT power plant was installed at the Belle Isle Station, Oklahoma, the United States in 1949 by GE [30]. Initial applications of CCGT power plants were limited since the gas turbine itself was still a novel technology in the 1950s; moreover, the unit power was not sufficient to compete with steam turbines. During the early 1980s, the CCGT power plants started to become attractive to power companies and were adopted widely for electricity generation. With decades of technology development, the efficiency of the CCGT power plant is now in excess of 60% [33]. Thus, the CCGT power plants have promoted natural gas to become the second most important fossil fuel for power generation after coal [27].

This chapter introduces the coal-fired and gas-fired power plants and their operation. It starts with describing the coal-fired and gas-fired power generation processes and the energy conversion principles. Then an overview of thermal power plant flexible operations is presented.

2.2 Coal-fired Power Plants

2.2.1 Traditional Coal-fired Power Plants

The traditional technology of generating electricity from coal is to burn pulverised coal in air, and the released heat is captured to produce steam in a boiler. The steam is fed into a steam turbine that drives a generator to generate electricity. The schematic of a pulverised coal-fired power station is shown in Figure 2.1.

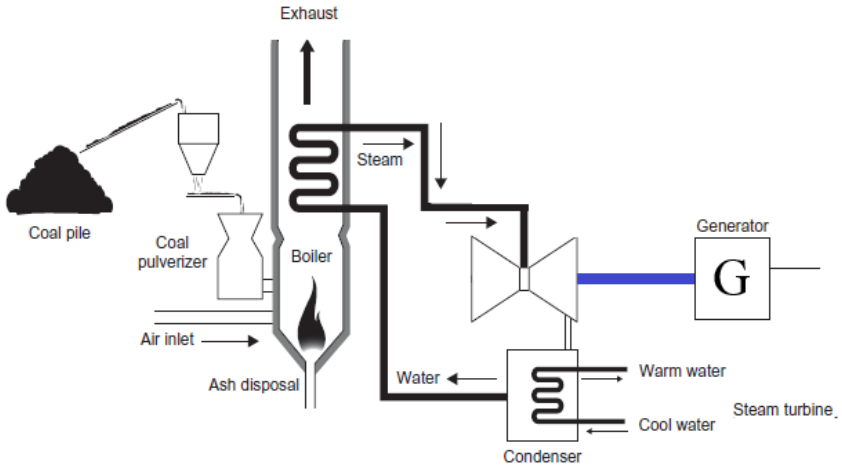

Figure 2.1: Schematic of a pulverised coal-fired power plant [34].

It can be seen from Figure 2.1 that the coal from the storage is transmitted to the pulveriser for grinding. The pulverised coal is mixed with air to be blown to the furnace for combustion in a boiler, releasing chemical energy as heat. The heat released from the combustion is captured by feed water within tubes in the boiler, the water is then converted into steam. The produced steam is carried to a steam turbine converting the energy stored in the steam to mechanical energy that spins a generator. The exhaust steam then enters condenser where it is condensed to water by cooling water, finally the condensed water is fed to the boiler to start a new cycle.

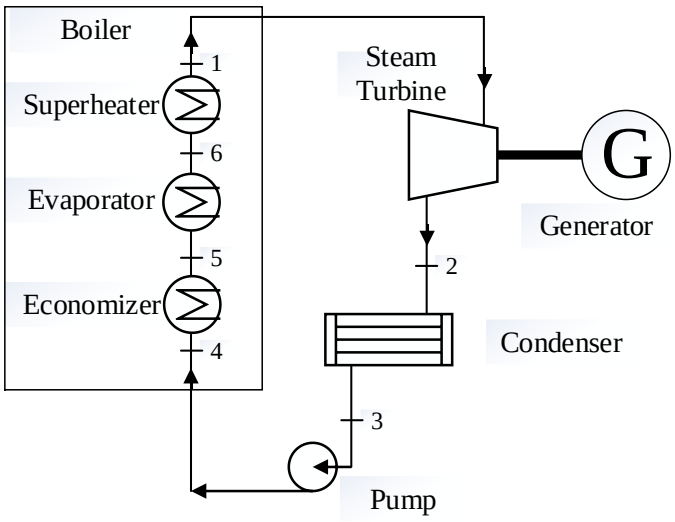

Figure 2.2: Ideal Rankine cycle configuration [35].

A typical system configuration of the Rankine cycle is shown in Figure 2.2. There are four main components involved in a Rankine cycle: pump, boiler, turbine, and condenser. To begin with, the feed water is pumped into the boiler by the feed water pump. Then, the feed water is heated into superheated steam while passing through the economiser, evaporator and superheater. The produced steam expands in the steam turbine by an adiabatic process. The exhaust steam is then condensed to water in the condenser for the next cycle.

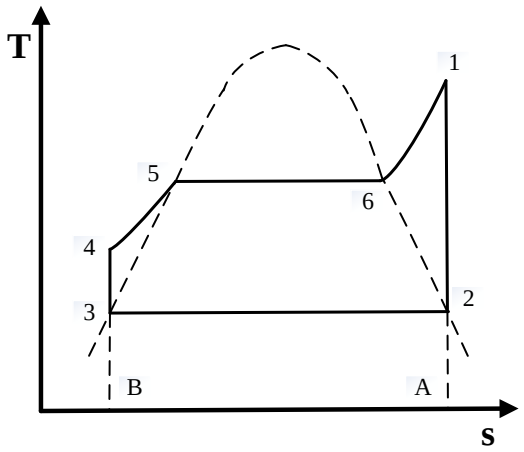

Figure 2.3: T-s diagram for subcritical Rankine cycle.

The T-s diagram of a subcritical Rankine cycle is shown in Figure 2.3. For ideal Rankine cycle, the pump and turbine are assumed to be isentropic, and the boiler and condenser are not involved in doing any work. The pump raises the feed water pressure isentropically from position 3 to position 4. Then the feed water flows into boiler where the water is converted into superheated steam via economizer (position 4 to 5), evaporator (position 5 to 6) and superheater (position 6 to 1), as shown in Figure 2.2 and Figure 2.3. The superheated steam expands through a steam turbine at constant entropy from position 1 to position 2. Finally, the exhaust steam is condensed to water from position 2 to position 3. Therefore, the energy balance equations for each component can be described as follows.

The pump required work (W_{pump}) is given by:

$$W_{pump} = h_4 - h_3, \tag{2.1}$$

where, h is the enthalpy and subscript of the enthalpy is the position in Figure 2.2 and 2.3.

The net heat added (Q_{in}) is given by:

$$Q_{in} = h_1 - h_4. \tag{2.2}$$

The steam turbine work (W_{steam}) is:

$$W_{steam} = h_1 - h_2. \tag{2.3}$$

The condenser discharged heat (Q_{out}) is:

$$Q_{out} = h_2 - h_3. \tag{2.4}$$

Therefore, the efficiency of the ideal Rankine cycle is:

$$\eta_r = \frac{W}{Q} = \frac{(h_1 - h_2) - (h_4 - h_3)}{(h_1 - h_4)}. \tag{2.5}$$

It can be seen that the efficiency is the ratio of the area 3-4-5-6-1-2 and the area B-4-5-6-1-A in Figure 2. 3. Therefore, increasing the temperature and pressure of the

steam expects to improve the cycle efficiency, which leads to the concept of the supercritical power plant which is introduced in the next section.

2.2.2 Supercritical Power Plants

Supercritical power plant operates at higher temperature and pressure than those traditional (subcritical) coal-fired power plants, leading to higher efficiency and lower emissions. Supercritical is a state of substance where there is no clear distinction between the liquid and the gaseous phase. The water reaches supercritical state when the temperature is above 374.15 ℃, and the pressure is above 22.1s MPa. The T-s diagram of a supercritical cycle is shown in Figure 2.4. A pump raises the feed water pressure isentropically from position 3 to position 4. The feed water flows into boiler where the water is converted into superheated steam from position 4 to position 1. Same as subcritical cycle, the superheated steam expands through a steam turbine at constant entropy from position 1 to position 2. Finally, the exhaust steam is condensed to water from position 2 to position 3.

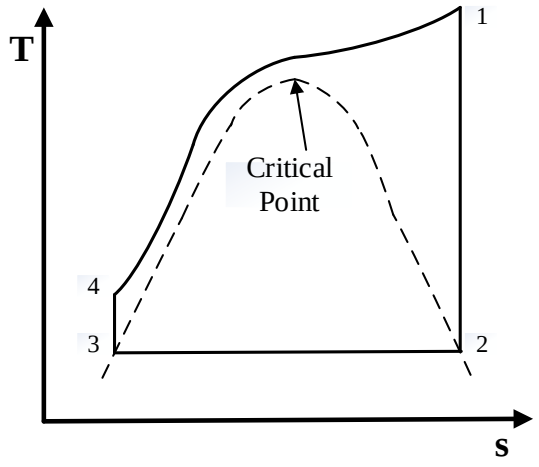

Figure 2.4: T-s diagram of a supercritical cycle.

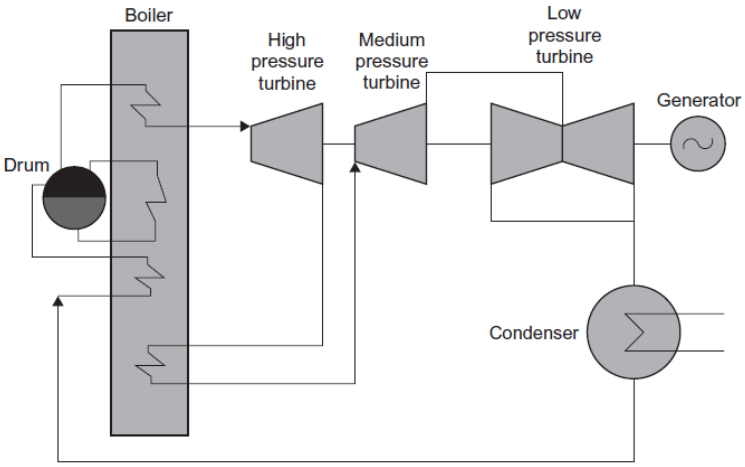

(a)

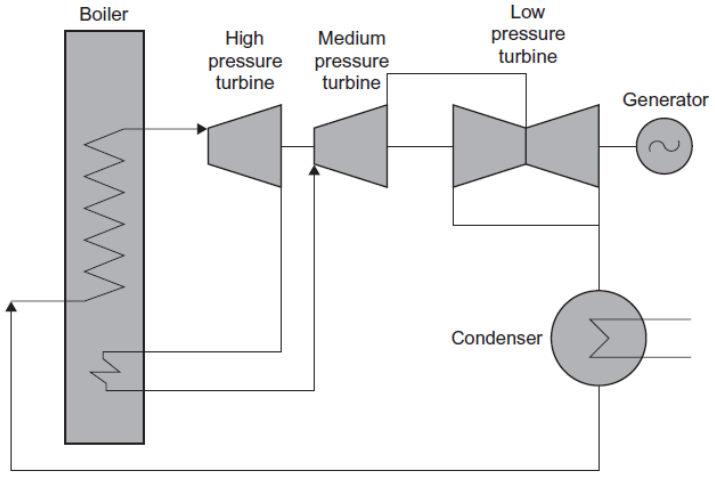

(b)

Figure 2.5: Coal-fired power plant boiler system: (a) subcritical steam cycle; (b) supercritical steam cycle [34].

In the supercritical boiler, the water becomes indistinguishable from steam, which is the supercritical state. The natural circulation cannot be formed under the supercritical condition; therefore, the once-through boiler is employed by the supercritical power plant. There is no steam drum in the once-through boiler, which is the main structural difference between the once-through boiler and natural circulation boiler, as shown in Figure 2.5. The main advantage of a supercritical once-through boiler is that it operates more efficiently than a subcritical boiler that has to recirculate water in the process of producing steam. Although the

supercritical boiler tends to be cheaper to operate, they are more expensive to build and maintain since special materials are needed to withstand the supercritical temperature and pressure.

2.2.3 Circulating Fluidised Bed Combustion Power Plants

Circulating fluidised bed combustion (CFBC) is an alternative to pulverised coal combustion for power generation. In the CFBC boiler, crushed coal, limestone, and ash are mixed in the bed levitated by the incoming combustion air. The schematic of a CFBC power plant is shown in Figure 2.6.

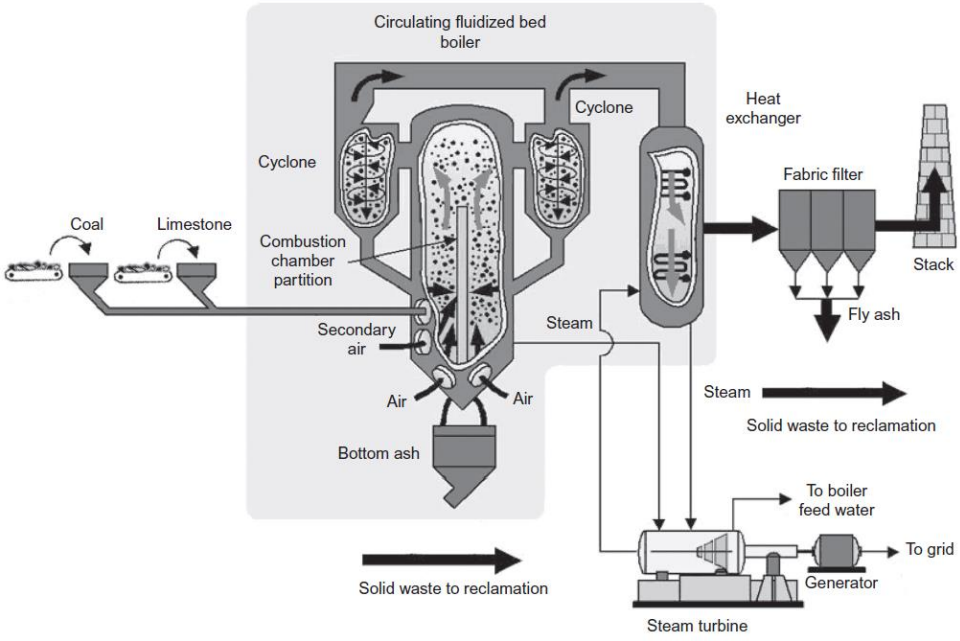

Figure 2.6: Schematic of circulating fluidized bed power plant [34].

The combustion temperature in the circulating fluidised bed combustion boiler (800-900 ℃) is significantly lower than in the pulverised coal combustion boiler (1300-1700 ℃), which results in fewer nitrogen oxides emission [36, 37]. Moreover, the majority of sulfuric in the coal can be captured by limestone that is injected into the furnace, which leads to significantly reduced sulfur dioxide emission [36].

2.2.4 Integrated Coal Gasification Combined Cycle Power Plants

An integrated gasification combined cycle (IGCC) is a technology that uses hydrocarbon fuels to produce electrical power in a clean and more efficient way via gasification, compared with direct combusting the fuels. In IGCC power plant, a high pressure gasifier is used to turn coal and other carbon based fuels into pressurized gas-synthesis gas (syngas). It can then remove impurities from the syngas prior to the power generation cycle. The schematic of an IGCC power plant is presented in Figure 2.7.

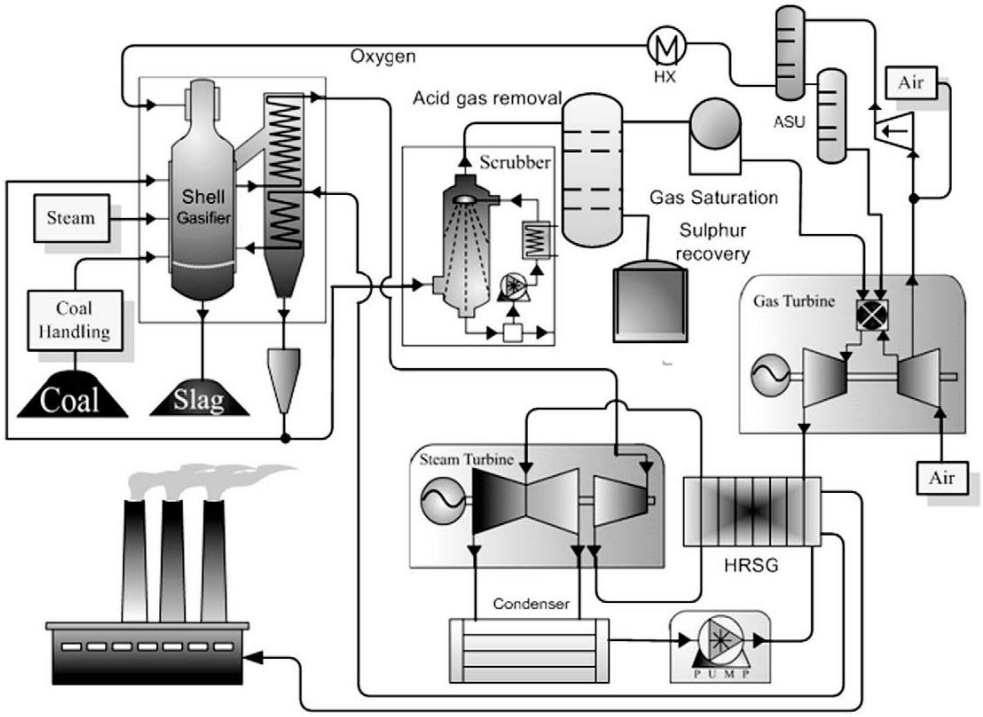

Figure 2.7: Flow diagram of an IGCC power plant [38].

There are numerous advantages of IGCC technology, high thermal efficiency (up to 45%), low particulate matter, nitrogen oxides, and sulfur dioxide emission, which are making it marketable [39]. However, the capital cost is much higher than the pulverised coal-fired power plant and its economic viability is still not clear.

2.3 Gas turbine and CCGT Power Plants

2.3.1 Gas Turbine Power Plants

The gas turbine contains three main components: a compressor, a combustion chamber, and a turbine. The schematic diagram of a gas turbine power plant is shown in Figure 2.8. Air is compressed through a multiple precision fan blades and then mix with natural gas in the combustion chamber for combustion. The hot combustion gas expands in the gas turbine, which forms a Brayton cycle. In a standard design, the compressor, turbine and generator are mounted on the same shaft. Therefore the turbine must produce enough power to drive both the compressor and generator.

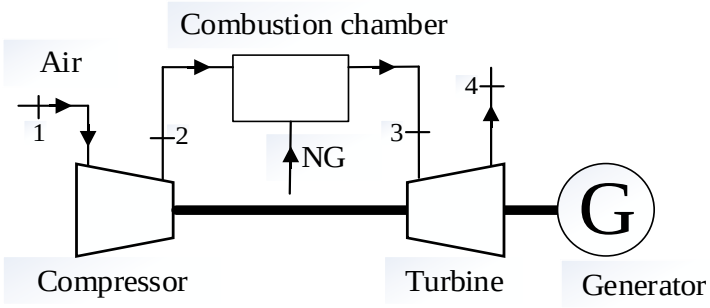

Figure 2.8: Schematic of a gas turbine cycle.

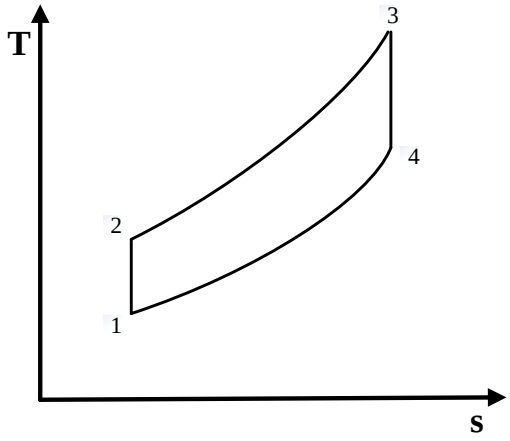

Figure 2.9: Gas turbine T-s diagram.

The ideal gas turbine cycle (Brayton cycle) T-s diagram is shown in Figure 2.9. The cycle comprises two isentropic and two isobaric processes. The compressor raises the air pressure isentropically from position 1 to position 2. Then the compressed air flows into the combustion chamber where the natural gas is burned, and the air is heated from position 2 to position 3 isobarically. The heated gas expands through a turbine at constant entropy from position 3 to position 4. Finally, the exhaust gas is cooled at constant pressure from position 4 to position 1. The work and heat transfers of each component can be expressed as follows.

Work input to compressor (W_{com}) is:

$$W_{com} = h_2 - h_1 , \tag{2.6}$$

where, h is the enthalpy and the subscript of enthalpy is the position in Figure 2.8 and 2.9.

Work output from turbine (W_{tur}) is:

$$W_{tur} = h_3 - h_4 . \tag{2.7}$$

The heat supplied to the cycle (Q_{in}) is:

$$Q_{in} = h_3 - h_2 . \tag{2.8}$$

Thus, the gas turbine cycle efficiency (η) is:

$$\eta = \frac{W_{tur} - W_{com}}{Q_{in}} . \tag{2.9}$$

2.3.2 CCGT Power Plants

When a power plant relies on a single Brayton cycle, the heat left over in the exhaust gas is substantial, which results in poor thermal efficiency of the gas turbine plant. For a large gas turbine based power plant, a steam turbine bottoming cycle is worth adding to the plant to improve plant efficiency. Instead of using a single thermodynamic cycle to convert fossil fuel to electricity, the combined-cycle plant

uses more than one cycle. The basic combined-cycle configuration consists of a gas turbine, a heat recovery steam generator (HRSG) and a steam turbine. The schematic of a CCGT power plant is shown in Figure 2.10. The gas exhausted from the gas turbine is hot enough for the HRSG to capture the heat to raise steam temperature, this steam is then utilised by a steam turbine connected to a generator for electricity generation.

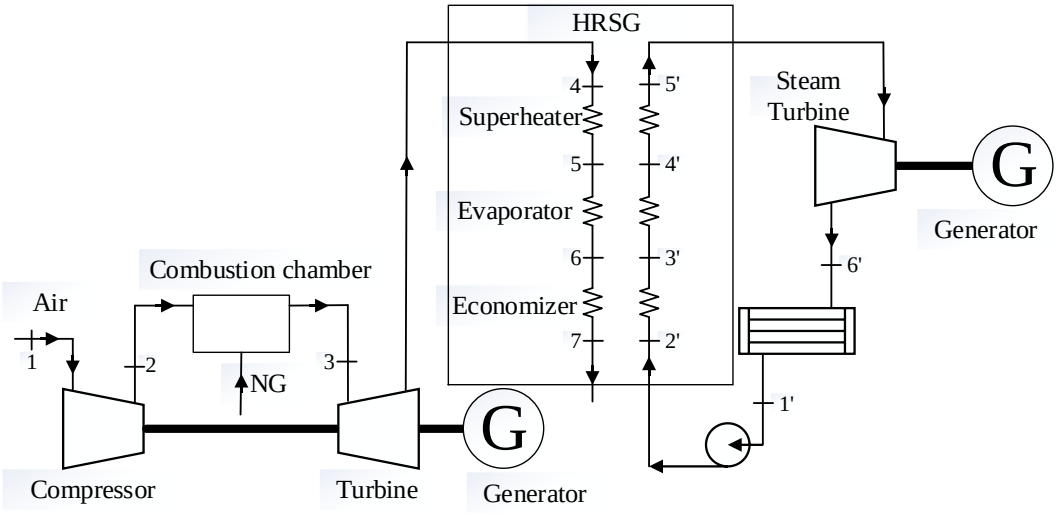

Figure 2.10: Schematic of CCGT power plant [29, 40].

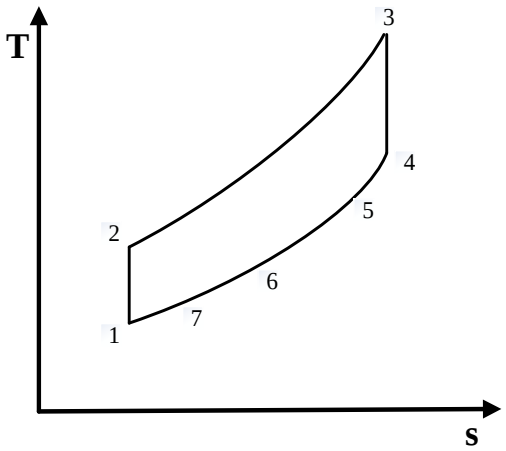

Figure 2.11: Brayton cycle T-s diagram [29].

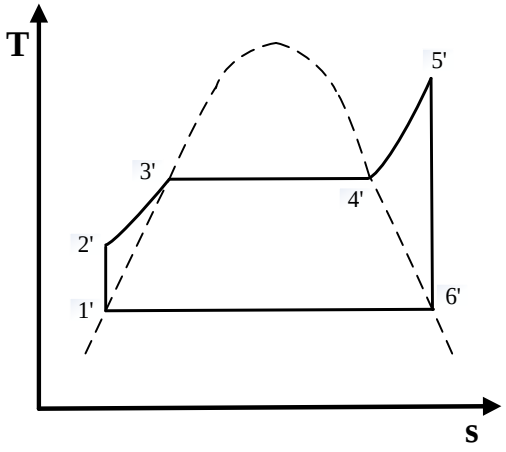

Figure 2.12: Rankine cycle T-s diagram [29].

The T-s diagram of the Brayton cycle and Rankine cycle are shown in Figure 2.11 and Figure 2.12, respectively. It can be seen from the T-s diagrams, the waste heat from position 4 to position 7 is captured by the feed water whose enthalpy is increased to position 5' from position 2'. The exhaust gas lost energy from position 4 to 5 corresponds to the water increased energy from position 4' to 5'. In the same way, position 5 to 6 corresponds to position 3' to 4'; position 6 to 7 corresponds to position 2' to 3'.

The steam turbine output power is:

$$W_{steam} = h_{5'} - h_{6'} \circ \tag{2.10}$$

Therefore, the efficiency of the CCGT power plant is calculated by:

$$\eta = \frac{W_{com} + W_{tur} + W_{steam} + W_{pump}}{Q_{in}} . \tag{2.11}$$

Comparing equation (2.11) with (2.9), it is clear to see how the energy efficiency is improved. The CCGT power plant is characterised by operational flexibility and high efficiency. The other attractive advantage of CCGT power plants is the relatively low investment cost and short construction time compared with coal-fired power plants. The disadvantage of CCGT power plants is in their complexity in combining two power cycles in one plant.

2.4 Review of Recent Development in Flexible Operation of Thermal Power Plants

The operational flexibility of a power plant is the capability of fast start-up or shut-down and to activate quickly to provide power reserves when required [28]. Flexible operation is one of the key solutions to support grid balance in dealing with the great challenges arising from the increased penetration of power generation from renewable energy sources. This section presents an overview of the current development status of thermal power plant flexible operation, including coal-fired power plants, CCGT power plants, CHP power plants and solar thermal power plants.

The steam turbine is the primary mechanical device in most conventional thermal power plants. It converts the thermal energy contained in the high temperature and high pressure steam into mechanical energy. The change in load causes the governing system of a turbine to change the mass flow of steam through the turbine according to the load demand [34]. A nonlinear mathematical steam turbine model is developed by Chaibakhsh and Ghaffari in Matlab Simulink environment, which could present the transient dynamics of the turbine-generator system for various load conditions [41]. Topel et al. studied the potential to improve power plant performance through the increase of steam turbine flexibility at the time of start-up. [42].

Conventional power plant operational flexibility is presented in [33]. The rate of change of plant power output is called ramp rate. A power plant's potential for meeting fluctuating demand grows with higher plant ramp rate. The normal ramp rate of hard coal, gas turbine and CCGT power plants is 1.5-6%, 8-15% and 2-8% of the rated power per minute, respectively [33]. In addition to the flexible operation ability inherent in the plant itself, various alternatives may allow improved plant operation flexibility, such as control strategy optimisation, energy storage integration, etc.

For coal-fired power plants, the most popular strategy to regulate the power output is the boiler-turbine coordinated control. The response speed of this control method is slow due to the large heat transfer delay from the fuel supply to the water-steam cycle. Wang et al. proposed a method to improve the flexibility of the coal-fired power plant by optimising the water fuel ration control strategy [43]. The potential of regulating the extracted steam of high pressure (HP) heaters was evaluated by Zhao et al. to realise the flexible operation of coal-fired power plant [3]. Also, the operational flexibility of a coal-fired power plant could be improved via the TES integration [15].

CCGT power plants are considered as the flexible unit in power grid operation and they can also provide the service of peak shaving [28]. Some previous studies focused on the optimisation of the start-up process of CCGT power plants [44-46], as the start-up speed is one of the important factors for flexibility. On the other hand, Wojcik and Wang proposed a novel hybrid system with CCGT and A-CAES to increase plant operational flexibility [47]. Moreover, the CCGT power plant gains the capabilities of flexible operations through TES integration [48]. Also, Barelli and Ottaviano proposed a method called supercharged gas turbine combined cycle to achieve plant flexible operation, with an additional compressor upstream of the normal gas turbine cycle [49].

As CHP and solar thermal power plants both have Rankine cycle which is the common thing for thermal power plant. Moreover, the Rankine cycle is a vital section for the plant flexible operation. The following two paragraphs review the current development of CHP and solar thermal power plants flexible operation strategies.

CHP is an efficient technology since it produces both power and heat by recovering the waste heat in conventional plants. Fang and Lahdelma showed that thermal storage can significantly improve the flexibility and cost-efficiency of CHP power plants [14]. In the combined CHP and TES system, the excess thermal energy can be stored in the TES unit, during low heat demand. The TES unit can also produce heat to meet the heat demand at peak moments. Hence the electricity and heat

production can be decoupled in the CHP and TES system, which brings flexibility to electricity and heat production [50].

The inherent disadvantage of renewable energy sources is intermittent, such as solar and wind. Fossil fuel power plants align power generation with the load demand by controlling the fuel supply. By contrast, solar energy is available only when the sun is shining. In order to overcome the intermittent character of solar energy, TES system is also necessary for solar thermal power plants [13]. A dynamic model of the solar thermal power plant with TES was developed to illustrate that the use of TES offers plant the ability to generate power at a constant value despite disturbances of solar radiation [51].

In summary, the flexible operation of thermal power plants can be improved via the integration of energy storage, especially the TES. The dynamic performance of gas turbine based power plants is potentially improved through CAES integration. Accordingly, to the best of author knowledge, no relevant studies focused on the methods proposed in Chapter 1 which will discuss in the following chapters.

2.5 Summary

In summary, this section reviews the generation principles of coal-fired power plants and gas-fired power plants. It describes the generation process of different types of coal-fired power plants relying on the Rankine cycle. The subcritical power plant efficiency is low leading to significant nitrogen oxides and carbon dioxide emission. To address the issue, several advanced coal-fired power plants were adopted to improve the cycle efficiency and reduce exhaust gas emission per unit electricity, which are supercritical coal-fired power plants, circulating fluidised bed combustion power plants and integrated coal gasification combined cycle power plants.

The operation of the gas turbine relies on the Brayton cycle. Gas turbine based power plants are employed to provide the service of peak shaving since they are more flexible in operation compared with coal-fired power plants in the grid. In

order to enhance the efficiency of gas-fired power plants, combined Brayton cycle and Rankine cycle power plants were developed, where the heat in gas turbine exhaust is captured by HRSG to produce steam for further power generation, which is called CCGT power plant. The normal ramp rate of CCGT power plants is 2-8% of the rated power per minute.

This chapter also presents a review of the recent research and development in flexible operation strategies of thermal power plants. Based on the existing literature, the previous studies were focused on the control strategies optimisation and energy storage integration to enhance the operational flexibility. The study of CHP power plants and solar thermal power plants with TES integration has been extensively conducted [52-56]. The TES system gives CHP power plants the ability to decouple thermal and power generation, and solar thermal power plants the ability to generate the customer required power despite the disturbances of solar radiation. While the study of the integration of coal-fired power plants and CCGT power plants with TES is still in its early stage.

Chapter 3-Study of Supercritical Coal-fired Power Plant Integration with TES

3.1 Introduction

The operational flexibility of thermal power plants has played an essential role in supporting the increase of renewable power generation integration with the gird. This chapter explores the potential of introducing TES to power generation process to improve the plant dynamic performance for plant flexible operation. In this study, a 600 MW supercritical coal-fired power plant model is chosen as a test base. The main advantage of supercritical coal-fired power plants are their higher thermal efficiency compared with subcritical coal-fired power plants due to their higher operation temperature (500-600 ℃) and pressure (24-26 MPa).

For coal-fired power plants, boiler-turbine coordinated control is a widely used strategy to regulate the power output. However, the plant response is slow in terms of the flexible operation's requirement, which is due to the large delay of the energy transfer from the fuel supply to the water-steam loop. The primary frequency reserve of the thermal power plants relies on its inertia and the thermal storage in the boiler system. Therefore the capability of offering primary frequency control of once-through boiler (supercritical) is smaller than natural circulation boiler (subcritical). This motivates the exploration of the potential for utilisation of TES in supercritical coal-fired power plants because the TES may provide additional thermal reserves when required.

The chapter starts with a brief introduction of the simulation platform SimuEnging. Then, three TES charging strategies are studied: extract steam from intermediate pressure turbine (IPTB) inlet and pass through TES and then loop back to the condenser; extract steam from low pressure turbine (LPTB) inlet and pass through TES and then loop back to the condenser; extract steam from IPTB inlet and pass through TES and then loop back to the LPTB inlet. After that two TES discharging strategies are investigated: use TES to produce additional steam for LPTB; use TES to heat feed water instead of the preheater. Then, the simulation results are

presented and analysed from energy and exergy perspectives. Finally, the investigation is performed in the demonstration of TES integration for improving the performance of grid frequency control.

3.2 Supercritical Coal-fired Power Plant Modelling and the Simulation Platform

In practice, it is almost impossible to test TES integration on a real power plant without considerable feasibility pre-study and off-line test so this study is based on modelling and simulation study. To perform the off-line tests with the optional control mechanism and dynamic responses for a practical power plant, a detailed and visualised simulation platform called SimuEngine was initially developed by Tsinghua University, China and then further applications are exploited at the University of Warwick, UK. SimuEngine accommodates a digital 600 MW supercritical coal-fired power plant modelling and simulation platform coded in FORTRAN language, which has been verified by the real operational plant data [57].

The supercritical power plant model implemented on SimuEngine can deal with a complex flow net which represents a typical power plant system consisting of resistance components (such as valves), power components (such as fans), inertia node and source-sink nodes. The joints in a flow net are defined as nodes, while the channels connected with the nodes are defined as branches. Node pressure method is applied to solve the nonlinear flow net equations in order to obtain the nodes' pressure and flow rates of the branches.

The water-steam loop and control panel of the SimuEngine are shown in Figure 3.1 and 3.2, respectively. Table 3.1 shows a set of typical water/steam parameters in the measurement points when the supercritical coal-fired power plant works at the rated state, at which this power plant consumes 216.3 tons coal per hour, and generates 600 MW electrical power.

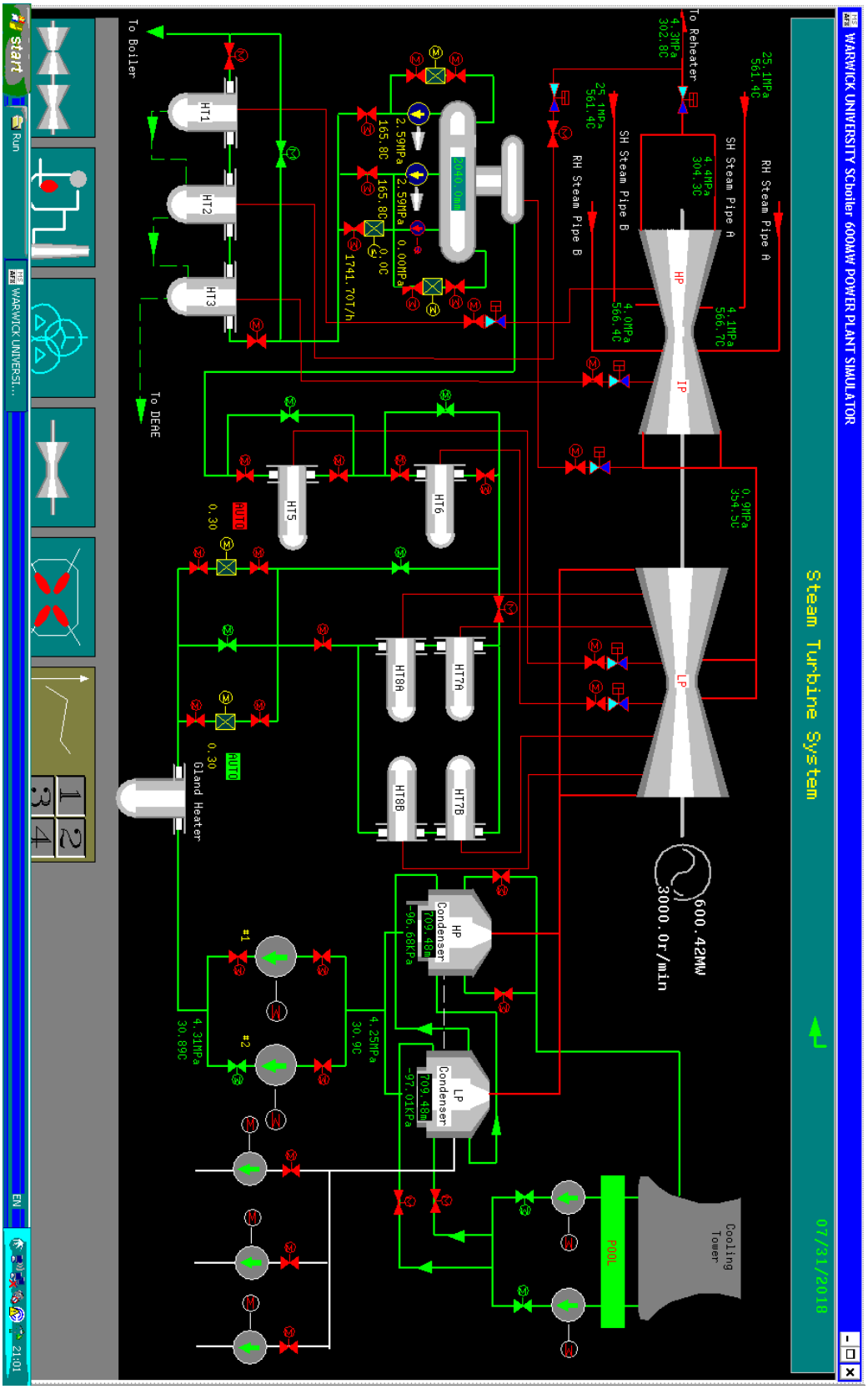

Figure 3.1: SimuEngine water-steam loop.

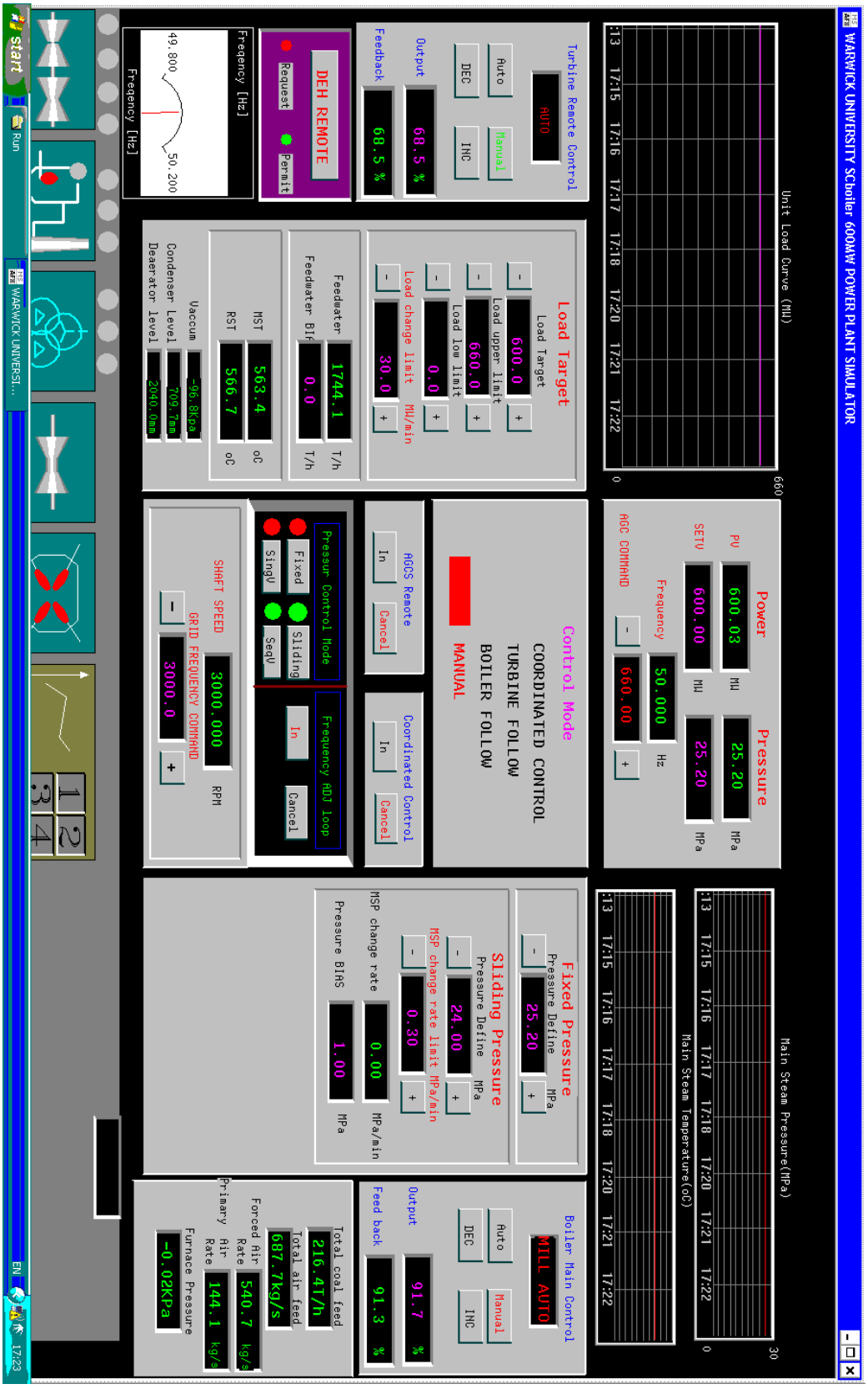

Figure 3.2: SimuEngine control panel.

The schematic diagram of a typical supercritical coal-fired power plant is shown in Figure 3.3. From the figure, it can be seen that there is no steam drum in its water-steam cycle to buffer the steam (thermal energy), which leads to less thermal reserves compared with subcritical power plants.

Table 3.1: Main water/steam parameters in a 600 MW supercritical coal-fired power plant.

	Temperature (℃)	Pressure (MPa)	Flow rate (kg/s)
LP heater inlet	31.96	1.63	351.8
LP heater outlet	107.42	0.62	351.8
HP heater inlet	166.86	27.65	484
HP heater outlet	263.49	27.48	484
Economizer outlet	312.63	27.3	484
Super heater outlet/ HPTB inlet	562.04	25.1	483.9
HPTB outlet	304.72	4.41	445.9
IPTB inlet	565.66	3.8	406.4
IPTB outlet	354.86	0.9	387.2
LPTB inlet	354.86	0.9	309.2

The feed water heater model diagram is plotted in Figure 3.4. The mathematical models for steam heaters are derived with respect to the principle of mass and energy conservation, with convergence parameters. The shell side mass change is determined by the mass flow in and out of the junction point of observation and can be described by mass conservation equation [58]:

$$V_s \frac{d\rho_s}{dt} = \dot{m}_{se} + \dot{m}_{de} + \dot{m}_{lk} - \dot{m}_{dl} \ , \tag{3.1}$$

where, V_s is the volume of shell side, ρ_s is the steam density in shell side, $\dot{m}_{se}$ is the steam entrance mass flow rate, $\dot{m}_{de}$ is the drain water entrance mass flow rate, $\dot{m}_{lk}$ is the pipe leakage mass flow rate, and $\dot{m}_{dl}$ is the drain water mass flow rate.

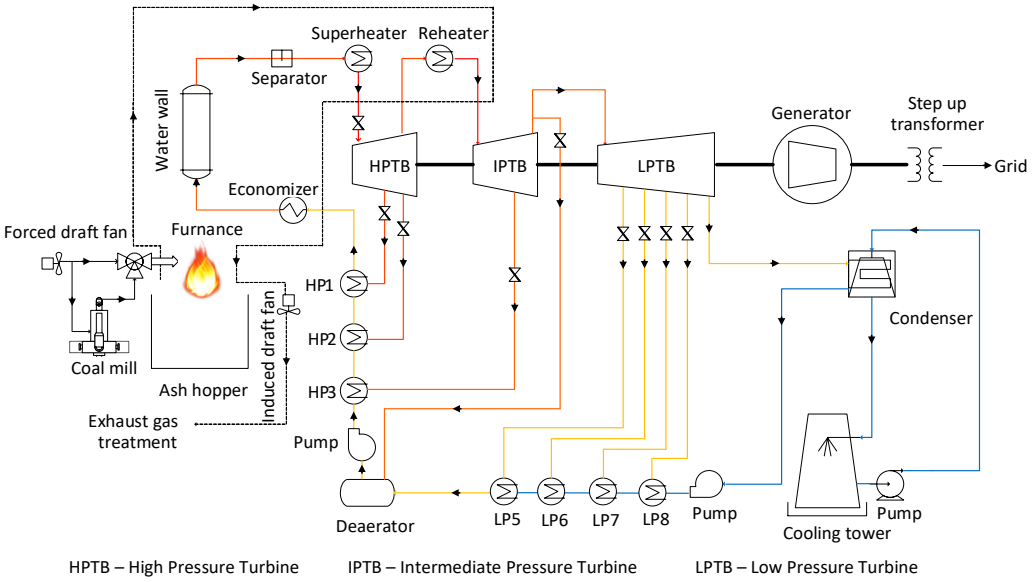

Figure 3.3: Schematic of typical supercritical boiler coal-fired power plant.

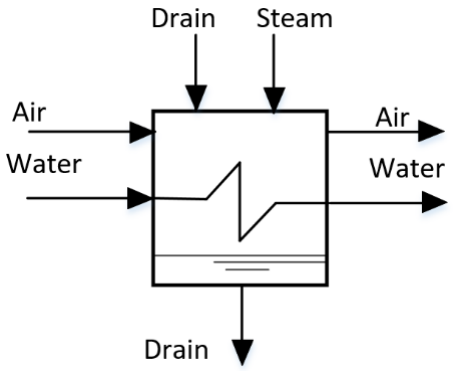

Figure 3. 4: Feed water heater model diagram.

With the hypotheses of that the momentum balance is neglected and the pressure is assumed to be constant in the steam water heater, the energy change at each observation junction is governed by the energy conservation equation [59]:

$$V\rho\frac{dh}{dt}=\dot{Q}-\dot{m}\Delta h, \tag{3.2}$$

where, the left side of the equation is the enthalpy (h)change rate of the working fluid in time domain, V is the volume, ρ is the density, $\dot{Q}$ is the heat transfer rate of the working fluid, and $\dot{m}\Delta h$ is the enthalpy change of the working fluid in space domain.

The heat transfer rate of the working fluid is determined by the temperature difference between the two working fluids, and the heat transfer coefficient (U).Heat transfer rate of the superheat section can be written as:

$$\dot{Q}_{DS} = U_{DS}(T_{se} - T_{wl}) , \tag{3.3}$$

where, T_{se} is the heating steam entrance temperature, T_{wl} is the feed water outlet temperature, and U_{DS} is the heat transfer coefficient of the superheat section.

Heat transfer rate in the saturation section or condensation section is therefore described by:

$$\dot{Q}_{CND} = U_{CND}(T_{sat} - \frac{T_{we} + T_{wl}}{2}) , \tag{3.4}$$

where, T_{sat} is the saturated water temperature, T_{we} is the feed water entrance temperature and U_{CND} is the heat transfer coefficient of saturated section.

Heat transfer rate in the drain cooling section is:

$$\dot{Q}_{DRN} = U_{DRN}(T_{dl} - T_{we}) , \tag{3.5}$$

where, T_{dl} is the drain water temperature and U_{DRN} is the heat transfer coefficient of the drain cooling section.

Both water and steam exists in the shell side, thus the shell side temperature is calculated by the combination of water section and steam section. Hence, the energy conservation equation for saturated water is expressed by:

$$\begin{aligned} &\frac{d}{dt}(\rho_w V_w h_w + \rho_s V_s h_s) = \dot{m}_{se}(h_{se} - h_w) + \dot{m}_{de}(h_{de} - h_w) + \\ &\dot{m}_{lk}(h_{wl} - h_w) - U_{DS}(T_{se} - T_{wl}) - U_{CND}(T_{sat} - \frac{T_{we} + T_{wl}}{2}) - K_a(T_{sat} - T_a) \end{aligned} , \tag{3.6}$$

where, ρ_w is the density of water, V_w is the volume of water, h_w is the enthalpy of saturated water, ρ_s is the density of steam, V_s is the volume of steam, h_s is the enthalpy of saturated water, h_{se} is the enthalpy of heating steam entrance, h_{de} is the

enthalpy of drain water entrance, h_{wl} is the enthalpy of feed water outlet, K_a is the heat dissipation coefficient and T_a is the atmosphere temperature.

Energy conservation equation for drain cooling section is:

$$\rho_{dl} V_{dl} \frac{dh_{dl}}{dt} = \dot{m}_{dl}(h_w - h_{dl}) - U_{DRN}(T_{dl} - T_{we}) - K_{da}(T_{dl} - T_a), \tag{3.7}$$

where, ρ_{dl} is the density of drain water outlet, V_{dl} is the volume of drain water outlet, h_{dl} is the enthalpy of drain water outlet and K_{da} is the heat dissipation coefficient of drain cooling section.

The heater pipe usually is very thin walled, and the temperature difference between the pipe metal and water is small, therefore, the influence of pipe heat storage can be included into water. With this assumption, the energy conservation equation in water side is derived as:

$$\begin{aligned} &\rho_w V_w \frac{dh_{wl}}{dt} + M_m c_{p,m} \frac{dT_m}{dt} = \dot{m}_{we}(h_{we} - h_{wl}) + U_{DS}(T_{se} - T_{wl}) \\ &+U_{CND}(T_{sat} - \frac{T_{we} + T_{wl}}{2}) + U_{DRN}(T_{dl} - T_{we}) - K_{wa}(T_{wl} - T_a) \end{aligned}, \tag{3.8}$$

where, h_{wl} is the enthalpy of feed water outlet, M_m is the mass of pipe, $c_{p,m}$ is the specific heat of metal, T_m is the metal temperature, h_{we} is the enthalpy of feed water entrance and K_{wa} is the heat dissipation coefficient of the water with the atmosphere.

All the working fluid flow is connected by a ‘flow net’ in SimuEngine. Flow net consists of resistance components, power components, inertia nodes and source sink nodes. The task of flow net calculation is to get the pressure of nodes and the flow rate of branches. The flow resistance is used to present the relationship between branch flow pressure drop (ΔP) and flow rate (G). The flow resistance factor (r) is calculated by:

$$r = \frac{\Delta P}{G^2} \ . \tag{3.9}$$

The valves are installed in the power plant at various sections to control the flow rate. The flow valve port area is controllable, which results in valve resistance factor changes and the resistance factor is calculated by:

$$r = (1+\frac{T}{273})r_0(k) = (1+\frac{T}{273})\frac{r_{00}}{[k\ f(k)]^2}\ , \qquad (3.10)$$

where, k is the valve opening, $r_0(k)$ is the resistance factor when valve opening is k and temperature is 0 ^oC, r_{00} is the resistance factor when valve opening is 1 and temperature is 0 ^oC and $f(k)$ is a function defined by valve opening and associated coefficients.

Different components of the power plant process are linked via "flow net" which is a realisation of recursive steps of calculation for achieving energy balance and mass balance at each connecting note point. The flow net equations are nonlinear, so it is a challenging task to solve these nonlinear equations. In SimuEngine power plant simulation model, the node pressure method is used, which is to build pressure equations of each node to get linear equations in the flow net. Once the node pressure is calculated, the flow rate of each branch can be calculated by the resistance equation ($rG^2 = \Delta P$). Pure resistance of the flow net is schematically shown in Figure 3.5.

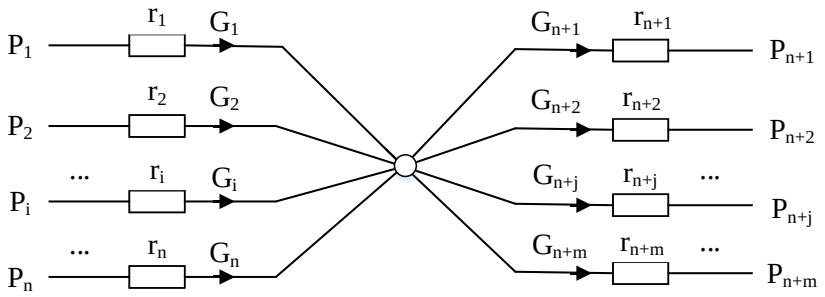

Figure 3.5: Flow net diagram for pure resistance branches.

Node pressure (P) can be calculated by the equation:

$$P = \frac{\sum_{i=1}^{n+m} \frac{P_i}{b_i}}{\sum_{i=1}^{n+m} \frac{1}{b_i}} \tag{3.11}$$

$$b_i = r_i |G_i|, i = 1, 2, \cdots, n+m \tag{3.12}$$

where, P_i is the pressure of the node i, r_i is the resistance factor of branch i, and G_i is the flow rate of branch i.

If the node is a large inertia vessel or tube, the equation should be modified to:

$$P = \frac{\sum_{i=1}^{n+m} \frac{P_i}{b_i} + PC}{\sum_{i=1}^{n+m} \frac{1}{b_i} + C}, \tag{3.13}$$

$$C = \frac{d\rho}{dP} \cdot \frac{V}{dt}, \tag{3.14}$$

where, V is the node volume, and $\frac{d\rho}{dP}$ is the derivation of node fluid density to pressure.

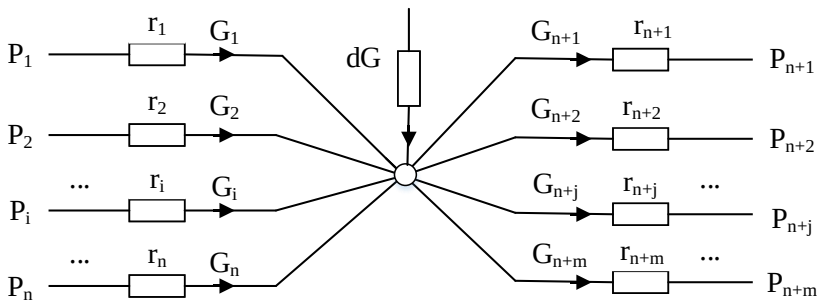

Figure 3.6: Flow net diagram for source node.

If the node is a source (dG), as shown in Figure 3.6. The node pressure equation should be modified to:

$$P = \frac{\sum_{i=1}^{n+m} \frac{P_i}{b_i} + dG}{\sum_{i=1}^{n+m} \frac{1}{b_i}} \quad , \tag{3.15}$$

where, dG is the source branch flow rate. If the branch is a sink, the dG should change to $-dG$.

In real-time simulation, if the disturbance is small, the solution could be calculated without iteration; if the disturbance is significant and cannot be neglected, the iteration is used to improve the accuracy of the solution. More details can be found from previous publications [57, 60, 61].

With this power plant system model and simulation platform, the feasibility study for TES integration is presented in the following subsection. The study is to test the feasible TES charging and discharging strategy to match the needs of the load demand.

3.3 Simulation Study of TES Charging Strategies

This section presents the TES charging strategies during the off-peak period. The idea is to extract high-temperature steam from the water-steam loop of the power plant which will pass through the thermal storage unit during the off-peak period. In this way, the electrical power output can be controlled by regulating thermal energy output for power generation while maintaining the constant boiler heat generation. This section is to find the answers to the following concerns: where the TES can be integrated and how much thermal energy can be extracted without affecting the dynamic performance of the supercritical power plant.

Due to the high energy quality of the steam in the high pressure turbine (HPTB), extract steam from HPTB inlet is not an efficient way for thermal storage. Therefore, two suitable thermal energy extraction points have been identified, which are IPTB (Intermediate Pressure Turbine) inlet and LPTB (Low Pressure Turbine) inlet, and three TES charging strategies are investigated. It should be noticed that the steam

temperatures at the IPTB inlet and LPTB inlet are around 565 ℃ and 355 ℃ with the pressures around 3.8 MPa and 0.9 MPa, respectively, for the plant used for this simulation study. The detailed integration strategies and simulation results are presented and analysed in the following subsections.

3.3.1 Extracting Steam from IPTB and Looping the Steam Back to the Condenser

The first steam extraction point is placed in the inlet of the IPTB, whose high-temperature steam passes a TES unit for thermal storage after extraction. The outlet steam of the TES flows into the condenser after the thermal charge process, mixing with the LPTB outlet steam. The schematic of this TES charging strategy is shown in Figure 3. 7, where the dashed line is the path of the extracted steam.

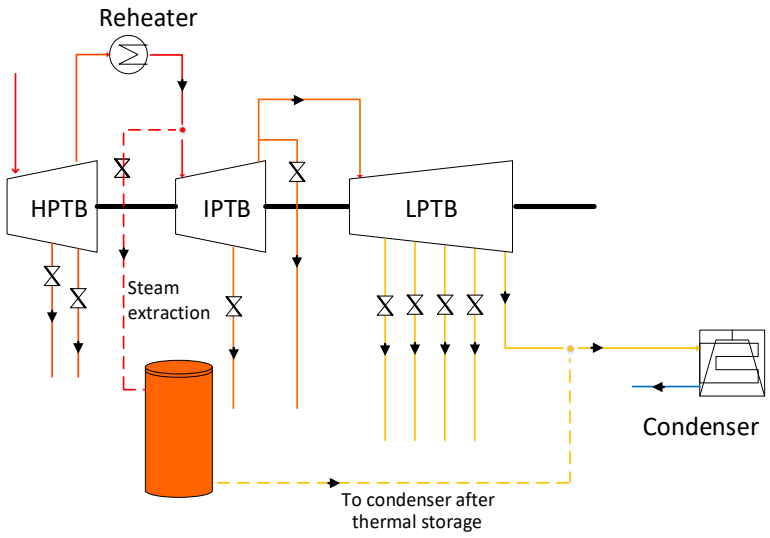

Figure 3.7: Schematic of the first TES charging strategy.

The amount of steam extraction is controlled by the valve (on the dashed line) regulations. With different valve openings, the mass flow rate to the IPTB and also the power output will be different, and the mass flow rate to the LPTB and preheaters will be changed as well. In this study, the valve opening does not mean the percentage of steam extraction from IPTB inlet, the mass flow rate of extracted steam is determined by the upstream and downstream pressures, the configuration

of valves and the value opening. The bigger value of valve opening means more steam will be extracted from the turbine. The simulation results of the mass flow rate and the variations of the plant power output with different valve openings are shown in Figure 3.8, and the IPTB inlet temperature, pressure and mass flow rate are shown in Figure 3.9.

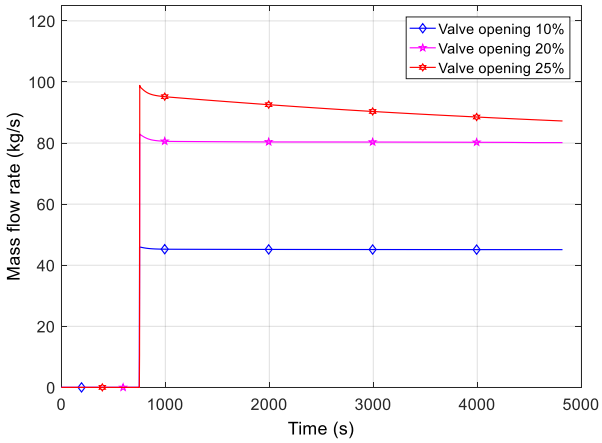

(a)

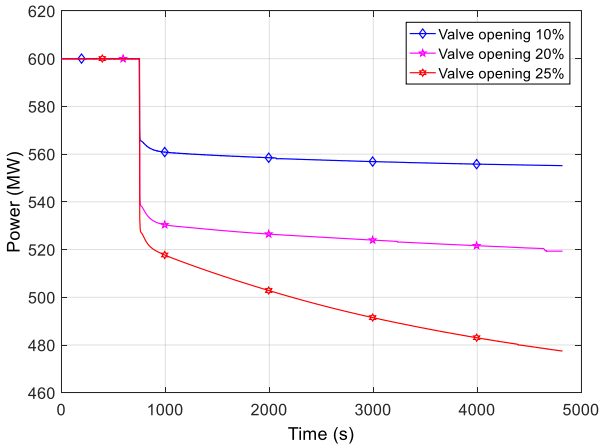

(b)

Figure 3.8: Relationship of extracted steam from IPTB inlet and output power: (a) Mass flow rate; (b) Output power.

The mass flow rate changes affects the steam temperature and pressures to the turbine inlet. As shown in Figure 3.9 (a), the IPTB inlet temperature has a rapid drop after steam extraction. This is because the sudden pressure drop leads to more water/steam being drawn from the boiler. After that, the IPTB inlet temperature

stabilized at a certain value below the rated number. This is due to the decrease of IPTB and LPTB mass flow rate, which leads to less steam being extracted for the deaerator and feed water preheaters (HP3, LP5, LP6, LP7, LP8), as shown in Figure 3.3, which results in the decline of feed water temperature. From Figure 3.8, it can be seen that the changes need to be limited to an available range to maintain stable operation of the power plant. If the steam is extracted beyond a critical limit, the plant output power will continue to decline (valve opening 25%), which is caused by the collapse of power plant pressure level. The simulation results indicate that the maximum mass flow rate of steam extraction from the IPTB inlet is 80 kg/s, and the adjustment range of the output power is 13.3% of its rated power. Meanwhile, the IPTB inlet temperature decreases to 564.4 K, and the IPTB inlet pressure decreases to 3.28 MPa.

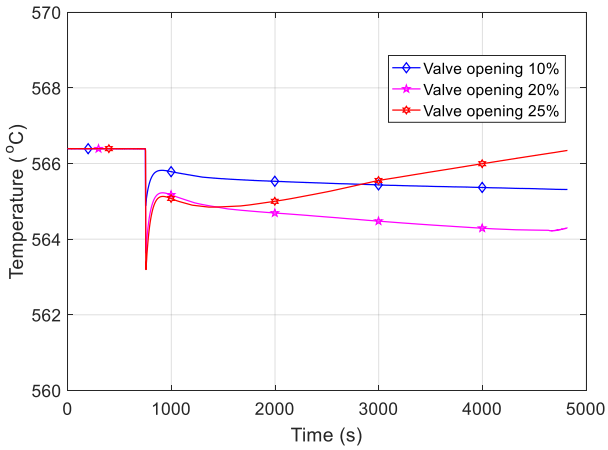

(a)

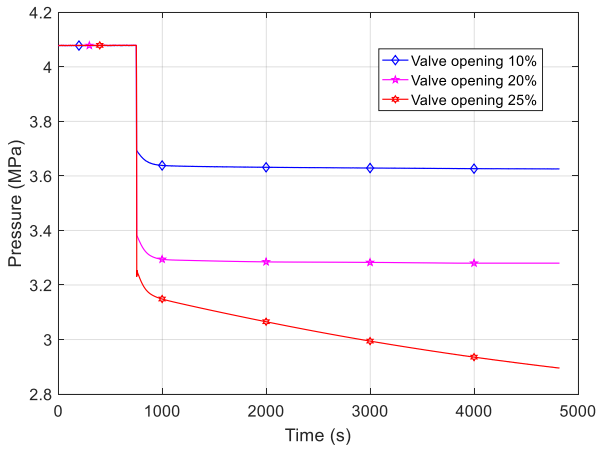

(b)

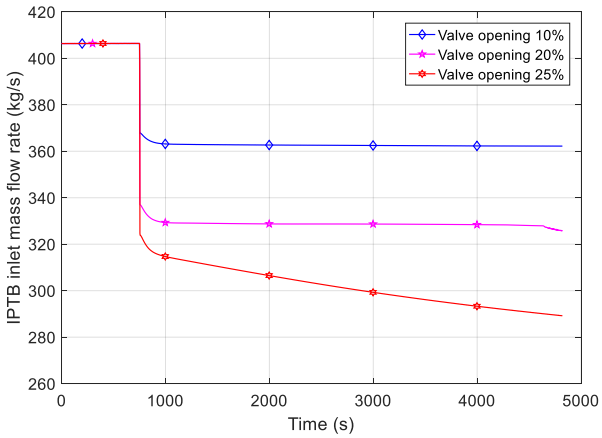

(c)

Figure 3.9: IPTB inlet: (a) Temperature; (b) Pressure; (c) Mass flow rate.

3.3.2 Extracting Steam from LPTB and Looping the Steam Back to the Condenser

Instead of the IPTB inlet, the steam extraction at the inlet of LPTB is studied in this subsection. The steam flows into the condenser after TES charging process mixing together with the steam from LPTB outlet. The schematic of this TES charging strategy is shown in Figure 3.10, where the dashed line is the path of the extracted steam.

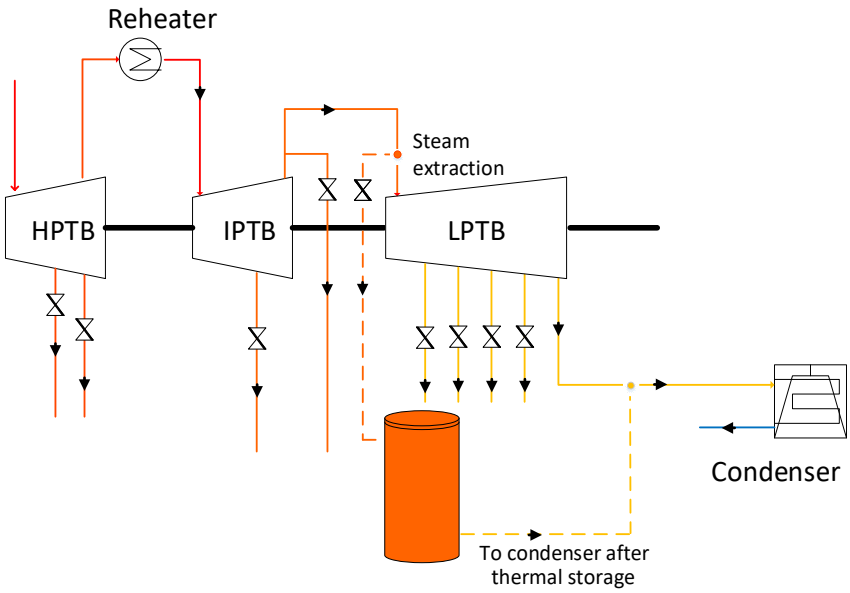

Figure 3.10: Schematic of the second TES charging strategy.

The simulation results of the mass flow rate and plant power output changes with different valve openings are shown in Figure 3.11, and the LPTB inlet temperature and pressure are shown in Figure 3.12. Similar to the steam extraction from the IPTB inlet, the simulation results indicate that the maximum mass flow rate of steam extraction from the LPTB inlet is 56 kg/s, and the adjustment range of the output power is 6.5% (561 MW).

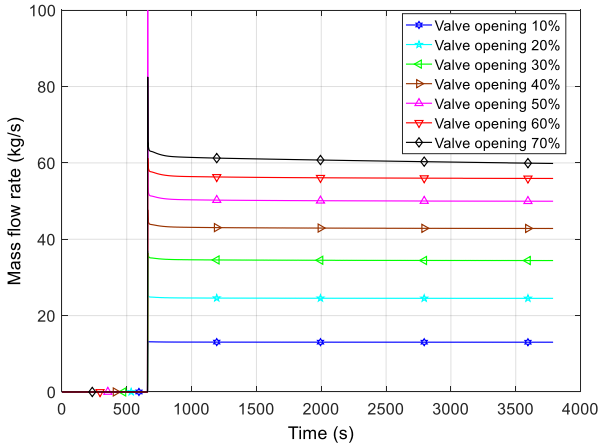

(a)

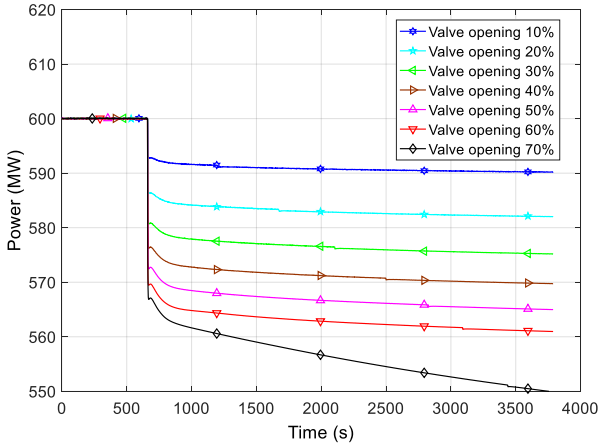

(b)

Figure 3.11: Relationship of extracted steam from LPTB inlet and output power: (a) Mass flow rate; (b) Output power.

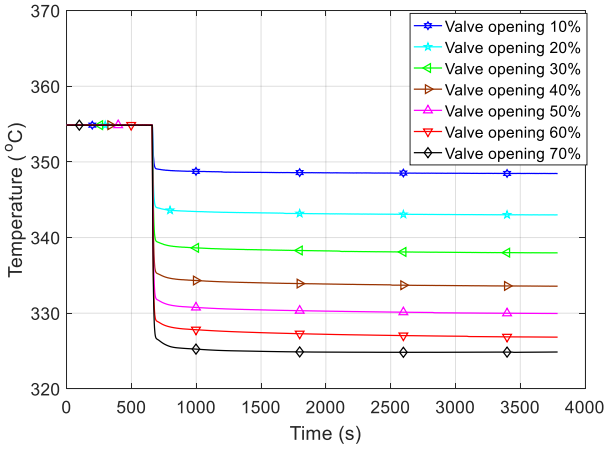

(a)

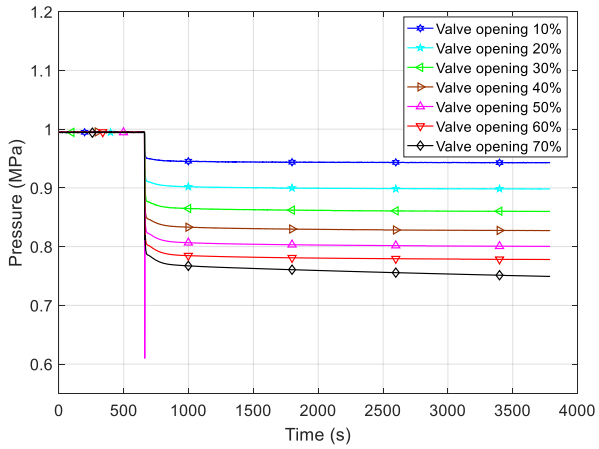

(b)

Figure 3.12: L PTB inlet: (a) Temperature; (b) Pressure.

3.3.3 Extracting Steam from IPTB and Feeding the Steam Back at LPTB Inlet

This TES charging strategy is to extract steam from IPTB inlet, after thermal storage the steam will feed back at LPTB inlet. The study reported in this section relies on the assumption that the steam temperature and pressure can be controlled after passing through the thermal storage unit. When the temperature of the steam is controlled to have the same temperature required by the LPTB inlet, the steam can be fed back to the LPTB directly to mix with the steam coming from IPTB. The

schematic of this TES charging strategy is shown in Figure 3.13, where the dashed line is the path of the extracted steam.

The simulation results of the mass flow rate and power output associated with different valve openings are shown in Figure 3.14. With various operation status and applying the above TES charging strategy, the maximum mass flow rate of steam can be extracted from the inlet of IPTB is 174 kg/s, and the adjustment range of the output power is about 96.1% (576.5 MW). Excess steam extraction leads to the steam pressure dropping to lower than the operating pressure required by IPTB. Therefore, this TES charging strategy only works with a small range of power regulation. The merit of this strategy is to recycle the steam back to LPTB which does not change the whole system cycle of the LPTB section.

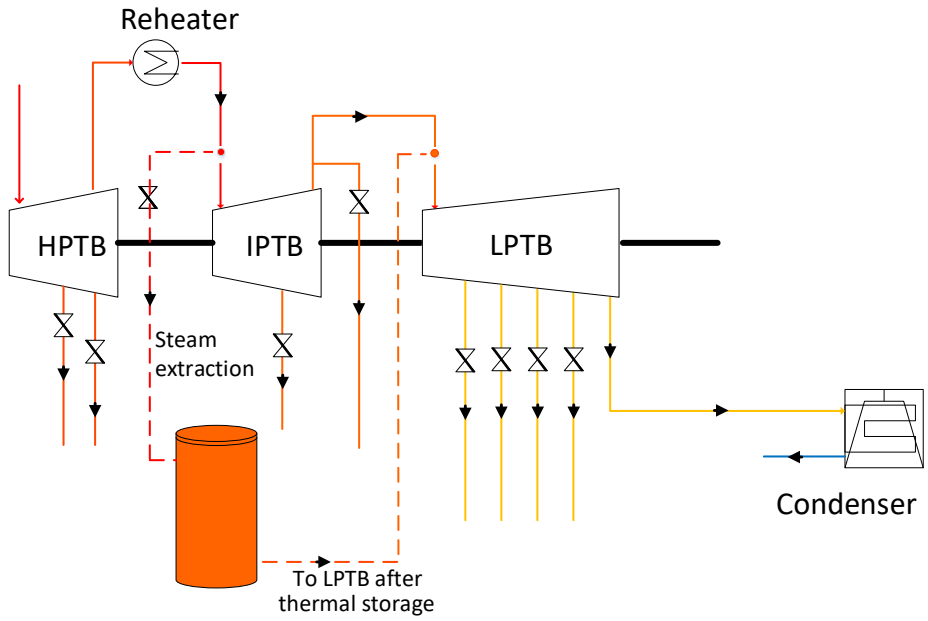

Figure 3.13: Schematic of the third TES charging strategy.

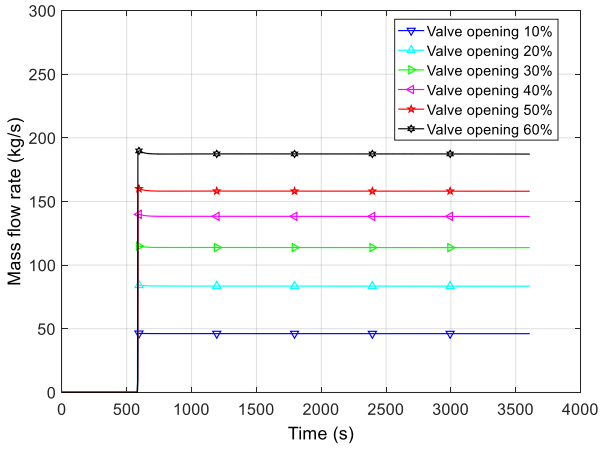

(a)

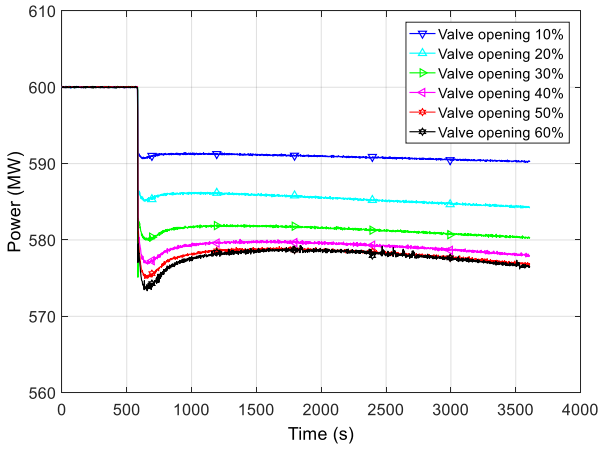

(b)

Figure 3.14: Relationship of extracted steam from IPTB inlet and output power: (a) Mass flow rate; (b) Output power.

3.4 Simulation Study of TES Discharging Strategies

During the electricity peak demand period, the stored thermal energy should be discharged back to the water steam loop to increase the total electricity generation. Two strategies have been investigated: the first one is to use TES to produce high-temperature and high pressure steam for LPTB; the second one is to use TES to preheat the feed water instead of using the original preheater. Considering the temperature of the TES, the generated steam cannot satisfy the requirement of the

IPTB inlet, therefore, it needs to be fed into LPTB inlet. The simulation study for these two TES discharging strategies is presented and analysed in the following subsections.

3.4.1 Using TES to Produce Additional Steam for LPTB

During the TES discharging process, part of the feed water flows into the bottom of the TES unit from the deaerator, which evaporates into high-temperature steam and is superheated while it rises through the tubes in the TES, then it leaves the TES as superheated steam. This steam is then fed to the steam turbine, which leads to the increase of the electric power output. As part of water is taken out of the deaerator, therefore, more water needs to be pumped into the deaerator in order to maintain the steam mass flow rate in the HPTB and IPTB. Figure 3.15 shows the schematic diagram of the designed TES discharging strategy, where the dashed line is the path of the feed water and the generated steam.

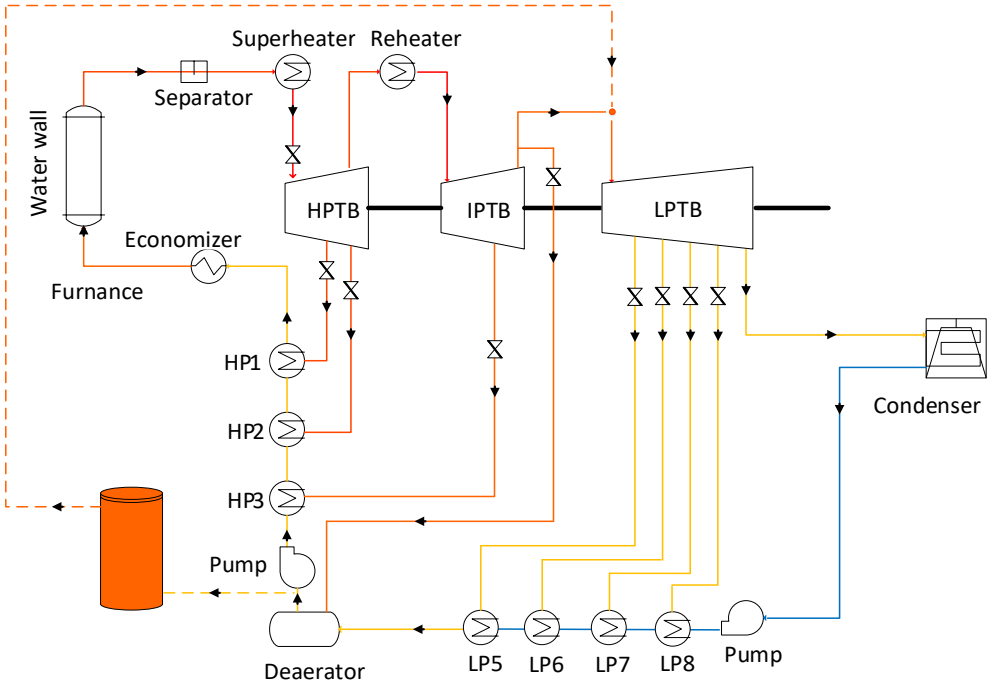

Figure 3.15: Schematic of the TES discharging strategy.

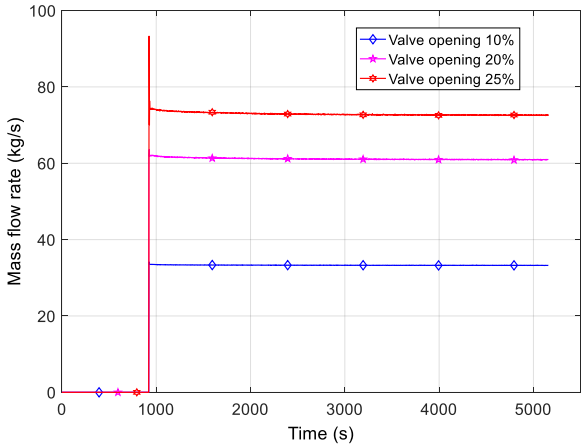

(a)

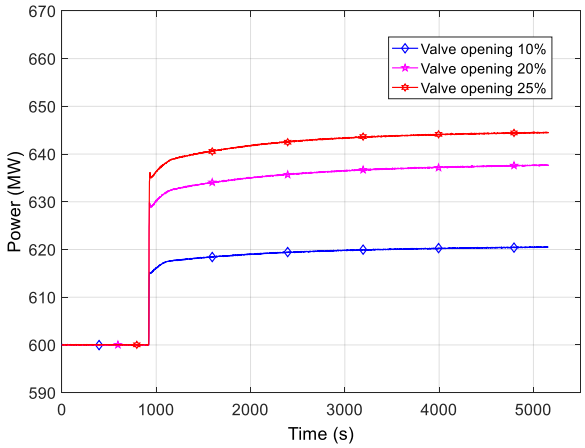

(b)

Figure 3.16: Relationship of generated steam for LPTB inlet and output power: (a) Mass flow rate; (b) Output power.

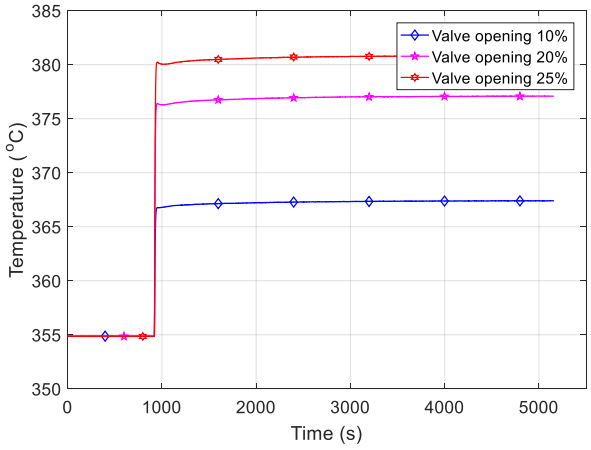

(a)

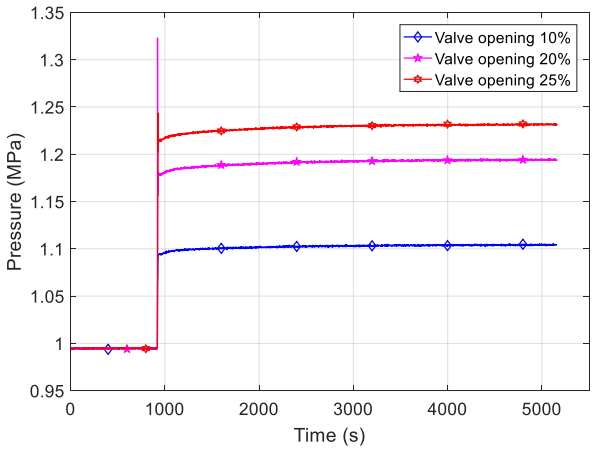

(b)

Figure 3. 17: LPTB inlet: (a) Temperature; (b) Pressure.

The simulation results of the mass flow rate and the variations of the plant power output are shown in Figure 3.16, and the LPTB inlet temperature and pressure are shown in Figure 3.17. With the various valve openings, the increased steam mass flow rate and power output are observed. From the simulation study, the maximum steam mass flow rate could be increased at the inlet of the LPTB is 72.6 kg/s. As a result, the maximum output power is 644.4 MW, which nearly reaches the design upper limitation of the plant power output (650 MW).

3.4.2 Using TES to Heat the Feed Water Instead of Preheater

In a supercritical coal-fired power plant, some portion of the steam is taken out from the steam turbines to preheat the feed water, as shown in Figure 3.3. In this supercritical coal-fired power plant, there are three HP heaters and a group of LP heaters. The steam taken out from the HPTB is used for No.1 and No.2 HP heaters, the extracted steam from the IPTB is used for No.3 HP heater, and the steam taken from LPTB is used for LP heaters, as shown in Figure 3.3. The amount of the steam extraction is controlled by regulating valve openings; when these valves are closed, more steam will pass through the downstream turbines and produce more power. However, this operation leads to a decrease of the feed water temperature. While, the temperature of the feed water can be maintained via the TES integration. The feed water will bypass the preheaters and flow into TES to raise its temperature, and then the stored thermal energy is discharged back to the water-steam cycle. The simulation results are shown in Figure 3.18.

When the valve used to extract steam for No.3 HP heater is closed, the feed water should bypass the No.3 HP heater and be heated by the TES. As a result, the output power increases to near to 615 MW from 600 MW. When those valves for extracting steam to feed into the LP heaters are closed, the feed water should bypass the LP heater and be heated by the TES. The output power increases to around 616.5 MW from 600 MW. When those valves for extracting steam to feed into the LP heaters and No.3 HP heater are closed, the feed water should bypass both the LP heaters and No.3 HP heater and be heated by TES. The output power then increases to 634 MW from 600 MW. This method requires no plant structure changes, so it is feasible and cost-effective, although the power regulation capability is limited to a relatively small range.

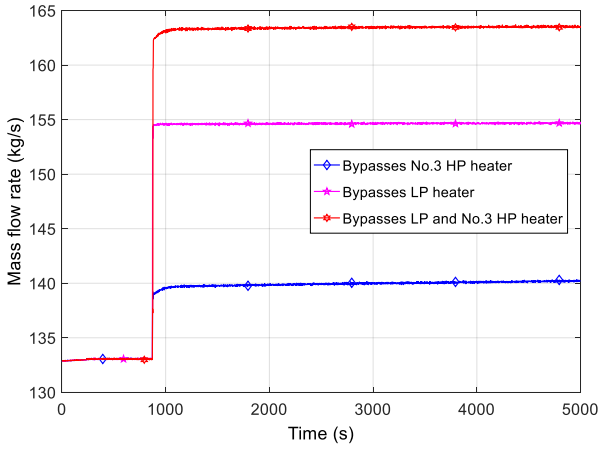

(a)

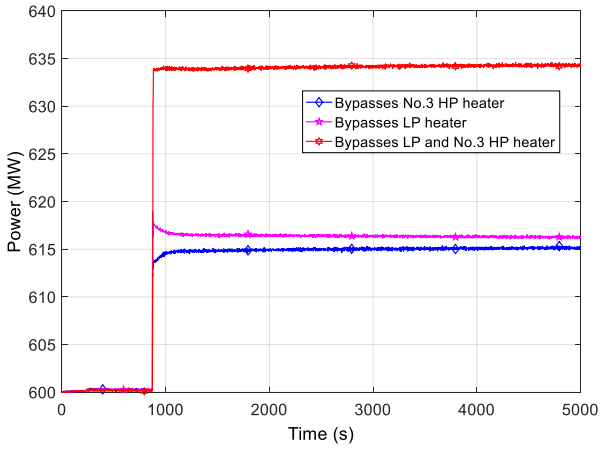

(b)

Figure 3.18: Using TES to heat feed water instead of preheater: (a) Mass flow rate; (b) Output power.

3.5 Energy and Exergy Analysis

The exergy refers to the energy which can be converted into doing work. Unlike the energy, exergy is always destroyed when a process is irreversible. Exergy analysis is based on the first and second thermodynamic laws, which provide a further clearer view of the energy transfer and balance of the power generation process [62]. When the power plant reaches its steady state, the stored or released thermal energy rate and the exergy variation rate can be calculated by the following equations.

The stored thermal energy rate ($\dot{E}$) can be calculated by:

$$\dot{E} = \dot{m}(h_{in} - h_{out}) , \tag{3.16}$$

where, $\dot{m}$ is the mass flow rate, subscript *in* and *out* represent inlet and outlet of the store, respectively.

Exergy is the maximum capacity of the energy that can be converted into work. The specific exergy (ψ) is calculated by the following equation [63]:

$$\psi = h - h_0 - T_0(s - s_0), \tag{3.17}$$

where, h is the enthalpy, s is the entropy, h_0, T_0 and s_0 are reference enthalpy, temperature and entropy, respectively. Note that the exergy is calculated when T_0 is 298.15 K, P_0 is 101.3 kPa.

The exergy change rate ($\dot{E}_x$) is calculated by [63]:

$$\dot{E}_x = \dot{m}[h - h_0 - T_0(s - s_0)], \tag{3.18}$$

The exergy variation rate is given by:

$$\Delta\dot{E}_x = \dot{E}_{x,in} - \dot{E}_{x,out} = \dot{m}[h_{in} - h_{out} - T_0(s_{in} - s_{out})] . \tag{3.19}$$

During the TES charging process, the stored energy and the lost exergy can be calculated, according to the Equation (3.16) and (3.19). As an example, the stored thermal energy rate and the lost exergy rate of the third TES charging strategy are calculated for various operating conditions, as shown in Table 3.2, which represents the energy and exergy changes of the extracted steam from IPTB inlet and looping back at LPTB inlet. The enthalpy and entropy of IPTB inlet and LPTB inlet are listed in Table 3.2 for different working conditions. The load condition 1 is the rated load condition (without TES charging), the load conditions 2 to 7 represent different valve opening of the third TES charging strategy, and the simulation results of this strategy can be seen from section 3.3.3.

Table 3.2: Energy and exergy analysis of TES charging process.

Load conditions / Parameters	1	2	3	4	5	6	7
Generated power (MW)	600	590.4	584.5	580.7	578.2	577.3	576.5
IPTB inlet enthalpy	3597.1	3597.5	3598.4	3599.3	3598.2	3596.8	3595
IPTB inlet entropy	7.27	7.315	7.35	7.39	7.41	7.43	7.45
LPTB inlet enthalpy	3168.9	3209.2	3245.6	3279.5	3306.9	3329.3	3348.1
LPTB inlet entropy	7.32	7.36	7.4	7.43	7.46	7.48	7.5
Extract steam (kg/s)	0	46.1	83.4	113.7	138.2	158	174.2
Stored thermal energy (MW)	0	19.9	29.42	36.36	40.26	42.27	43
Lost exergy (MW)	0	18.52	30.67	37.71	42.32	44.62	45.6

For TES discharging process, as an example, the released thermal energy rate and the increased exergy rate of the first TES discharging strategy are calculated and shown in Table 3.3, which describes the TES energy release to generate additional steam for the LPTB inlet. It can be seen that from Table 3.3, in order to produce satisfactory steam for the LPTB, the required thermal energy is nearly triple to the increased exergy of the feed water. This is due to the increase of the entropy from the deaerator outlet to LPTB inlet, during the TES discharging process.

Table 3.3: Energy and exergy analysis of TES discharging process.

Load conditions / Parameters	1	2	3	4
Generated power (MW)	600	620	637	644.4
Deaerator outlet enthalpy	720.9	741.4	759.4	762.4
Deaerator outlet entropy	1.98	2.02	2.06	2.07
LPTB inlet enthalpy	3168.9	3193.26	3212.13	3219.56
LPTB inlet entropy	7.32	7.32	7.308	7.305
Generated steam (kg/s)	0	32.2	60.9	72.6
Released thermal energy (MW)	0	78.95	149.55	178.4
Increased exergy (MW)	0	28.07	54.26	65.08

3.6 Thermal Energy Storage Model

This section presents the designed TES model. There are mainly three types of thermal energy storage: sensible heat storage (SHS), latent heat storage (LHS), and chemical heat storage [64]. SHS involves heating a storage material, without experiencing a phase change in it, where the heat is stored by increasing the temperature of storage material. LHS involves heating a material when it experiences a phase change, which can be from solid to liquid or from liquid to gas. For the third storage method, chemical heat storage consists of a reversible endothermic chemical reaction, during which the energy is stored or released by reforming or breaking chemical bonds [65].

Latent heat storage will be used for this study because its energy density is much higher than sensible heat storage and the cost is lower than chemical heat storage. Moreover, as presented by Kuravi, the exergy efficiency of TES can be significantly

improved using multiple phase change materials (PCMs) compared with a single phase change material (PCM) [66]. Therefore, the designed TES model is shown in Figure 3.19.

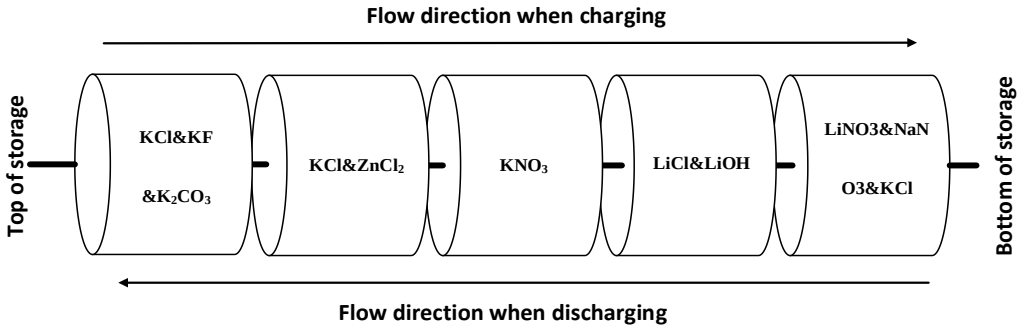

Figure 3.19: Designed TES model with five PCMs.

The composition of PCMs is: KCl&KF&K2CO3, KCl&ZnCl2, KNO3, LiCl&LiOH and LiNO3&NaNO3&KCl separately arranged along the charging flow direction. Their thermodynamic properties are listed shown in Table 3.4. For TES charging process, the extracted steam flows in the decreasing order of phase change temperature. For the discharging process, the flow direction of HTF is reversed in the increasing order of phase change temperature.

Table 3.4: Thermodynamic properties of salts compositions extracted from [67, 68].

Material	Composition, wt%	Melting temperature, ℃	Latent heat, J/g	Specific heat, J/(g·K)		Density, g/cm^3
				Solid	Liquid	
PCM1	KCl(40)- 23KF-37K_2CO_3	528	283	1.00	1.26	2.28
PCM2	KCl (54)- 46 $ZnCl_2$	432	218	0.67	0.88	2.41
PCM3	KNO_3	330	172	1.22	1.22	2.26
PCM4	LiCl(37)- 63LiOH	262	485	2.40	2.40	1.55
PCM5	$LiNO_3$(55.4)-4.5$NaNO_3$- 40.1KCl	160	266	1.4	1.4	2.21

A case study is carried out for the first TES charging strategy. In order to calculate the capacity of TES, some assumptions have to be made: 1) The average HTF mass

flow rate is 50 kg/s; 2) The TES is fully charged in two hours; 3) The TES initial and final temperature and the average steam temperature are shown in Figure 3.20. Operating around the phase change temperature exploits PCMs benefits [69], so the initial and final temperatures are set around their melting temperature.

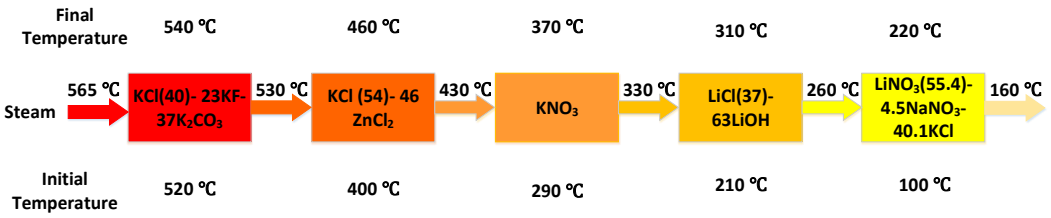

Figure 3.20: TES and steam temperature.

The stored thermal energy can be calculated by:

$$Q_{storage} = \dot{m}_{steam}(h_{in} - h_{out})t\,, \tag{3.20}$$

where, $Q_{storage}$ is the stored thermal energy, $\dot{m}_{steam}$ is the mass flow rate of steam, h_{in} is the inlet steam enthalpy, h_{out} is the outlet steam enthalpy, and t is the charging time.

The energy stored in mass M_{PCM} for a solid-liquid transition in a PCM is calculated by:

$$Q_{storage} = M_{PCM}[c_{p,s}(T_{melting} - T_{solid}) + l + c_{p,l}(T_{liquid} - T_{melting})], \tag{3.21}$$

where, M_{PCM} is the mass of PCM, $c_{p,s}$ is the heat capacity for solid phase, $c_{p,l}$ is the heat capacity for liquid phase, T_{solid} is the solid temperature (initial temperature), T_{liquid} is the liquid temperature (final temperature), $T_{melting}$ is the phase change temperature and l is the enthalpy of phase change.

Therefore, based on the assumptions, a total of 288.72 GJ heat is stored in the TES system, and 26.64 GJ, 76.68 GJ, 74.52 GJ, 47.52 GJ and 63.36 GJ for KCl&KF&K2CO3, KCl&ZnCl2, KNO3, LiCl&LiOH and LiNO3&NaNO3&KCl, respectively. The required mass of KCl&KF&K2CO3, KCl&ZnCl2, KNO3,

LiCl&LiOH and LiNO3&NaNO3&KCl are 87, 292, 276, 66 and 146 ton, respectively.

For the other TES integration strategies, the HTF could flow into or out of the TES at different positions based on the temperature of HTF and PCMs. For the second TES charging strategies, the HTF could bypass PCM1, PCM2 and PCM3, and pass through PCM4 and PCM5. For the third TES charging strategy, the HTF could pass through PCM1, PCM2 and PCM3, and then looping back to the LPTB inlet. For the first TES discharging strategy, the HTF will pass through entire TES from PCM5 to PCM1. For the second TES discharging strategy, the HTF will pass through PCM5 or PCM4 or PCM5 and PCM4 depending on different integration methods.

3.7 Power Grid Frequency Regulation

The simulation results show that the power plant could operate flexibly via TES integration but having a constant thermal generation. The plant output power can be regulated through TES charging and discharging processes, which offers enhanced capability in providing the services for load shifting and grid frequency control. This section presents the results in investigation on how the TES integration improves the plant responses to the grid demand changes.

First, the simulation study is conducted to test whether the extra regulation of water-steam loop via the TES integration can speed up the power plant dynamic responses. The first test is to present the power plant dynamic performance during off peak time. At the beginning , the power plant operates at 600 MW; at 584 seconds the load demand is reduced to 580 MW. The simulation results are shown in Figure 3.21 (a). The second test is to present the power plant dynamic performance during peak time. At the beginning , the power plant operates at 600 MW; at 584 seconds the load demand is increased to 615 MW. The simulation results are shown in Figure 3.21 (b). The dashed line describes the dynamic responses of power output without TES integration, and the output power is directly controlled by changing

the mass flow rate of coal feeding through coordinated control method. While, the solid line represents the output power dynamic performances with the TES integration, in which the output power is regulated with the support of TES charging and discharging processes and the amount of feed coal (fuel input) remains at the rated value. The Figure 3.21 presents that the power plant shows faster dynamic responses and offers a more smooth transition with TES integration compared with the plant responses without TES integration.

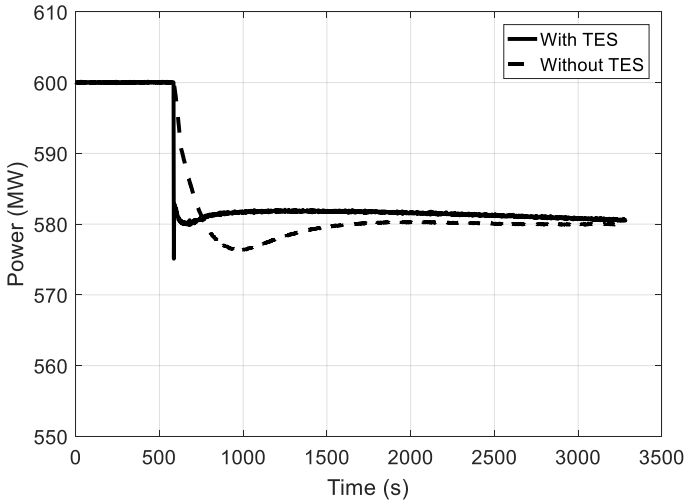

(a)

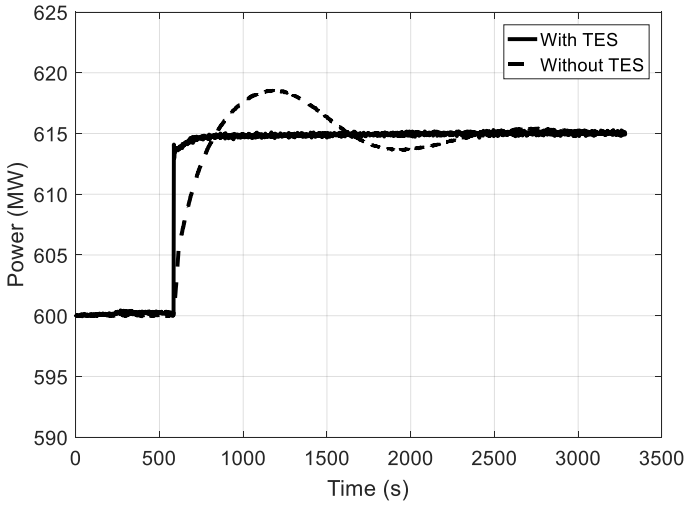

(b)

Figure 3.21: Contribution of the TES to match the load demand: (a) OFF peak period; (b) Peak period.

A gird frequency response model is developed to present the dynamic responses of the power plant in serving grid load balance, which is then linked to the power plant model. This frequency response model can represent how the plant flexible operation stabilises the grid frequency to the rated value. Because of the mechanical inertia of the power grid, the grid frequency fluctuation will take time when the mismatch happens between the generation and the load. The power plant controller will monitor the frequency variations and take the deviation into account when making its control decision. When the frequency drops, more power will be generated to meet the load demand; when the frequency rises, less power will be generated to match the load demand.

The governing equation to the generator speed changes is relevant to the system inertia (J) and torque balance as shown in the following Equation [70]:

$$J\frac{d\omega}{dt} = \tau_a = \tau_m - \tau_e, \tag{3.22}$$

where, ω is the rotation speed, τ_a is the accelerating torque, τ_m is the mechanical torque, and τ_e is the electrical torque.

The inertia constant (H) of a synchronous machine can be estimated by [71]:

$$H = \frac{E_{kinetic}}{S_{rated}} = \frac{1}{2}\frac{J\omega^2}{S_{rated}}, \tag{3.23}$$

where, $E_{kinetic}$ is the kinetic energy of synchronous machine, and S_{rated} is the nominal power rating.

The droop constant (R_i) describes the power versus frequency characteristic of the generator speed governor setting and it is defined as [71]:

$$R_i = -\frac{\Delta f}{f_0} \Big/ \frac{\Delta Power_i}{S_i}, \tag{3.24}$$

where, Δf is the frequency deviation, f_0 is the normal grid frequency, $\Delta Power_i$ is the power deviation of the *i*-th generation unit, S_i is the nominal power rating.

The imbalanced power and the frequency deviation can be described as [71]:

$$Power_M - Power_L = 2H\frac{d\Delta f}{dt} + D\Delta f\ , \qquad (3.25)$$

where, $Power_L$ is the load demand, $Power_M$ is the generated power, and D is the load response [72].

Applying Laplace transform to the above equation, the following equation can be derived [72]:

$$Power_M(s) - Power_L(s) = (2H \times s + D)\Delta f(s)\ . \qquad (3.26)$$

Some assumptions are made based on the GB (Great Britain) power system characteristics. The droop constant (R_i) is set to 4%, the load response (D) is 1. The mechanical acceleration time constant is ($M = 2H$) about 10.8 seconds.

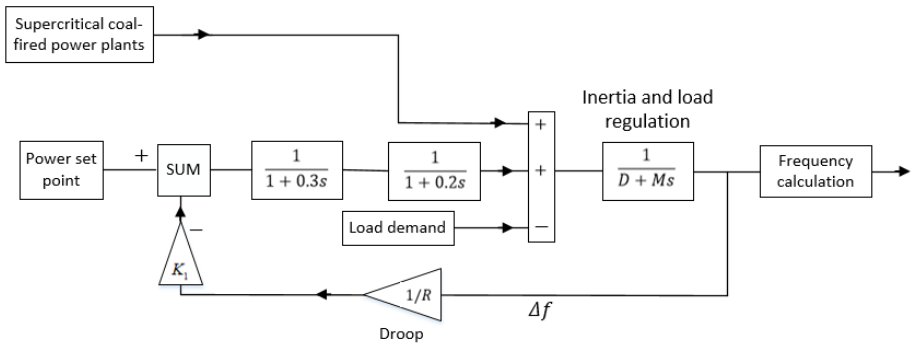

Figure 3.22: Block diagram of GB power grid frequency response system.

Figure 3.22 shows a model to represent the GB power grid frequency response. It is used to study how the supercritical coal-fired power plant with TES integration operates flexibly in supporting the service of grid frequency control. In Great Britain, the average demand is about 40GW, and the coal-fired power plants currently provide about 15% (around 6GW) of the total load demand. With the model shown in Figure 3.22, a simulation study is conducted by linking the power plant dynamic responses to the power grid model. Figure 3.23 presents the grid frequency responses when the load demand decreases by 0.5% at the time of 584 seconds from the time when the simulation starts. Then the system frequency starts

increasing, thus the supercritical coal-fired power plants are controlled to decrease the power output to restore the rated frequency of the power grid (50 Hz). Figure 3.23 shows that the grid frequency response is faster when the supercritical coal-fired power plant is integrated with TES system.

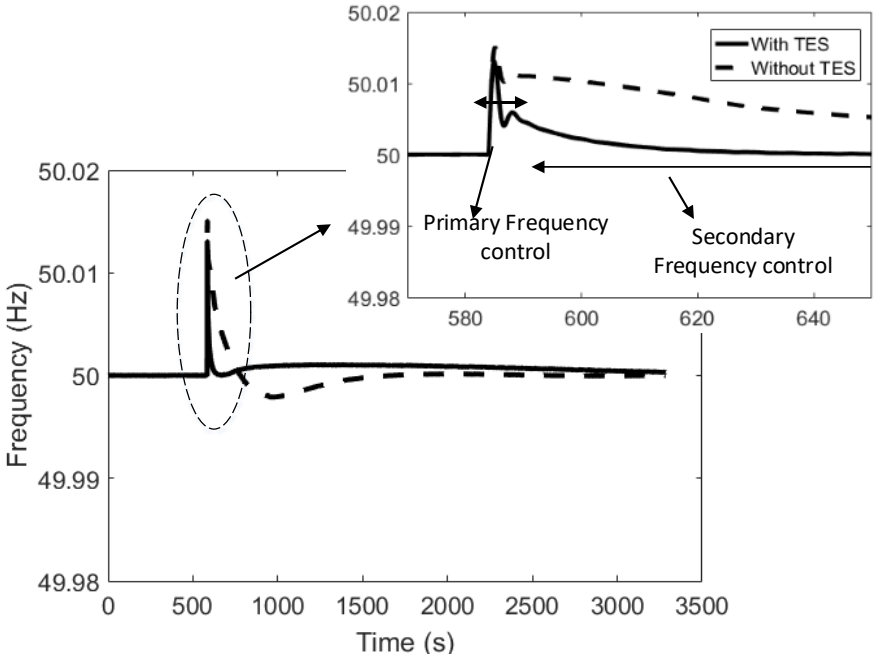

Figure 3.23: Grid frequency response for load decrease.

Figure 3.24 shows the grid frequency responses after a sudden increase in load demand. According to the equation 3.25, the grid frequency starts to decline. After the frequency nadir is reached, the power plants start to increase their power output, so the grid frequency is brought back to the rated value. The TES system provides additional thermal reservoir for the plant, which respond much faster than the regulation of fuel supply because of the shorter delay of heat transfer. From Figure 3.24, it is clear to see how the system dynamic response speed changes when the TES is integrated into the power generation process.

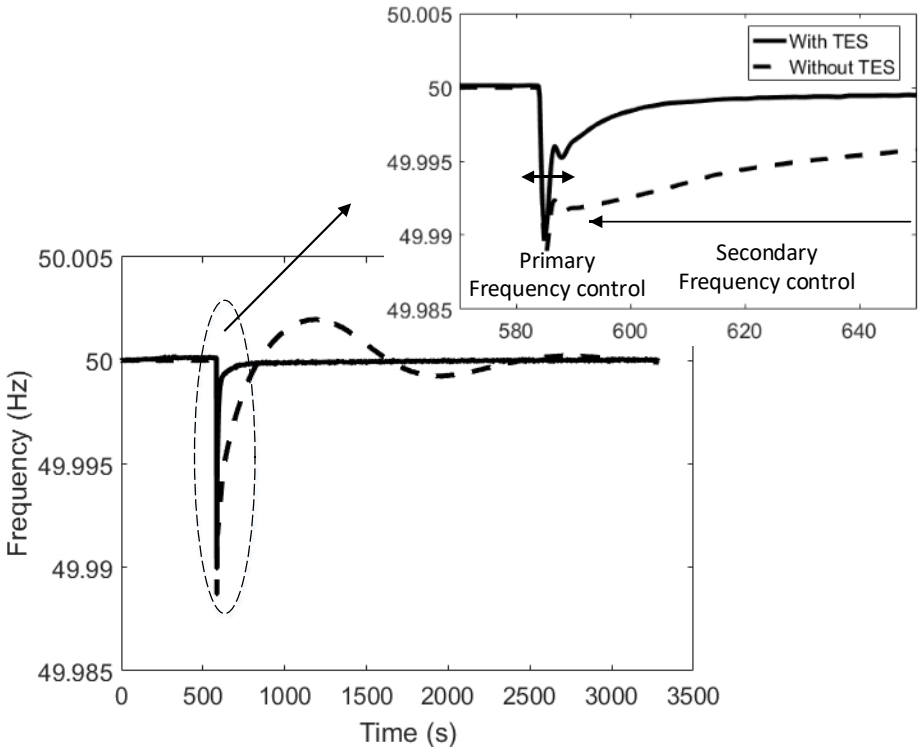

Figure 3.24: Grid frequency response for load increase.

In summary, the imbalance of the load demand and power generation leads to frequency deviations, the primary spin reserve based on the power grid mechanical inertia could stabilise grid frequency at a certain level, which is called primary frequency control. While, in order to recuperate the rated frequency and release the primary reserve, the secondary frequency control is needed. It can be seen from Figure 3.21, integrating TES into supercritical coal-fired power plant improves the plant dynamic performances for smoothing the gap between supply and demand. Figure 3.23 and Figure 3.24 demonstrate the merit of TES integration in meeting load demand and grid frequency control.

3.8 Summary

This chapter describes the modelling and simulation study for TES integration into a 600 MW supercritical coal-fired power plant for flexible plant operation. Three TES charging strategies, and two TES discharging strategies were investigated. The

simulation results show that it is feasible to extract thermal energy from the water steam cycle for TES charging during the off-peak period, and the stored thermal energy can be discharged back to the water-steam loop during the peak demand period to rise the power generation. The TES integration steady-state simulation results were analysed from the energy and exergy balance point of view. The simulation results evidence that:

1. It is a feasible way to integrate TES into the water-steam loop of the power plant to regulate the thermal energy used for power generation.

2. For the TES charging processes, the amount of steam extraction needs to be restricted in order to maintain stable power output. The first TES charging strategy is to extract steam from IPTB inlet and loop the steam back to the condenser. For the first TES charging strategy, the maximum flow rate of steam extraction from IPTB inlet is 80 kg/s, and the relative reduction of the power output is 13.3%. The second TES strategy is to extract steam from LPTB inlet and loop the steam back to the condenser. For the second TES charging strategy, the maximum flow rate of stream extraction from LPTB inlet is 56 kg/s, and the relative reduction of the power output is 6.5%. The third TES charging strategy is to extract steam from IPTB inlet and loop the steam back to the LPTB inlet. For the third TES charging strategy, the maximum flow rate of steam extraction from IPTB inlet is 174 kg/s, and the relative reduction of the power output is 3.9%.

3. The first TES discharging strategy is to use stored thermal energy to generate additional steam for LPTB. For the first TES discharging strategy, the maximum mass flow rate of generated steam is 72.6 kg/s, and the corresponding overall output power is 644.4 MW. The second TES discharging strategy is to use TES to heat the feed water instead of preheaters. For the second TES discharging strategy, the maximum output power is 634 MW.

4. With the TES integration, the supercritical coal-fired power plant shows faster dynamic responses to the load demand changes and performs better in grid frequency responses.

Chapter 4-Dynamic Modelling of CCGT Power Plant using Aspen Plus

4.1 Introduction

The main objective of this study is to examine and analyse the possibility of combined cycle gas turbine (CCGT) power plant integration with energy storage to improve the plant dynamic performance. So the dynamic simulation study of CCGT power plants is an essential step in developing and initially verifying the potential strategies for flexible plant operation without compromising its residual life. This chapter contributes to deriving a CCGT power plant dynamic simulation model.

An extensive literature survey, revealed that very few researchers have conducted the dynamic mathematical modelling of CCGT power plants. A complete water-steam bottoming cycle of a CCGT power plant with triple pressure stages is modelled based on the advanced process simulation software Apros [73]. Alobaid developed an entire dynamic sub-critical Benson HRSG model using the Apros [74]. A detailed steady-state model of a 420 MW CCGT power plant is created based on a Thermoflow THERMOFLEX model by Adams [75].

This chapter presents the dynamic modelling of a 420 MW CCGT power plant in Aspen Plus. It starts with describing the whole power plant structure and parameters. It gives the mathematical models of components in terms of the gas turbine section, HRSG section and steam turbine section. A novel method is presented to achieve system dynamic simulation in Aspen Plus.

4.2 CCGT Power Plant Description

A detailed dynamic model of a 420 MW with triple-pressure CCGT power plant is developed in a commercial software Aspen Plus, as shown in Figure 4.1. Aspen Plus is a flowsheet simulation software, and it stores a large database of interaction parameters which are used with mixing rules to estimate mixture properties. It has been widely employed for process simulation purposes by industrial entities since

the late 1990s [76-79]. However, all of these studies are based on steady state models. To assess flexible plant operation, it is essential to understand the dynamic behaviour of the power plant for variable load demand operation. So this chapter proposes a novel modelling approach to address the limitation of Aspen Plus software and capture the main dynamic behaviour of the simulated system in Aspen Plus by incorporating an external dynamic model.

Figure 4.1 presents the diagram of the triple pressure CCGT power plant. The plant comprises a gas turbine, an HRSG, and three steam turbines. The gas turbine has a compressor (in the model is COMP) and a turbine (in the model is EXP) running on a common shaft with a combustion chamber (in the model is COMB) in between. The HRSG comprises three steam generation subsections: high pressure, intermediate pressure, and low pressure. Each subsystem has its own feed water pump: HPPMP, IPPMP, and LPPMP, in Figure 4.1. The three pressure levels water flows into HRSG to convert to steam for expansion in steam turbines: HP, IP, and LP, in Figure 4.1. After that, the exhaust steam flows to a condenser (in the model is COND), and the condensate water is pumped back to HRSG to start a new cycle.

Under rated conditions, the CCGT power plant combusts 14.46 kg/s natural gas to produce 420 MW power, where 285 MW of the power generated through the gas turbine, and 135 MW of the power generated through steam turbines. The plant rated state parameters are listed in Table 4.1.

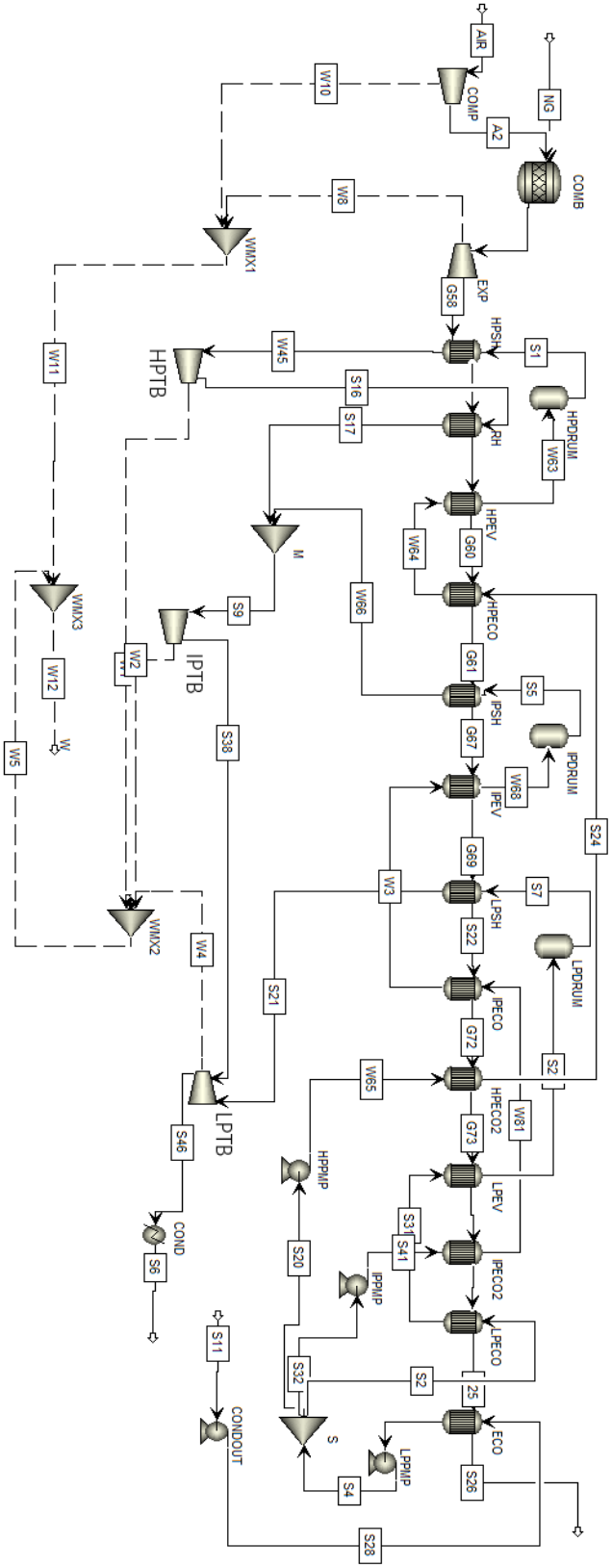

Figure 4.1: The developed 420 MW CCGT power plant model in Aspen Plus.

Table 4.1: Parameters of developed CCGT power plant.

Parameter	Value
Gas turbine power	285 MW
Steam cycle power	135 MW
Fuel supply	14.46 $kg \cdot s^{-1}$
Exhaust gas mass flow rate	677 $kg \cdot s^{-1}$
Exhaust gas temperature	846 K
Feed water flow rate	108 $kg \cdot s^{-1}$
High pressure steam turbine pressure	140 bar
Intermediate pressure steam turbine pressure	25 bar
Low pressure steam turbine pressure	6 bar

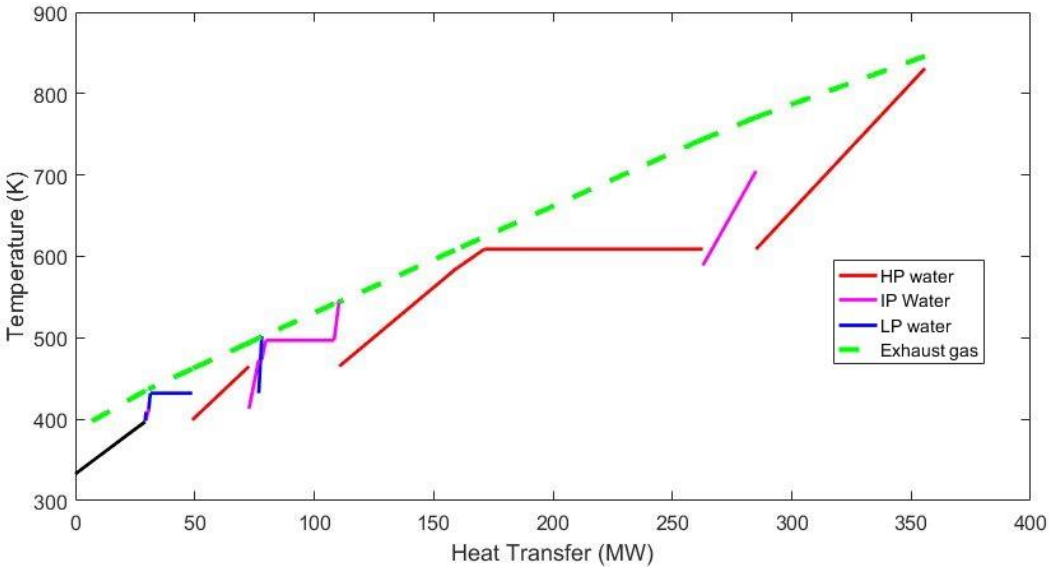

Figure 4.2: Rated load HRSG profiles in the CCGT power plant model.

The HRSG temperature profiles in the developed CCGT model running at rated load are shown in Figure 4.2. The HRSG consists of three distinct pressure levels (HP, IP and LP) of water/steam, they are plotted with red, purple and blue colours, respectively. At the HRSG, the heat is transferred from exhaust gas (dashed green line) to the three levels of water/steam through a series of heat exchangers, and the exhaust gas flows through HRSG at a higher temperature than the water-steam loop.

There are three evaporators arranged in the HRSG, where the temperature of water/steam is kept at its at evaporation point. Accordingly, the three horizontal lines demonstrates these processes, as shown in Figure 4.2.

4.3 Dynamic Modelling of CCGT Power Plants

This section presents the mathematic modelling of a 420 MW CCGT power plant. The process diagram of the developed CCGT power plant model is shown in Figure 4.3. A CCGT power plant generally consists of the gas turbine, HRSG and steam turbines. Air is compressed via a compressor and is mixed with natural gas (NG) in the combustion chamber for combustion, then hot combustion gas expands in the gas turbine, which forms a Brayton cycle. The waste heat from the gas turbine exhaust is recovered via the HRSG which is then used by the steam turbines for electricity generation, which forms a Rankine cycle. In this way, the CCGT power plant can achieve a much higher thermal efficiency than a single cycle gas turbine power plant.

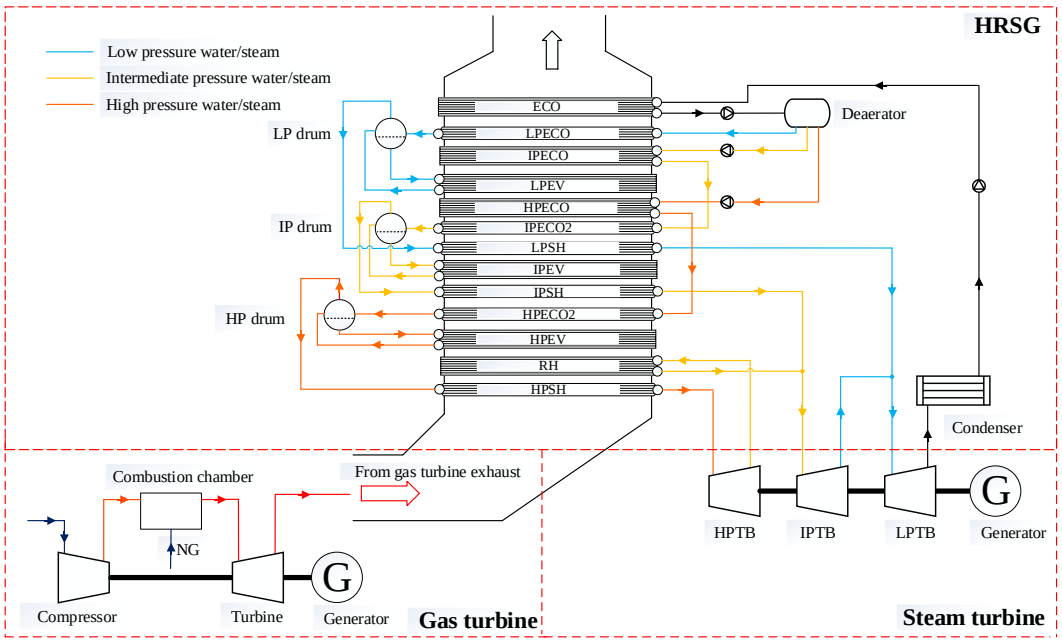

Figure 4.3: Schematic of CCGT power plant.

The gas turbine exhaust pass through HRSG in the order of high pressure superheater (HPSH), reheater (RH), high pressure evaporator (HPEV), second high pressure economizer (HPECO2), intermediate pressure superheater (IPSH), intermediate pressure evaporator (IPEV), low pressure superheater (LPSH), second intermediate pressure economizer (IPECO2), high pressure economizer (HPECO), low pressure evaporator (LPEV), intermediate pressure economizer (IPECO), low pressure economizer (LPECO), and economizer (ECO). As shown in Figure 4.3, three pressure levels of steam are produced, where the red, orange and blue line represents high, intermediate and low pressure water/steam, respectively.

4.3.1 Gas Turbine Section Modelling

The gas turbine section consists of three components: a compressor, a combustion chamber, and a turbine. The flowsheet connectivity for a compressor is shown in Figure 4.4. In the developed system, the material of compressor inlet stream is the air and the outlet stream is the compressed air. The outlet work stream is used to represent the required power for compression.

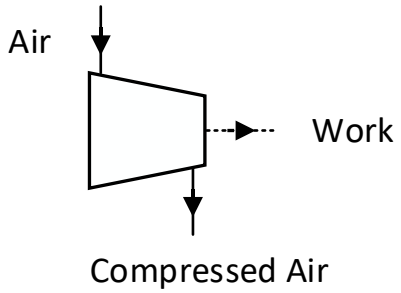

Figure 4.4: Flowsheet connectivity for compressor.

For the compressor, it is modelled as a polytropic compression process, and its power consumption can be calculated by [80]:

$$W_{in,\,ideal} = \left(\frac{\gamma}{\gamma - 1}\right) P_{in} V' \left[\left(\frac{P_{out}}{P_{in}}\right)^{(n-1)/n} - 1\right], \qquad (4.1)$$

$$W_{in} = \frac{W_{in,\,ideal}}{\eta_c} \ , \tag{4.2}$$

where, $W_{in,\,ideal}$ is the power consumption under ideal polytropic condition, γ is the specific heat ratio, P_{in} is the inlet pressure, V' is the specific volume, P_{out} is the outlet pressure, n is the polytropic exponent, W_{in} is the real power consumption, and η_c is the compressor polytropic efficiency.

The actual polytropic efficiency of the compressor varies with mass flow rate and is plotted in Figure 4.5 [81]. The efficiency curve is formulated by using several high-order polynomial equations to minimise errors between efficiency curve and numerical value. The polytropic efficiency (η_c) is incorporated into Aspen Plus by a FORTRAN subroutine, and updated each time-step based on the instant compressor mass flow rate. (see Appendix)

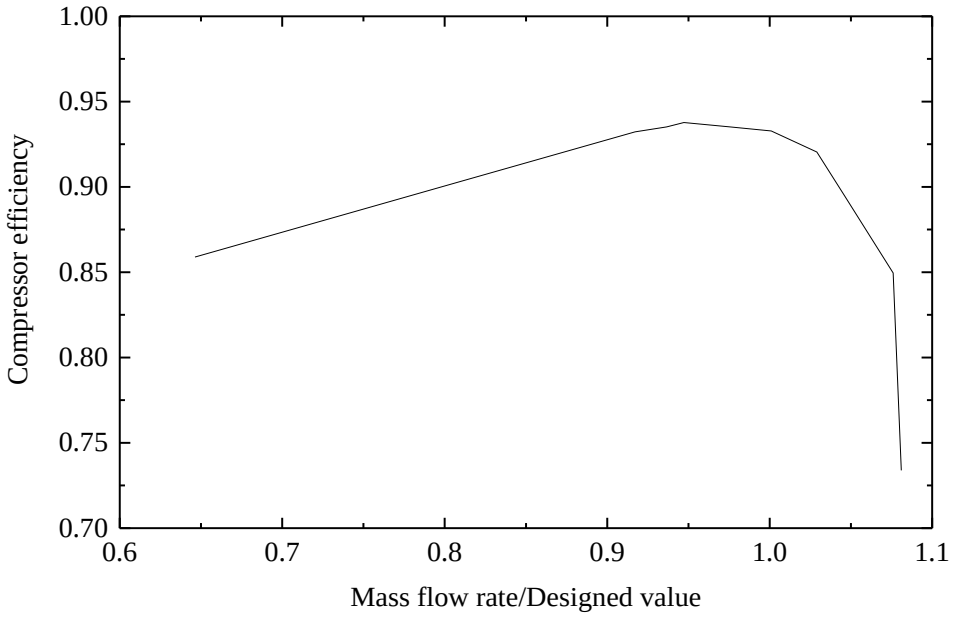

Figure 4.5: Compressor efficiency curve.

The temperature of the compressor outlet stream is given by:

$$T_{out} = \frac{T_{in}}{\eta_c}\left[\left(\frac{P_{out}}{P_{in}}\right)^{(\gamma-1)/\gamma} - 1\right] + T_{in} \ , \tag{4.3}$$

where, T_{out} is the outlet temperature, and T_{in} is the inlet temperature. The air composition used in modelling is given in Table 4. 2. It can be seen from Equation 4.1, 4.2 and 4.3 that higher compressor efficiency leads to lower power consumption and lower outlet temperature of the compressor for a target outlet pressure.

Table 4.2: Air composition in molar fraction [82].

Components	Molar Fraction (%)
N_2	75.67
O_2	20.35
H_2O	3.03
CO_2	0.345
Others	0.915

For the combustion chamber, the flowsheet connectivity diagram is shown in Figure 4.6. In this model, there are two inlet material streams compressed air and natural gas, while the outlet material stream is the combustion gas for the turbine.

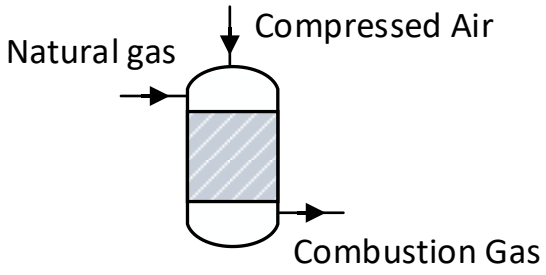

Figure 4.6: Flowsheet connectivity for combustion chamber.

The natural gas composition used in the modelling is given in Table 4.3. Although it consists of methane, ethane, propane, nitrogen, carbon dioxide, and other gases, in fact methane and ethane account for more than 99% of the total volume [83]. Therefore, only two reactions are considered in the combustion process:

$$CH_4 + 2O_2 = CO_2 + 2H_2O\,, \tag{4.4}$$

$$C_2H_6 + \frac{7}{2}O_2 = 2CO_2 + 3H_2O\,. \tag{4.5}$$

Table 4.3: Natural gas composition in molar fraction.

Components	Molar Fraction (%)
CH_4	98.57
C_2H_6	0.82
N_2	0.6
CO_2	0.01

For the turbine, it is modelled as an isentropic process, and its output power is calculated by [75]:

$$W_{out,\,ideal} = -\left(\frac{\gamma}{\gamma-1}\right)P_{in}V'\left[\left(\frac{P_{out}}{P_{in}}\right)^{(\gamma-1)/\gamma} - 1\right], \tag{4.6}$$

$$W_{out} = \eta_t W_{out,\,ideal}\,, \tag{4.7}$$

where, $W_{out,\,ideal}$ is the turbine output power under ideal isentropic condition, W_{out} is the real turbine output power, and η_t is the isentropic efficiency.

The isentropic efficiency of the turbine modelled as [84]:

$$\eta_t = 0.91[1 - 0.3(1-\dot{n}_t)^2](\dot{n}_t / \dot{m}_t)(2 - \dot{n}_t / \dot{m}_t)\,, \tag{4.8}$$

where, $\dot{n}_t$ is the ratio of rotating speed to its designed value, and $\dot{m}_t$ is the ratio of mass flow rate to its designed value.

The temperature of the turbine outlet stream is given by [75]:

$$T_{out} = T_{in} - \eta_t T_{in}\left[1 - \left(\frac{P_{out}}{P_{in}}\right)^{(\gamma-1)/\gamma}\right]. \tag{4.9}$$

4.3.2 HRSG Section Modelling

The HRSG is modelled as a group of heat exchangers in this study. The exhaust gas from the gas turbine enters the HRSG, where the waste heat is recovered to produce steam at different pressures (HP, IP and LP). The heat exchanger dynamic model is developed based on energy and mass balance equations. The heat exchanger is modelled in one dimension which is parallel to the working fluid flow direction. It is assumed that the pressure drops of both fluids are not considered.

The energy conservation equation is given by [58, 59]:

$$V\rho\frac{\partial h}{\partial t}+\dot{m}\frac{\partial h}{\partial z}dz=\dot{Q}+W\,, \tag{4.10}$$

and mass balance is described by [44]:

$$\frac{\partial \rho}{\partial t}+\frac{\partial \rho v}{\partial z}=0\,, \tag{4.11}$$

where, V is the volume, ρ is the density, h is the enthalpy, t is the time, $\dot{m}$ is the mass flow rate, z is the axial distance, $\dot{Q}$ is the heat power, W is the work done on the fluid, and v is the working fluid velocity.

The heat power can be calculated by:

$$\dot{Q}=UA\Delta T\,, \tag{4.12}$$

where, U is the heat transfer coefficient, A is the heat exchange area, ΔT is the temperature difference between hot side and cold side.

The heat transfer coefficient can be calculated by [75]:

$$U=U_{design}(\frac{n}{n_{design}})^{0.7}\,, \tag{4.13}$$

where, n is the molar flow rate and the subscript *design* denotes values at rated load condition.

The momentum balance is neglected in this study, then

$$V\rho\frac{\partial h}{\partial t} = Q + \dot{m}_i h_i - \dot{m}_o h_o \,, \tag{4.14}$$

where, subscript i is inlet, and o is the outlet.

The change of enthalpy can be calculated by [85]:

$$\Delta h = h_2 - h_1 = \int_1^2 c_p(T)dT \,, \tag{4.15}$$

$$h_2 - h_1 = c_{p,avg}(T_2 - T_1) \,, \tag{4.16}$$

where, c_p is the heat capacity.

Therefore, the change of fluid temperature can be calculated by:

$$\frac{dT}{dt} = \frac{UA\Delta T + mc_p(T_i - T_o)}{V\rho c_p} \,. \tag{4.17}$$

In order to capture the dynamics of the heat exchanger, it is discretized into several zones, each of which obey both energy and mass conservation equations [59], as shown in Figure 4.7. In this study the heat exchangers are discretized into 15 cells, since it turns out to be a sound trade-off between computation time and calculation accuracy. This model is only used for load-following simulation rather than start-up or shut-down simulation. As the fluid temperature in each heat exchanger do not change dramatically, so the metal temperature is not considered at this stage.

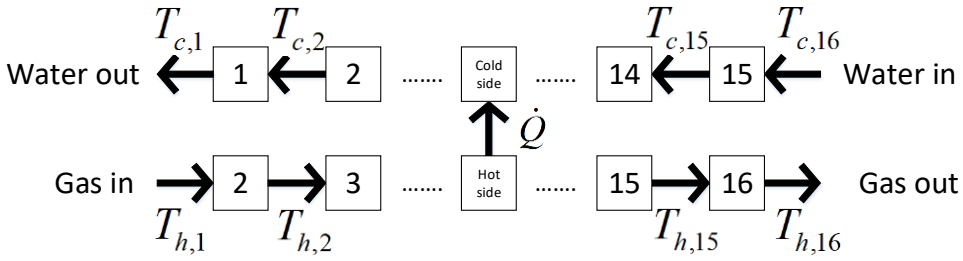

Figure 4.7: Cell model of the counter current heat exchanger.

For each cell, the heat exchange area (A_i), and the volume (V_i) can be presented as [59]:

$$A_i = \frac{A}{N}, \tag{4.18}$$

$$V_i = \frac{V}{N}, \tag{4.19}$$

where, N cells, subscript i is the cell number.

The instantaneous temperature change of cold stream can be calculated by:

$$\frac{dT_{c,i}}{dt} = \frac{UA_i(T_{h,i+1} - T_{c,i}) - m_c c_{p,ci}(T_{c,i} - T_{c,i+1})}{V_i \rho_{c,i} c_{p,ci}}, \tag{4.20}$$

where, subscript h is the hot stream and c is the cold stream.

Similarly, the instantaneous temperature change of hot stream can be calculated by:

$$\frac{dT_{h,i}}{dt} = \frac{-UA_i(T_{h,i} - T_{c,i-1}) + m_h c_{p,hi}(T_{h,i-1} - T_{h,i})}{V_i \rho_{h,i} c_{p,hi}}. \tag{4.21}$$

The water pump is used to increase the pressure of water in the LP, IP and HP circuits of the water-steam cycle. The flowsheet connectivity diagram is shown in Figure 4.8.

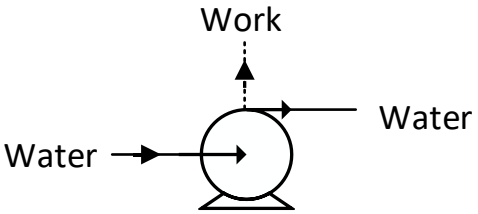

Figure 4.8: Pump flowsheet connectivity diagram.

The power requirement of the water pump (W_{pump}) is given by [75]:

$$W_{pump} = \frac{1}{\eta} \dot{m}_{water} V'(P_o - P_i), \tag{4.22}$$

where, η is the efficiency, $\dot{m}_{water}$ is the water mass flow rate, V' is the specific volume, P_o is the outlet pressure, and P_i is the inlet pressure.

In the simulation, the thermodynamic properties (e.g. heat capacity and density) of the exhaust gas and water/steam are updated at every time-step based on current temperature and pressure using Aspen Plus's thermodynamic database.

4.3.3 Steam Turbine Section Modelling

Three levels of steam generated by the HRSG are used to spin the corresponding three steam turbines: HPTB, IPTB, and LPTB. The development of the steam turbine models uses the same thermodynamic principles as the gas turbine model development. The actual isentropic efficiency of steam turbine varies with mass flow rate and can be determined by Figure 4.9 [48]. The nominal isentropic efficiency of HPTB, IPTB, and LPTB used in the simulation were 0.88, 0.88 and 0.85, respectively.

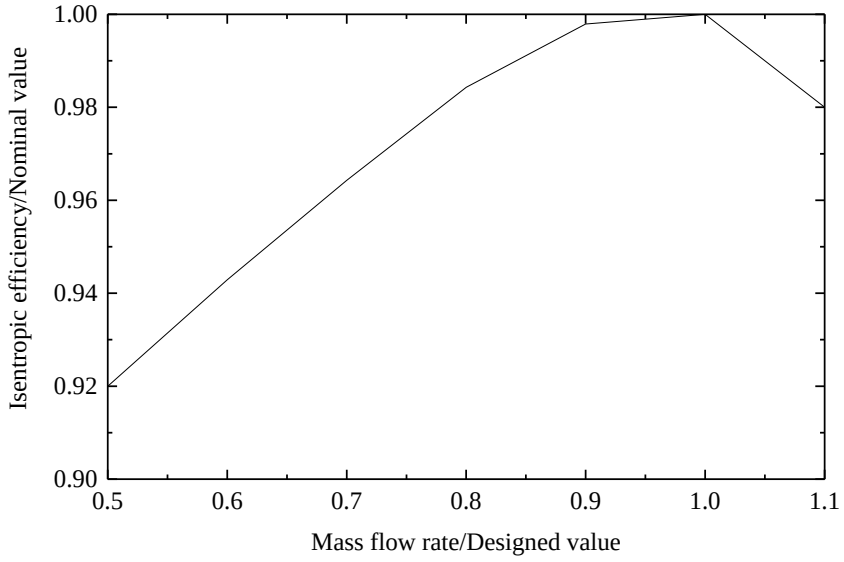

Figure 4.9: Steam turbine isentropic efficiency curve.

4.3.4 Physical Properties

The choice of an appropriate physical property method is significant for the accuracy of the simulation. The physical property method is a collection of estimation methods and models to calculate several thermodynamic and transport

properties for thermodynamic equilibrium (flash calculation) and process streams. The thermodynamic properties include fugacity, enthalpy, entropy, Gibbs free energy and volume. The transport properties include viscosity, thermal conductivity, diffusion coefficient and surface tension. Moreover, Aspen Plus stores a large database of interaction parameters which are used with mixing rules to estimate mixtures properties. In this model, the PR-BM property method is chosen for the gas cycle calculation [86], and STEAMNBS property method is chosen for the water-steam cycle calculation [87].

In Aspen plus, the PR-BM property method uses the Peng Robinson cubic equation of state with the Boston-Mathias alpha function for all thermodynamic properties. The PR-BM property method is recommended for hydrocarbon processing applications such as gas processing, refinery, and petrochemical processes.

The Peng Robinson equation is:

$$P = \frac{RT}{V_m - b} - \frac{a}{V_m(V_m + b) + b(V_m - b)} \quad , \tag{4.23}$$

where, a , b and c are component specific parameters, the value of these parameters are stored in Aspen Plus database for pure components or calculated using mixing rules for mixtures. V_m is the molar volume calculated by the equation of state without the correction, T is the temperature, and R is the ideal gas constant.

The STEAMNBS property method uses 1984 NBS/NRC steam table correlations for thermodynamic properties, and the international association for properties of steam (IAPS) correlations for transport properties. The STEAMNBS property method is used for pure water and steam, and the temperature ranges are from 273.15K to 2000K.

The Aspen Properties monitor routines have to be called to calculate the physical properties of the working fluid. For the gas or air, the physical properties are calculated by calling sequence “PPMON_VMTHRM (T, P, Y, N, IDX, NBOPST, KDIAG, KBASE, KPHI, KH, KS, KG, KV, PHI, HMX, SMX, GMX, VMX, DPHI,

CPMX, DSMX, DGMX, DVMX, KER)". For the pure water, the physical properties are calculated by calling sequence "PPMON_LTHRM (T, P, N, IDX, NBOPST, KDIAG, KBASE, KPHI, KH, KS, KG, KV, PHI, H, S, G, V, DPHI, DH, DS, DG, DV, KER)". For the saturated water, the physical properties are calculated by calling sequence "FLSH_PFLASH (KODE, SPEC1, SPEC2, F, N, IDX, NPHASE, KPHASE, MAXIT, TOL, NBOPST, LDIAG, KDIAG, KBASE, TEMP, PRES, HTOTAL, VFRAC, BETA, X, X1, X2, Y, EKVL, EKVL2, IRSTRT, RETEN, IRETEN, KER)". For the pure vapour, the physical properties are calculated by calling sequence "PPMON_VTHRM (T, P, N, IDX, NBOPST, KDIAG, KBASE, KPHI, KH, KS, KG, KV, PHI, H, S, G, V, DPHI, DH, DS, DG, DV, KER)". The list description for the parameters in the above routines is shown in Table 4.4 [88].

Table 4.4: Descriptions for parameters.

Variable	Description
BETA	Moles first liquid/moles total liquid.
CPMX	Heat capacity for a vapor mixture.
DG	Array of partial derivatives for pure component Gibbs free energies with respect to temperature.
DGMX	Partial derivative of mixture Gibbs free energy with respect to temperature.
DH	Array of partial derivatives for pure component enthalpies with respect to temperature.
DPHI	Array of partial derivatives with respect to temperature of fugacity coefficients, for pure components or for components in mixture.
DS	Array of partial derivatives for pure component entropies with respect to temperature.
DSMX	Partial derivative of mixture entropy with respect to temperature.

DV	Array of partial derivatives for pure component molar volumes with respect to temperature.
DVMX	Partial derivative of mixture molar volume with respect to temperature.
EKVL	Vapor-liquid K-values.
EKVL2	Vapor-liquid K-values for second-liquid phase.
F	Total mixture mole fraction array.
G	Array of pure component Gibbs free energies.
GMX	Mixture Gibbs free energy.
H	Array of pure component enthalpies.
HMX	Mixture enthalpy.
HTOTAL	Total mixture enthalpy per mole feed.
IDX	Component index array.
IRETEN	Integer retention array.
IRSTRT	Retention flag.
KBASE	Thermodynamic reference state code.
KDIAG	Diagnostic level.
KER	Not used.
KG	Gibbs free energy calculation code.
KH	Enthalpy calculation code.
KODE	Flash option code.
KPHASE	Phase when NPHASE = 1.
KPHI	Fugacity coefficient calculation code.
KS	Entropy calculation code.
KV	Molar volume calculation code.
LDIAG	Flash diagnostic level.
MAXIT	Maximum number of iterations.
N	Number of components present.
NBOPST	Property Methods array.
NPHASE	Number of phases in PHASES.

P	Pressure.
PHI	Array of fugacity coefficients for pure components or components in mixture.
PRES	Pressure.
RETEN	Real retention array.
S	Array of pure component entropies.
SMX	Mixture entropy.
SPEC1	First specified variable.
SPEC2	Second specified variable.
T	Temperature.
TEMP	Temperature.
TOL	Convergence tolerance.
V	Array of pure component molar volumes.
VFRAC	Moles vapor/moles total mixture.
VMX	Mixture molar volume.
X	Liquid mole fraction array.
X1	Liquid 1 mole fraction array.
X2	Liquid 2 mole fraction array.
Y	Vapor mole fraction array.

4.3.5 Dynamic Simulation Implementation

This section presents how to implement dynamic simulation in Aspen Plus. The method proposed can also be used for other Aspen Plus steady state models to convert to dynamic models. The procedures are shown in Figure 4.10.

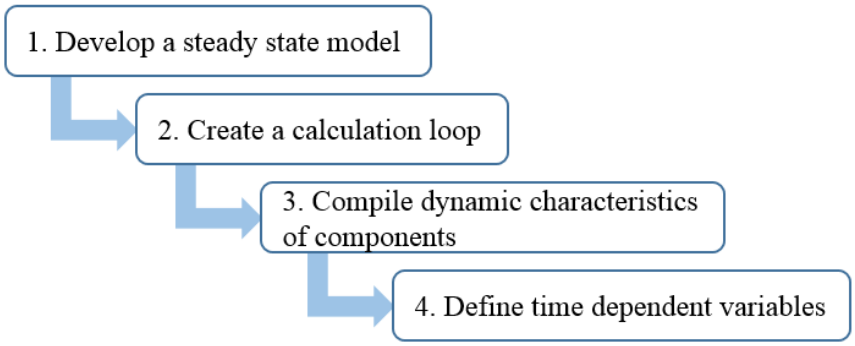

Figure 4.10: Procedures to derive the dynamic model.

The first step of the dynamic modelling is to develop the steady state model. After that, a calculation loop is created by using the built-in 'calculator' block to implement the dynamic model. In the 'calculator', there are three kinds of variables, they are import variable, export variable and tear variable, as shown in Figure 4.11. A calculation loop "$OLVER01" is created, by defining a tear variable, as shown in Figure 4.12, where all the components are included. Based on tear variable (see Appendix), information is passed from unit to unit until new value of the tear variable is computed. The calculations repeat until the convergence tolerance is satisfied. The tolerance is set to a very small value (1e-10), so the calculation loop will repeat again and again.

The sequential modular approach is used for dynamic simulation of the CCGT power plant. It takes modules as the basic computational unit and through sequential calculation of each module solves the model. The feature of modular based systems is that the system provides input parameter values to the module which returns the corresponding output. The output of upstream modules can be used as the input for the downstream modules. The sequential modular approach is widely used for process modelling since it improves the accuracy of the model and reduces the difficulty of system modelling and solving [89]. The calculation sequence is shown in Figure 4.12 where the calculation starts from the compressor ("COMP"), followed by fuel supply ("FUEL"), the combustion chamber ("COMB"), gas turbine ("EXP"), heat exchangers, steam turbines, etc. The last module is the

"RESULTS", after this module, a new calculation loop will be started from "COMP".

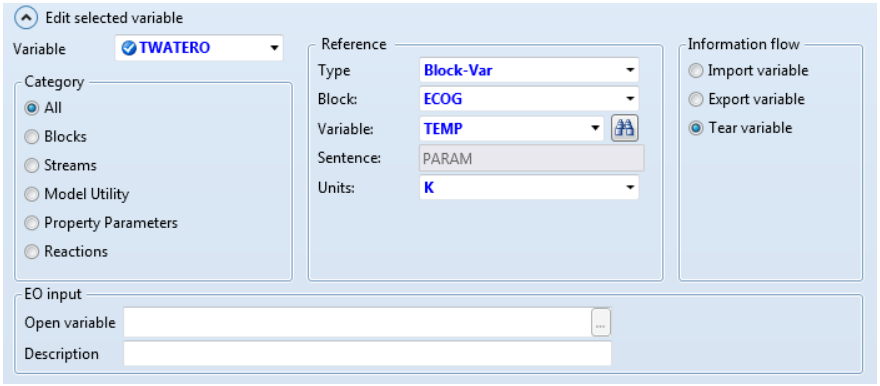

Figure 4.11: Variable definition.

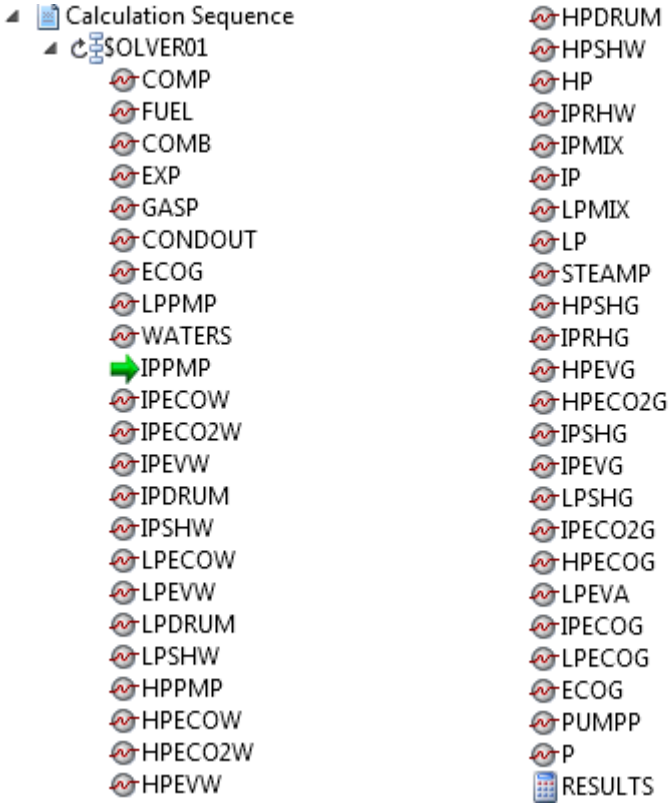

Figure 4.12: Calculation loop of the CCGT power plant.

For the next step, the dynamic characteristics of components are coded to Aspen Plus, such as compressor efficiency, turbine efficiency, etc, which are described in subsection 4.3. Finally, time dependent variables are defined in external FORTRAN

subroutines or “calculator”. In this model, the time dependent variables are dT is the Equation 4.20 and 4.21. Based on the time dependent variables, the simulated time is defined as 1 second on each circulation.

4.4 CCGT Power Plant Performance

The performance of the developed CCGT power plant is presented in this subsection. Based on the data published [90, 91], the detailed comparison of the three CCGT power plant models regarding operation data is listed in Table 4.5. The first CCGT power plant is modelled in GE’s GateCycle software, which can be used for detailed engineering design [90]. The second model is developed in Aspen HYSYS, which is a powerful process simulation package with a large library of physical properties [91]. The last model is developed in Aspen Plus, which is the model designed in the thesis. According to Table 4.5, the main parameters of the Aspen Plus model are close to the GateCycle and HYSYS model. Due to differences of the heat exchangers arrangement in the HRSG, some parameters are slight differences between these three models. The main difference appears in the HPTB inlet pressure because of different HRSG structures and steam turbine. Although there are slight deviation between these three models, the simulated results are all in a reasonable range.

The mass flow rate of feed air and feed water will be different for each load condition. With the increasing of load demand, the mass flow rate of feed air and feed water are also increased to meet the load demand. The compressor mass flow rate of Aspen Plus model for different load conditions is plotted in Figure 4.13. The HPTB, IPTB and LPTB mass flow rates are plotted in Figure 4.14. According to Figure 4.3, the feed water is separated into three parts after flowing out of deaerator. Three pressure levels of steam are produced by HRSG, they are HP, IP and LP steam. The HP steam pass through HPTB, the outlet steam of HPTB is mixed with the IP steam flows into IPTB, the outlet steam of IPTB is then mixed with the LP

steam flows into LPTB. Therefore, the mass flow rate of HPTB is lower than IPTB which is lower than LPTB, as shown in Figure 4.14.

Table 4.5: Comparison of three CCGT power plant models at rated load condition.

Plant data		GateCycle [90]	Aspen HYSYS [91]	Aspen Plus
Gas turbine cycle	Compressor inlet temperature (K)	288	288	288
	Power for compressor (MW)	283.2	-	301.2
	GT turbine inlet temperature (K)	1767.5	1601	1547
	Power from GT turbine (MW)	569.6	-	585.7
HP steam turbine	Flowrate (kg/s)	80	-	84
	Inlet temperature (K)	820	838	818
	Inlet Pressure (bar)	110	98.8	140
IP steam turbine	Flowrate (kg/s)	89.9	-	99
	Inlet temperature (K)	816	570	671
	Inlet Pressure (bar)	25	24	25
LP steam turbine	Flowrate (kg/s)	99.8	-	108
	Inlet temperature (K)	559.1	568	504
	Inlet Pressure (bar)	4.2	4	6
Plant power generation (MW)		420	393	420

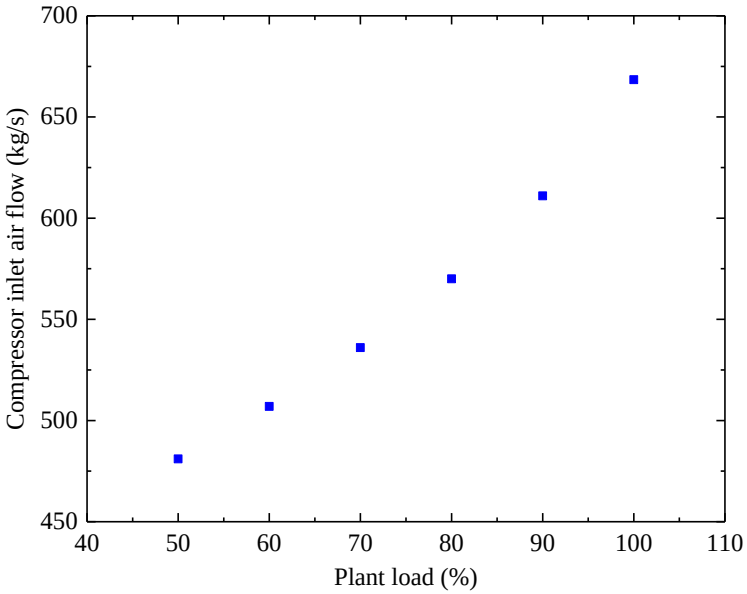

Figure 4.13: Compressor mass flow for different load conditions.

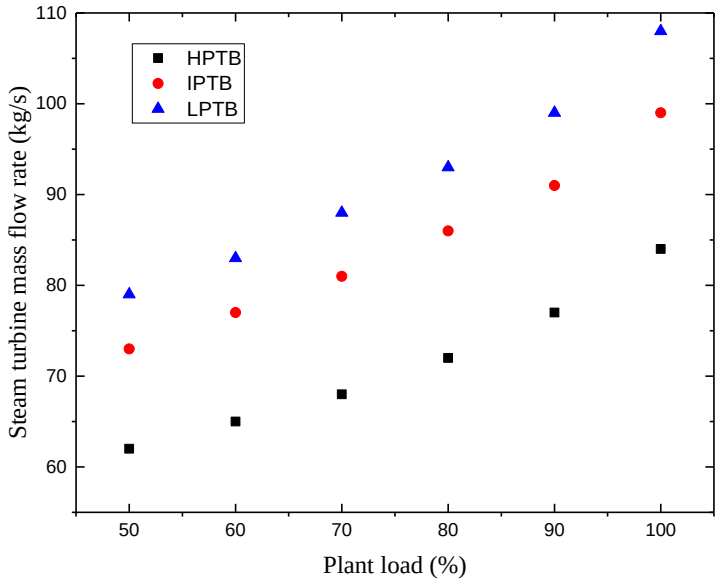

Figure 4.14: Steam turbine mass flow for different load conditions.

4.5 CCGT Power Plant Dynamic Simulation

A dynamic simulation of the developed CCGT power plant model is conducted to present its dynamic performances. A load demand profile in 1500s is shown in

Figure 4.15, which is used as the target power for CCGT power plant. The simulated fuel supply, gas turbine output power, steam turbine mass flow rate and steam turbine output are plotted in Figure 4.16, 4.17, 4.18 and 4.19, respectively.

At the beginning, the CCGT power plant combusts 11.18 kg/s natural gas to generate 300 MW power. At 300 seconds, the load demand increases to 380 MW, the natural gas consumption starts increasing to 13.13 kg/s to meet the load demand, as shown in Figure 4.16. Due to the thermal inertia of water-steam cycle, the response speed of the steam turbine cycle is much lower than the gas turbine cycle. According to the simulation results, the gas turbine output power increases from 185.7 MW to 255.1 MW within a minute and a half. While the steam turbine takes around 6 minutes to reach the target value, as shown in Figure 4.19.

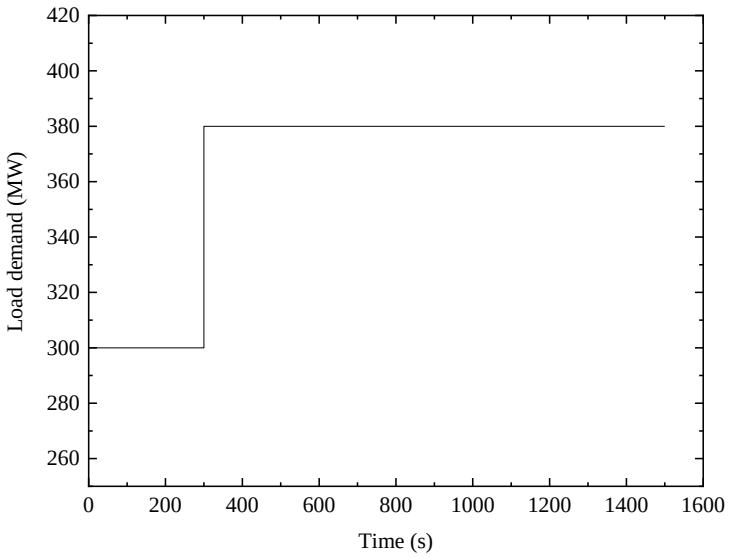

Figure 4.15: Load demand.

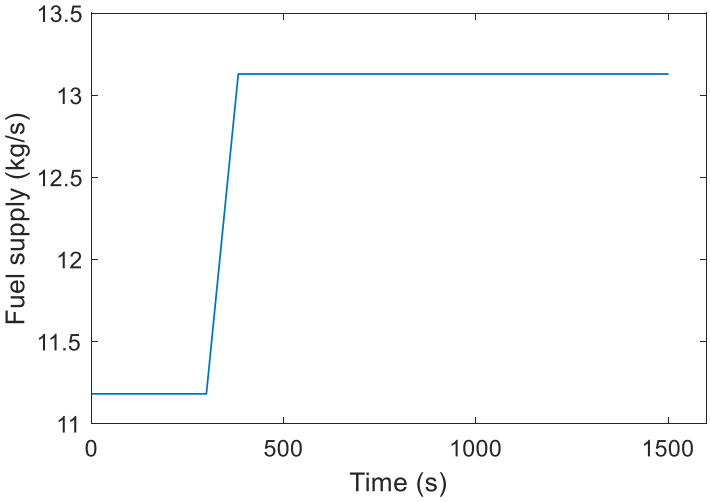

Figure 4.16: Fuel supply.

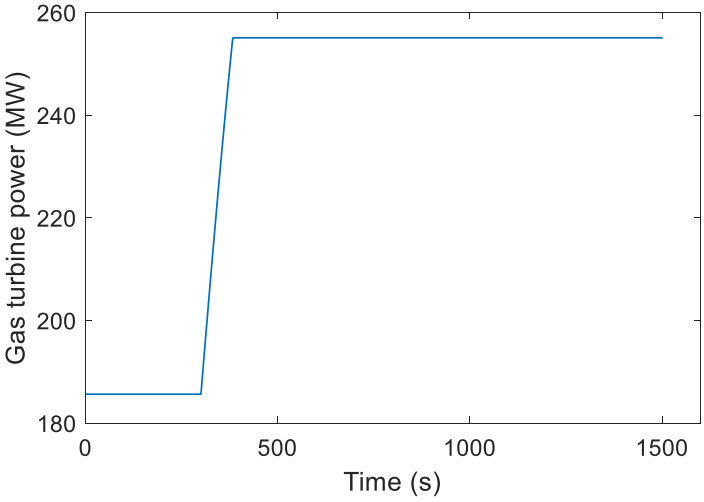

Figure 4.17: Gas turbine output power.

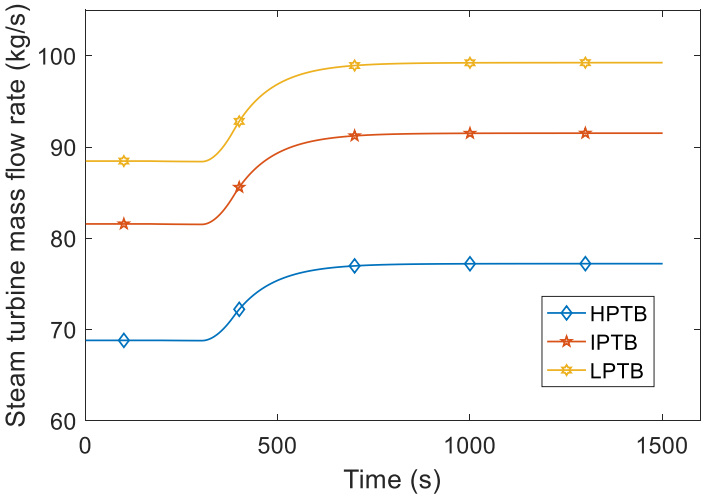

Figure 4.18: Steam turbine mass flow rate.

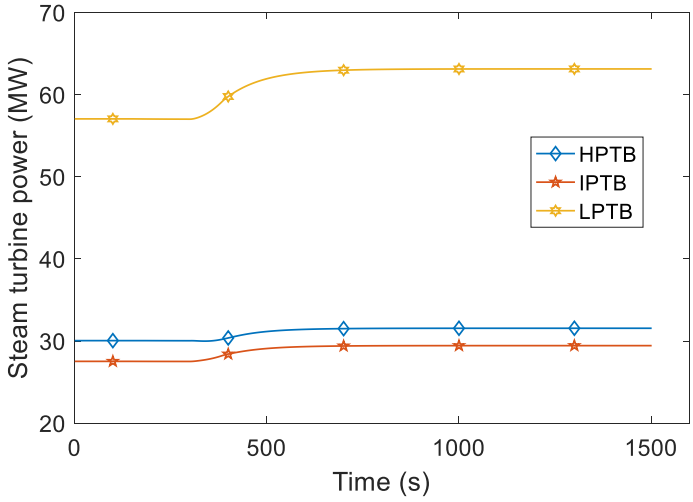

Figure 4.19: Steam turbine output power.

4.5 Summary

This chapter introduces the dynamic modelling of a 420 MW CCGT power plant in Aspen Plus. The mathematical descriptions of the individual sub-model representations in Aspen Plus are presented, including compressor, combustion chamber, gas turbine, heat exchanger, steam turbine, and others. The physical

properties calculation of gas cycle and water-steam cycle are chosen PR-BM property method and STEAMNBS property method, respectively.

At the rated operation condition, the power plant combusts 14.46 kg/s natural gas to generate 420 MW electrical power, in which 285 MW of the power is generated by the gas turbine, and 135 MW of the power is generated by steam turbines. The water-steam cycle consists of three pressure levels of steam (HP, IP and LP); each level of steam drives corresponding stream turbines.

The Aspen Plus model captures the full off-design details of the CCGT power plant such as, compressor efficiency map, turbine characteristics, flow-dependent variables and the like. Moreover, a novel modelling method is proposed to conduct whole system dynamic simulation in Aspen Plus by incorporating an external FORTRAN subroutine. The modelling strategies and solutions presented in this chapter is available to simulate any CCGT power plants in Aspen Plus.

Chapter 5-Study of CCGT Power Plant Integration with TES

5.1 Introduction

Combined-cycle power generation technology has been developed and served as an effective means for base load supply worldwide since the 1960s due to its inherent advantages in high efficiency and operational flexibility. Over the past 10 years, the capacity of intermittent renewable energy has increased dramatically, which has a significant impact on maintaining the balancing of the power generation and demand. This forces CCGT power plants into a role change: from baseload supply to fast response operating services.

It is extremely challenging to ensure CCGT power plants operate flexibly and also maintain their efficiency at the same time. Previous research focused on the control strategy and optimising the power generation process to improve operational flexibility. Although, these methods stabilized the gird dynamics and achieved short-term high profits, they will lead to a significant reduction in the lifetime of the power plant equipment [92]. Based on the CCGT power plant dynamic model introduced in Chapter 4, this chapter presents a feasibility study of the CCGT power plant combined with the cascaded latent heat storage (CLHS) for flexible plant operation.

This chapter starts with reviewing the TES technology development with regard to sensible heat storage, latent heat storage and chemical heat storage. It then describes the mathematical modelling of the CLHS system. Finally, the integration strategies and dynamic simulation of the CCGT power plant with CLHS are presented.

5.2 Review of TES systems

TES attracts people's attention since it provides numerous benefits for the industrial areas. For example, it corrects the disparity of thermal power generation and load

consumption, especially for smoothing the gap between the availability of solar resources and load demand. The performance of a TES system depends on the type of thermal storage, storage material selection and structure of TES unit. The TES system can be classified as sensible heat storage, latent heat storage and thermos-chemical heat storage. This section presents a review of TES systems.

5.2.1 Sensible Heat Storage

Sensible heat storage (SHS) accumulates thermal energy by increasing the temperature of the storage medium; therefore, the storage material without undergoes a phase change in the storage process. The amount of thermal energy stored depends on the heat capacity (c_p), the mass of material (m) and the temperature change. The amount of thermal energy stored (Q) may be given by the following equation [64]:

$$Q = \int_{T_i}^{T_f} mc_p dT \,, \tag{5.1}$$

where, T_i is the initial temperature and T_f is the final temperature.

The storage materials of SHS are divided into two categories: solid state or liquid state [69]. The most common used solid state material includes sand-rock minerals and metals, whereas liquid state material contains hot water, oil-based fluid and molten salts[69, 93].

SHS systems have been utilised for a significant number of applications, due to its characteristic of inexpensive and reliable. One of the common types of SHS is the hot water storage in modern homes for hot water supply. Besides, Hänchen et al. developed a model of the packed bed of rocks, which is used as the thermal storage system for air-based concentrated solar power plants [94].

SHS is one of the most popular thermal storage technologies because of its low cost. However, this technology offers very low energy density, and it suffers significant heat losses to the surroundings.

5.2.2 Latent Heat Storage

Latent heat storage (LHS) accumulates thermal energy by changing the phase of the material, which can be from solid to liquid or from liquid to gas. The enthalpy of phase transition is much higher than sensible heat; therefore, the LHS has higher energy density than SHS. The energy stored in mass (m) for a solid to liquid transition is calculated by [64]:

$$Q = \int_{T_i}^{T_m} mc_p dT + m\alpha l + \int_{T_m}^{T_f} mc_p dT \tag{5.2}$$

where, T_m is the phase change temperature, α is the fraction of the material experienced the phase change and l is the enthalpy of phase change.

The first term of the above equation is the sensible heat stored by the PCM temperature increase from the initial temperature to the phase change temperature. The second term is the energy stored by the latent heat which depends on the fraction of the material experienced the phase change. If the material is further heated after the phase change, the last term appears to represent the sensible heat of the liquid.

LHS has received numerous applications throughout the world, such as using PCMs for thermal management of Li-ion batteries [95], for energy saving of buildings [96], etc. Power plants may realise efficient and flexible operations via LHS system integration, including coal-fired power plant [15], CHP power plant, CCGT power plant and solar thermal power plant [97]. The integration of LHS with CAES has been proposed to improve the cycle-to-cycle efficiency [98].

Compared with SHS, LHS can store and release a large amount of heat in an isothermal process, due to the phase change. However, the conductivity of the most PCMs is relatively low, which affects the heat transfer rate in the material and the performance of thermal storage. To overcome this drawback, the enhancement of PCMs conductivity has been the focus of many researchers in recent decades. Ji et

al. proposed a method to improve the thermal conductivity of PCMs by using continuous ultrathin-graphite foams to fabricate ultrathin-graphite foams PCM composites [99]. The microencapsulated PCMs with an inorganic shell provides a significant enhancement of the thermal conductivity [100]. Also, Elbahjaoui & Qarnia demonstrated that the use of nanoparticle-enhanced PCM improves the heat transfer rate compared with the basic PCM [101]. Besides improving the property of material, using the rectangular fin in a triplex tube heat exchanger is an efficient way to reduce the melting duration of PCMs [102]. The use of fins arranged orthogonally to the pipe provides additional heat transfer surface in LHS systems, which improves the heat transfer rate in LHS units [64]. A tree shaped fins is proposed to enhance the performance of a LHS system and a shape optimisation strategy is presented in [103].

5.2.3 Thermo-chemical Heat Storage

In thermo-chemical heat storage systems, heat is released or absorbed through the reversible exothermic/endothermic chemical reactions [104]. Thermo-chemical heat storage systems have higher energy density than SHS and LHS technologies. Besides, in the thermo-chemical systems the thermal energy is stored as chemical potential; therefore it does not degrade over time during storage, which makes it a possible technology for long-term storage [104]. Although thermo-chemical heat storage system has these advantages, it is the least investigated technology. There are some impediments hindering the development of thermo-chemical storage system, including heat transfer rate, chemical stability, reversibility and cost [66].

5.3 Dynamic Modelling of Latent Heat Storage system

This section presents the designed CLHS dynamic model, which consists of four PCM layers, including NaCl&$CaCl_2$ (PCM1), $MgCl_2$&NaCl&KCl (PCM2), LiCl&LiOH (PCM3) and $LiNO_3$&$NaNO_3$&KCl (PCM4). These PCM layers are

arranged in the direction of discharging flow (from left to right) as shown in Figure 5.1 and their thermodynamic properties are listed in Table 5.1.

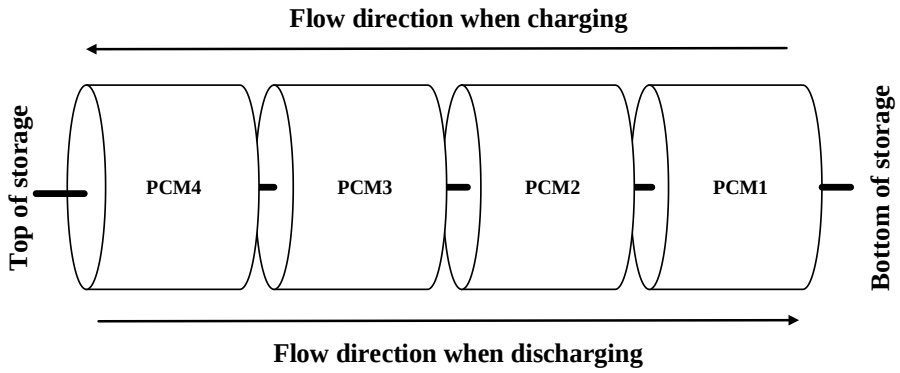

Figure 5.1: CLHS system with 4 PCMs.

The consideration for such an arrangement is due to the requirement of fast heat absorption or release during the charging and discharging processes. With time, the temperature of PCM is rising, during the charging process. Therefore, the temperature difference decreases in the flow direction of the working fluid in a single PCM layer and results in a decrease in the heat transfer rate and thereby affect the performance of the storage unit. The multiple PCM layers with different melting point are cascaded in decreasing order of phase change temperature, so that the temperature difference between PCM layers and working fluid can be maintained as the temperature of working fluid is decreases, during the charging process [64]. This is because the latent heat is much higher than sensible heat. Hence, the material temperature could sustain at melting point for quite long and store a lot of heat. For the discharging operation, the heat-transfer fluid flows in the opposite direction so that the PCM layers are arranged in ascending order of phase change temperature, in this way the temperature difference between the PCM layers and the heat transfer fluid can be maintained.

The basic structure of the above CLHS system consists of two vertical concentric tubes filled with four cascaded PCM layers in between, as shown in Figure 5.2, with a radius of 0.0215 m for the inner tube and 0.043 m for the outer tube, a wall thickness of 0.0015 m, and a height of 20 m (5m for each PCM layer), as shown in

Figure 5.3 [105]. The entire CLHS system consists of 5600 sets of such concentric tubes in parallel.

Table 5.1: Thermophysical properties of PCMs [68].

Material	Composition, wt%	Melting temp., K	Latent heat, J/g	Specific heat, J/(g·K)	Density, g/cm^3	Conductivity, W/(m·K)
PCM1	33 (NaCl) 67 ($CaCl_2$)	773	280	1	2.16	1.02
PCM2	63 ($MgCl_2$) 22.3 (NaCl) 14 (KCl)	658	461	0.96	2.25	0.95
PCM3	37 (LiCl) 63 (LiOH)	535	485	2.4	1.55	1.1
PCM4	55.4 ($LiNO_3$) 4.5 ($NaNO_3$) 40.1 (KCl)	433	266	1.4	2.21	1

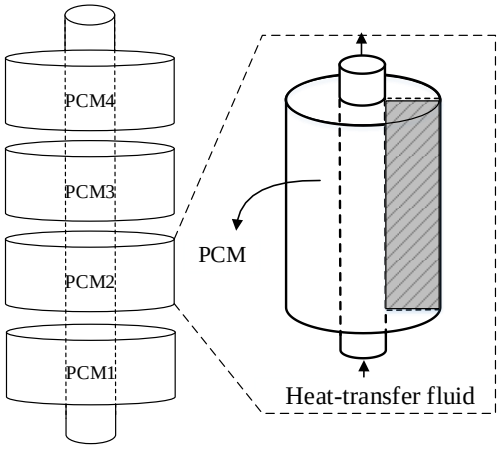

Figure 5.2: Structure of a single CLHS set.

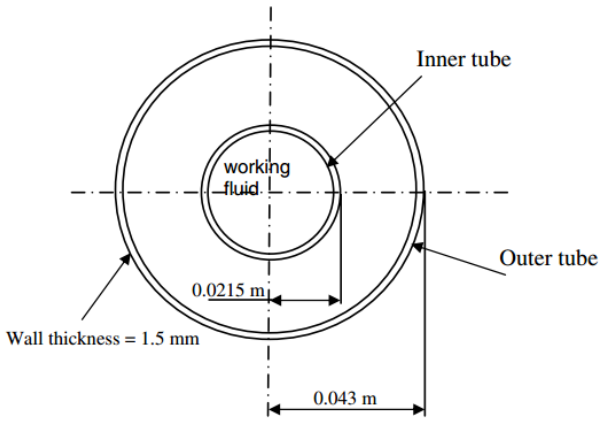

Figure 5.3: The cross sectional view of the concentric tubes [105].

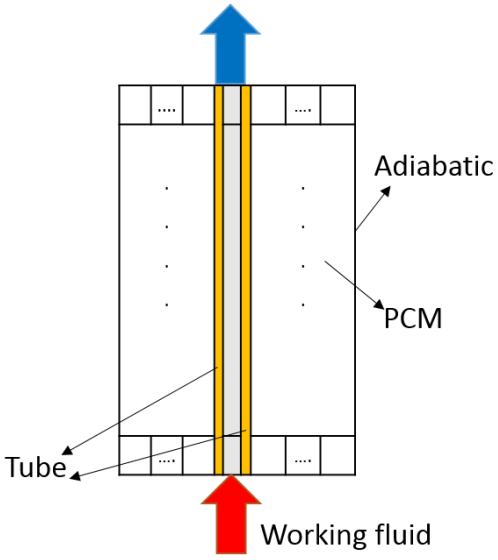

Figure 5.4: Vertical section view.

The vertical section view of the concentric tubes is shown in Figure 5.4. In the CLHS system, the heat transfer process is coupled with heat convection and heat conduction. Heat transfer fluid transfers heat to the inner tube by means of heat convection. For the heat transfer from the inner tube to the PCM and the heat diffusion in the PCM, the heat transfer is by means of heat conduction. The heat loss through the outer tube of the CLHS system is assumed to be negligible. In order to capture the dynamics of the thermal storage model, the shaded area in Figure 5.2 is discretized into 15×10 zones (15 in the vertical direction, and 10 in the radial direction).

The working fluid temperature is calculated by the heat convection equation:

$$\frac{dT_{f,i}}{dt} = \frac{-UA_i(T_{f,i} - T_{tube,i}) + \dot{m}_f c_{p,fi}(T_{f,i-1} - T_{f,i})}{V_i \rho_{f,i} c_{p,fi}}, \qquad (5.3)$$

where, subscript f is the working fluid, *tube* is the tube side and i is the cells number along working fluid direction. The heat transfer coefficient is taken as 300 $Wm^{-2}K^{-1}$ and 500 $Wm^{-2}K^{-1}$ for exhaust gas and steam, respectively.

The inner tube temperature is calculated by:

$$\frac{dT_{tube,i}}{dt} = \frac{UA_i(T_{f,i} - T_{tube,i}) - \dot{Q}_{cond}}{V_i \rho_{tube,i} c_{p,tube,i}}, \qquad (5.4)$$

where, $\dot{Q}_{cond}$ is the heat conduction from inner tube to PCM.

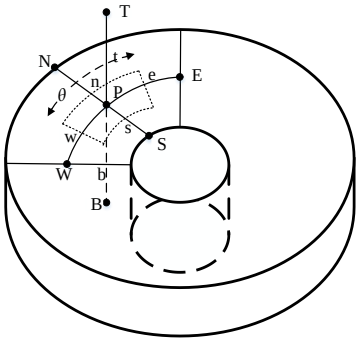

Figure 5.5: Three-dimensional heat conduction.

Figure 5.5 shows a portion of a three-dimensional heat conduction grid. In the cylindrical-coordinate system, the three-dimensional heat conduction equation for the grid point P in Figure 5.4 is given by [106]:

$$\rho c_p \frac{\partial T_P}{\partial t} = \frac{1}{r}\frac{\partial}{\partial r}(rk\frac{\partial T}{\partial r}) + \frac{1}{r}\frac{\partial}{\partial \theta}(\frac{k}{r}\frac{\partial T}{\partial \theta}) + \frac{\partial}{\partial z}(k\frac{\partial T}{\partial z}), \qquad (5.5)$$

where, ρ is the density, c_p is the heat capacity, T is the temperature, k is the heat conduction coefficient, r is the radius, θ is the angle, z is the length, t is the time and subscript P is the point P in the above figure.

Due to this cylinder is axisymmetric, the PCM temperatures around a circle are assumed same at the seam height of the cylinder. The temperature gradient in the

θ direction is assumed zero, therefore, the heat conduction equation in the cylinder is given by [107]:

$$\rho c_p \frac{\partial T_P}{\partial t} = \frac{1}{r}\frac{\partial}{\partial r}(rk\frac{\partial T}{\partial r}) + \frac{\partial}{\partial z}(k\frac{\partial T}{\partial z}). \tag{5.6}$$

The discretization equation is obtained by integrating the differential equations in the control volume over the time interval from t to $t+\Delta t$. The discretized equation is shown as follows:

$$\begin{aligned} a_P T_P = {} & a_N[fT_N + (1-f)T_N^0] + a_S[fT_S + (1-f)T_S^0] + a_T[fT_T + (1-f)T_T^0] + \\ & a_B[fT_B + (1-f)T_B^0] + [a_P^0 - (1-f)a_N - (1-f)a_S - (1-f)a_T - (1-f)a_B]T_P^0, \end{aligned} \tag{5.7}$$

where,

$$a_N = \frac{kr_n\Delta\theta\Delta z}{(\delta r)_n}, \tag{5.8}$$

$$a_S = \frac{kr_s\Delta\theta\Delta z}{(\delta r)_s}, \tag{5.9}$$

$$a_T = \frac{k0.5(r_n + r_s)\Delta\theta\Delta r}{(\delta z)_t}, \tag{5.10}$$

$$a_B = \frac{k0.5(r_n + r_s)\Delta\theta\Delta r}{(\delta z)_b}, \tag{5.11}$$

$$a_P^0 = \frac{\rho c_p \Delta V}{\Delta t}, \tag{5.12}$$

$$a_P = fa_N + fa_S + fa_T + fa_T + a_P^0, \tag{5.13}$$

where, f is a weighting factor, subscripts N and n are north side points, S and s are south side points, T and t are top side points, and B and b are bottom side points and superscript 0 means the previous time step value.

The ΔV is the control volume, which is given by:

$$\Delta V = 0.5(r_n + r_s)\Delta\theta\Delta r\Delta z. \tag{5.14}$$

In particular, $f = 0$ leads to the explicit scheme, $f = 0.5$ to the Crank-Nicolson scheme, and $f = 1$ to the fully implicit scheme. The explicit scheme is used to discretize the differential equation in this study, as follows:

$$a_P T_P = a_N T_N^0 + a_S T_S^0 + a_T T_T^0 + a_B T_B^0 + (a_P^0 - a_N - a_S - a_T - a_B) T_P^0 . \qquad (5.15)$$

This means that T_P is not related to other unknown temperatures such as T_N, T_S, T_T and T_B, but it is explicitly related to the known temperature T_N^0, T_S^0, T_T^0 and T_B^0. The main advantage of the explicit scheme is that it can solve partial differential equations non-iteratively by direct calculation [108]. However, for the explicit scheme, the time step (Δt) has to be small enough to ensure the simulation result accuracy [106] and the time step in this study is set to 0.001s.

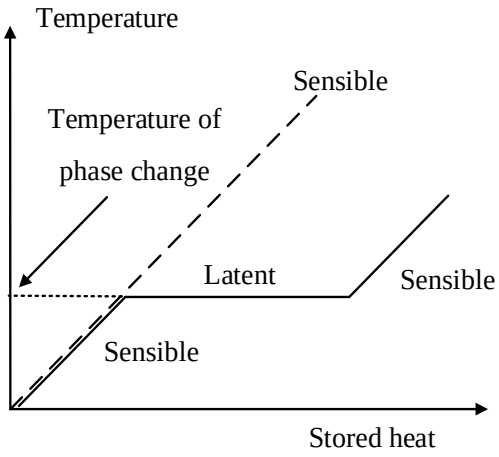

Figure 5.6: Phase change profile of PCM [109].

In the melting process, the PCM will absorb a large amount of heat which is stored as latent heat of fusion. However, during the phase changing process, the temperature of PCM keeps at the melting point [109], as shown in Figure 5.6. Therefore, the above equations are only used for the calculations under pure solid or liquid conditions.

To simulate the melting process, the following equation is introduced to calculate the enthalpy change during PCM melting [66, 67, 107]:

$$\rho \frac{\partial H_P}{\partial t} = \frac{1}{r}\frac{\partial}{\partial r}(rk\frac{\partial T}{\partial r}) + \frac{\partial}{\partial z}(k\frac{\partial T}{\partial z}), \quad (5.16)$$

where, H is the enthalpy.

The discretization equation is given by:

$$a_P'(H_P - H_P^0) = a_N T_N^0 + a_S T_S^0 + a_T T_T^0 + a_B T_B^0 + (-a_N - a_S - a_T - a_B)T_P^0, \quad (5.17)$$

where,

$$a_P' = \frac{\rho \Delta V}{\Delta t}. \quad (5.18)$$

The H_P^0 is the known enthalpy (previous time step enthalpy), and the discretization method is also an explicit scheme.

Due to the outer tube is assumed to be adiabatic, therefore there is no heat conduction on the boundary. Thus a_T is set as 0 for the topmost side of PCM, a_B is set as 0 for the bottommost side of PCM, and a_N is set as 0 for the outermost side of PCM.

5.4 CLHS Integration Strategies and System Simulation Studies

This section describes the integration strategies of a CCGT power plant with CLHS during the plant start-up, load-following, and standby operations, respectively. In particular, the start-up procedure is investigated, and the idea of thermal storage during plant start-up is proposed. This section examines how the integration of CLHS impacts on the dynamic performance of the plant regarding to the output power in the CLHS charging and discharging processes. This section presents how plant output power can be regulated through the CLHS charging and discharging processes. And also this section presents how to use the stored thermal energy to keep HRSG warm during plant standby for faster plant restart.

5.4.1 CLHS Integration Strategy during the Plant Start-up Process

In practice, although the gas turbine can start-up from cold state to rated load condition within 20 minutes, HRSG takes up to 170 minutes to reach its nominal load condition, depending on its initial temperature state at start-up, which includes hot, warm or cold [74]. During the start-up period, the critical fact is the rapid increase of operating parameters including mass flow rate, pressure and temperature. In that period, HRSG components are subject to high thermal stress, which is caused by the temperature gradient in metal. In order to reduce thermal stress of the HRSG, a bypass damper is adopted to control the mass flow rate of the exhaust gas for HRSG [110]. In fact, only a small portion of the exhaust gas flows into HRSG during the plant start-up period, and most of the exhaust gas is directly discharged to the atmosphere, resulting in energy loss. As described in [111], approximately 75% of the exhaust gas (513 kg/s in this study) from the gas turbine is discharged into the atmosphere for 25 minutes during the plant start-up (see Figure 5.7). The thesis proposes to capture the waste thermal energy by using CLHS, as shown in Figure 5.8. The key idea is to let the waste exhaust gas passing through the CLHS before discharging into the atmosphere. A filter is needed to remove the corrosive gases of the exhaust gas, as shown in Figure 5.8. In this way, the waste heat in the exhaust gas can be stored by PCM layers in the CLHS system. The exhaust gas pressure of CLHS outlet is assumed to be the same as the atmosphere.

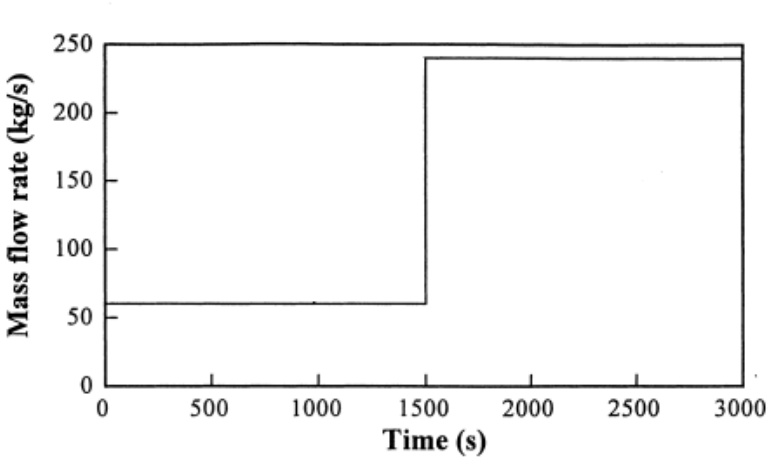

Figure 5.7: HRSG inlet mass flow rate [111].

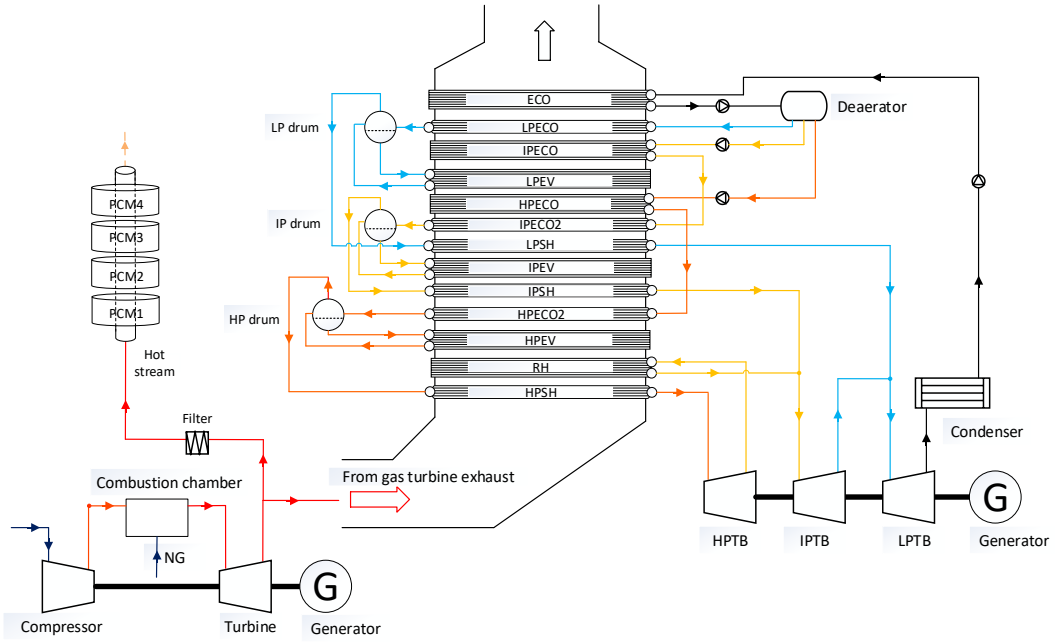

Figure 5.8: CLHS integration strategy for charging process.

As described in Section 5.3, there are 5600 sets of concentric tubes that are arranged in parallel. Accordingly, for each set of concentric tubes at the same height in the CLHS system, it can be assumed that they have the same temperature distribution due to their parallel structure [112]. Then the study of the entire CLHS system can be simplified as a study of one set of concentric tubes (see Figure 5.2).

Table 5.2: Parameter setting used to establish initial temperature distribution.

Layer	Start-up temp. (K)	Phase change temp. (K)	Initial temperature distribution
PCM4	387	433	Figure 5.9 (a)
PCM3	502	535	Figure 5.9 (b)
PCM2	596	686	Figure 5.9 (c)
PCM1	697	773	Figure 5.9 (d)

In order to establish a reasonable initial temperature distribution of each PCM such that a phase change process occurs in the simulation, a temperature below the phase change point of each PCM is used to start up the CLHS, as listed in Table 5.2. When

the local temperature reaches the phase change point, the temperature distribution of each PCM at that time is its initial temperature distribution, as shown in Figure 5.9. The temperature scale is presented in Figure 5.9 (d) that applies to all the sub-figures in Figure 5.9. The plotted figures demonstrate the temperature distribution of the shaded area of Figure 5.2. The phase change temperature is reached first in the bottom left corner as expected, for each PCM. The axial temperature distribution coincides with the flow of exhaust gas in the inner tube, while the radial temperature distribution also follows the heat diffusion from the inside to the outside of the PCM.

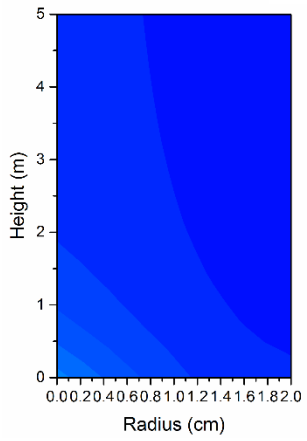

(a) PCM4

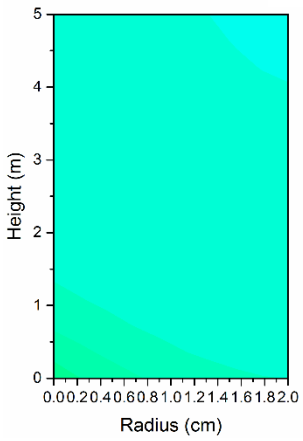

(b) PCM3

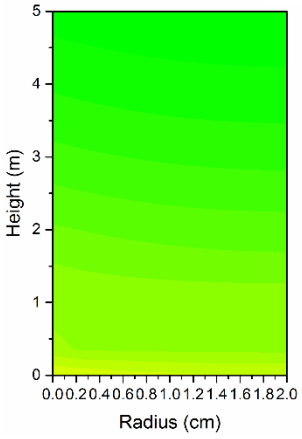

(c) PCM2

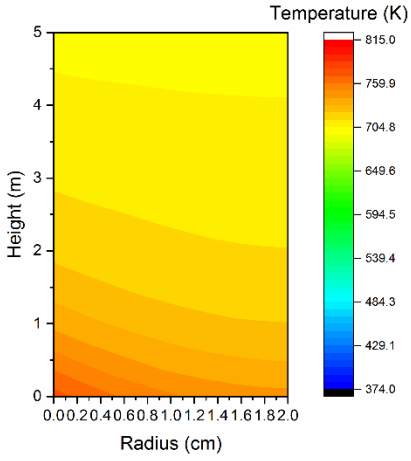

(d) PCM1

Figure 5.9: Initial temperatures distribution of different PCM layers.

After 1500 seconds of the charging process, the waste thermal energy in the exhaust gas is stored and further diffused in the PCMs. The lowest local temperature of each PCM layer reaches the phase change temperature. The PCM temperature in the area where the phase change process is finished continues to increase if the material is further heated. The updated temperature distributions of each PCM layer are shown in Figure 5.10. The left side temperature is higher than right side and the bottom side temperature is higher than top side because the exhaust gas flows from bottom to top on the left side of the plotted area (see Figure 5.1 and Figure 5.2).

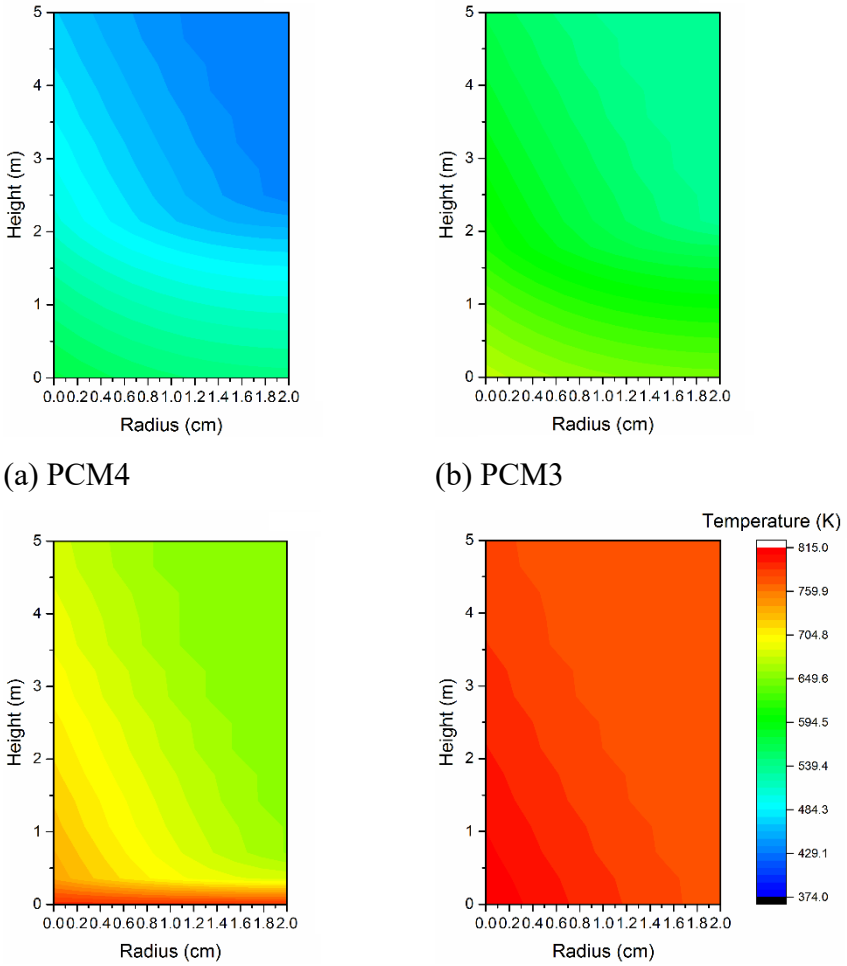

(a) PCM4 (b) PCM3

(c) PCM2 (d) PCM1

Figure 5.10: Temperature distribution of different PCM layers at the end of charging in the start-up operation.

As introduced in section 5.3, there are 150 zones which are calculated to represent the temperature distribution of each PCM layer. After charging for 1500s, the temperatures of PCM4 for each zone are shown in Table 5.3, and the stored latent heat is shown in Table 5.4. The temperatures in Table 5.3 are corresponding to the same positions in Figure 5. 10 (a). In order to explain the data clearly, each datum is given a unique coordinate. For example, in Table 5.3, the coordinate of left bottom number 569.6 is (1, 1), the coordinate of right top number 433 is (10, 15) and so on.

Table 5.3: Temperatures of PCM4 for each zones after charging (K).

467.01	459.76	453.29	447.5	442.25	437.46	433	433	433	433
471	463.2	456.13	449.67	443.71	438.18	433	433	433	433
474.9	466.8	459.6	453.16	447.4	442.18	437.42	433	433	433
479.72	471.15	463.39	456.33	449.84	443.84	438.25	433	433	433
483.95	474.96	466.92	459.73	453.29	447.49	442.25	437.46	433	433
489.36	479.93	471.42	463.68	456.6	450.07	444.01	438.34	433	433
494.13	484.21	475.32	467.34	460.15	453.67	447.81	442.48	437.58	433
500.01	489.64	480.3	471.82	464.07	456.95	450.35	444.21	438.45	433
505.66	494.97	485.51	477.22	470.04	463.99	459.1	455.41	452.95	451.73
517.04	507.31	498.95	491.86	485.94	481.13	477.37	474.61	472.82	471.94
529.36	520.56	513.03	506.65	501.34	497.04	493.69	491.24	489.65	488.87
540.78	532.85	526.06	520.32	515.54	511.66	508.65	506.44	505.01	504.31
551.22	544.12	538.03	532.87	528.59	525.11	522.41	520.43	519.14	518.52
560.79	554.47	549.04	544.45	540.64	537.54	535.13	533.37	532.22	531.67
569.6	564.03	559.26	555.22	551.86	549.13	547.01	545.46	544.45	543.96

Table 5.4: The latent heat of PCM4 for each zones after charging (J/g).

266	266	266	266	266	266	53.859	0	0	0
266	266	266	266	266	266	184.84	0	0	0
266	266	266	266	266	266	266	42.803	0	0
266	266	266	266	266	266	266	176.6	0	0
266	266	266	266	266	266	266	266	39.586	0
266	266	266	266	266	266	266	266	176.95	0
266	266	266	266	266	266	266	266	266	43.272
266	266	266	266	266	266	266	266	266	185.18
266	266	266	266	266	266	266	266	266	266
266	266	266	266	266	266	266	266	266	266
266	266	266	266	266	266	266	266	266	266
266	266	266	266	266	266	266	266	266	266
266	266	266	266	266	266	266	266	266	266
266	266	266	266	266	266	266	266	266	266
266	266	266	266	266	266	266	266	266	266

It can be seen from Table 5.3 that the temperature of the highlighted area is 433 K (phase change temperature); therefore, the material is in the melting process and the latent heat should between 0 to 266 J/g, as shown in Table 5.4. It should be noted that only eight positions of the highlighted area have latent heat, they are position (7, 15), (7, 14), (8, 13), (8, 12), (9, 11), (9, 10), (10, 9) and (10, 8). The latent heat of the rest positions is 0 J/g. The heat transfer relies on the temperature difference between two positions since the surrounding temperature of these points is same as themselves; therefore, the heat transfer is zero, and then the material is pure solid. For example, the temperature of the top, bottom, left and right sides of the position (9, 12) are all 433 K, and its latent heat is 0 J/g.

Table 5.5: Temperature and latent heat for difference positions.

Position	Left side temperature (K)	Latent heat (J/g)
(7, 15)	437.46	53.859
(7, 14)	438.18	184.84
(8, 13)	437.42	42.803
(8, 12)	438.25	176.6
(9, 11)	437.46	39.586
(9, 10)	438.34	176.95
(10, 9)	437.58	43.272
(10, 8)	438.45	185.18

The heat transfer rate depends on the temperature difference, and a larger temperature gap leads to bigger heat flux, as shown in Table 5.5. It may be noticed that the latent heat at position (7, 14), (8, 12), (9, 10) and (10, 8) are much higher than others, due to the heat conduction from the bottom side.

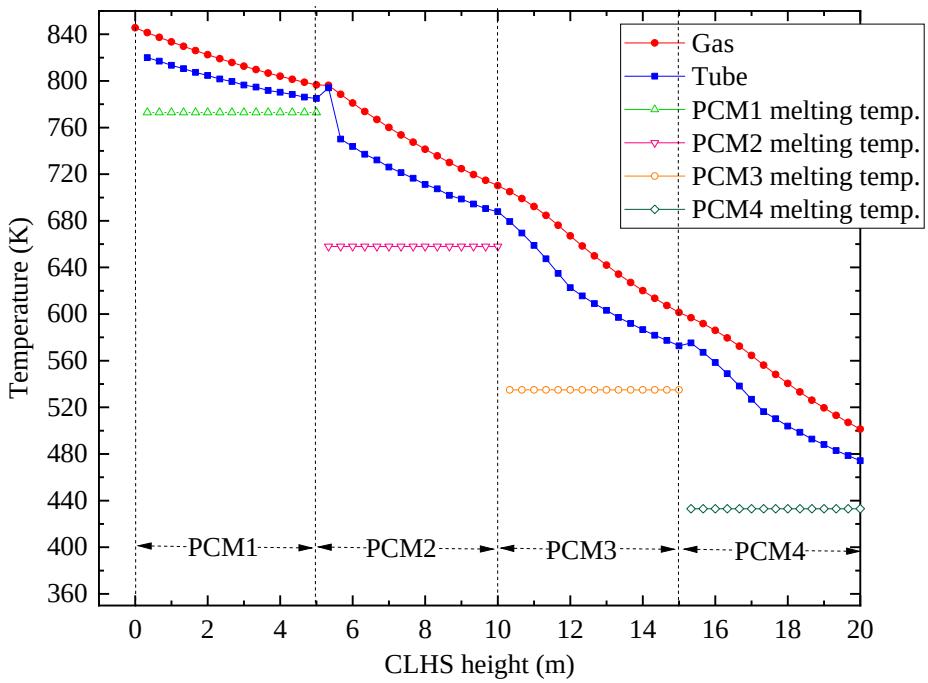

Figure 5.11: Gas and tube temperature after start-up charging process.

The inner tube temperature and the gas temperature are shown in Figure 5.11. After 25 mins charging, the bottom of PCM2 is liquefied, so the temperature of storage material and tube continues to increase, which caused a sharp of tube temperature, when gas flows into PCM2 form PCM1.

The stored thermal energy (Q_{tube}) in the tube is calculated by:

$$Q_{tube} = M_{tube} \cdot \Delta T \cdot c_p , \tag{5.19}$$

where, M_{tube} is the mass of tube, ΔT is the temperature change, and c_p is the heat capacity. In this study, the heat capacity of solid and liquid are supposed to have a same value.

The stored thermal energy of the PCM (Q_{PCM}) can be calculated by [66]:

$$Q_{PCM} = M_{PCM}[\Delta T \cdot c_p + l] , \tag{5.20}$$

where, M_{PCM} is the mass of PCM, ΔT is the temperature change, c_p is the heat capacity, and l is the latent heat.

The mass of each zone is calculated by:

$$M_{PCM,i} = \rho V = \rho\pi(r_i^2 - r_{i-1}^2)\Delta z , \tag{5.21}$$

where, subscript i is the cells number.

According to the calculation, a total of 327 GJ heat is stored in the CLHS system during the 1500 seconds and each PCM layer stores heat of 88 GJ, 101 GJ, 83 GJ, and 55 GJ, for PCM4, PCM3, PCM2, and PCM1, respectively.

5.4.2 TES Integration Strategy during Load-following Operation

In addition to avoiding the energy loss of the exhaust gas during the start-up process, the real-time output power of the CCGT power plant can be regulated within a certain range by the CLHS charging and discharging processes. The steam turbine

output power is related to the steam mass flow rate that is determined by the mass flow rate of gas turbine exhaust gas. In normal operation, the steam turbine output power has to follow the change of gas turbine working conditions. This section proposed the strategies to decouple the gas turbine and steam turbine energy interlink via TES integration.

During the off-peak time, part of the high-temperature exhaust gas is extracted from the gas turbine as a heat source for CLHS charging (same as the layout shown in Figure 5.8). As a result, less steam will be generated and the steam has a lower pressure. Then the power generated by the steam turbines will be reduced, while the gas turbine section is still operating under the rated load condition. Because of the equipment restrictions, the minimum steam turbine power is 66 MW when 363 kg/s exhaust gas bypass to the CLHS for thermal storage.

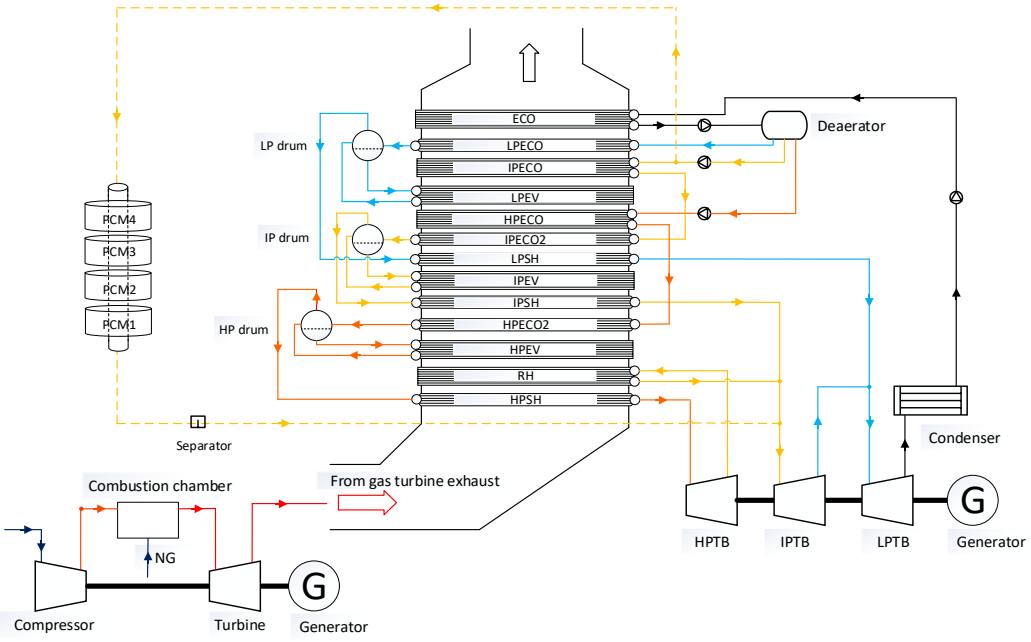

Figure 5.12: CLHS integration strategy for discharging during load-following operation.

On the other hand, during peak time, part of the feed water is extracted from the deaerator and fed into the CLHS. The extracted water undergoes the reverse process of charging and evaporates into high-temperature steam and then leaves CLHS as superheated steam, as shown in Figure 5.12. Once the generated steam meets the

turbine requirement, it will be fed into steam turbine. In order to produce dry steam for steam turbine, a separator is adopted to remove water droplets from steam. In this way, the stored thermal energy is discharged from CLHS to water-steam loop, thereby increase the output power of the steam turbines. Meanwhile, more water will be pumped into the water-steam loop and the maximum steam turbine output power could increase to 143 MW.

The simulated charging and discharging processes are described in the following part. Figure 5.13 shows designed pre-defined load demand dynamic change. At the beginning, the power plant operates at the rated load condition, and the total output power is 420 MW, in which 285 MW is from the gas turbine cycle, and 135 MW is from the steam turbine cycle. At 300 seconds, the load demand is reduced from 420 MW to 408 MW. At 2100 seconds, the load demand returns to 420 MW. At 2800 seconds, the load demand increases again from 420 MW to 428 MW, and it lasts 1200 seconds. During entire time, the gas turbine section operates at the rated load condition with a constant output power 285 MW. As a result, the real-time power output of the CCGT power plant is determined by the steam turbines.

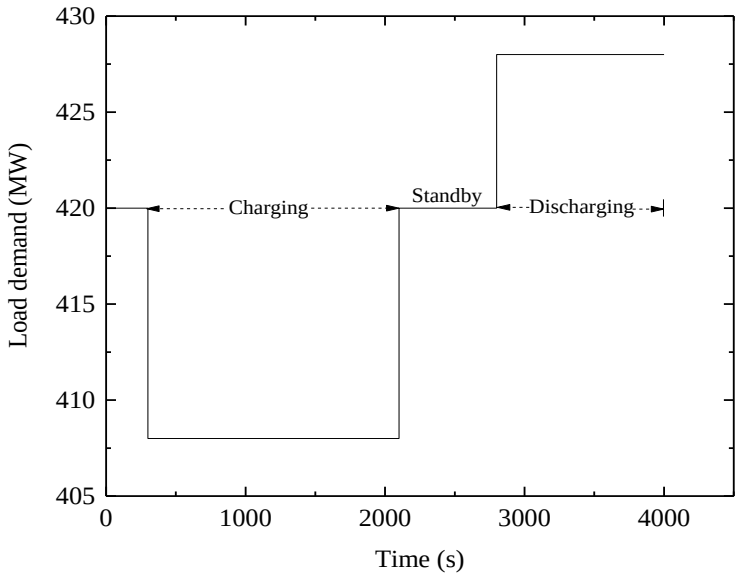

Figure 5.13: The desired load demand dynamics during load-following operation.

5.4.2.1 CLHS Charging Process

To meet the load demand reduction from 420 MW to 408 MW, the steam turbine output power is reduced from 135 MW to 123 MW, so 60 kg/s of exhaust gas is extracted from the gas turbine outlet and fed to the CLHS. This is under charging conditions so the extracted gas should flow from the bottom of the CLHS to its top, which is the direction along the decreasing order of PCMs melting point. It should be pointed out that the initial temperature distribution of the CLHS layers used for the load-following operation simulation is the same as the initial temperature distribution (Figure 5.9) in the start-up operation simulation.

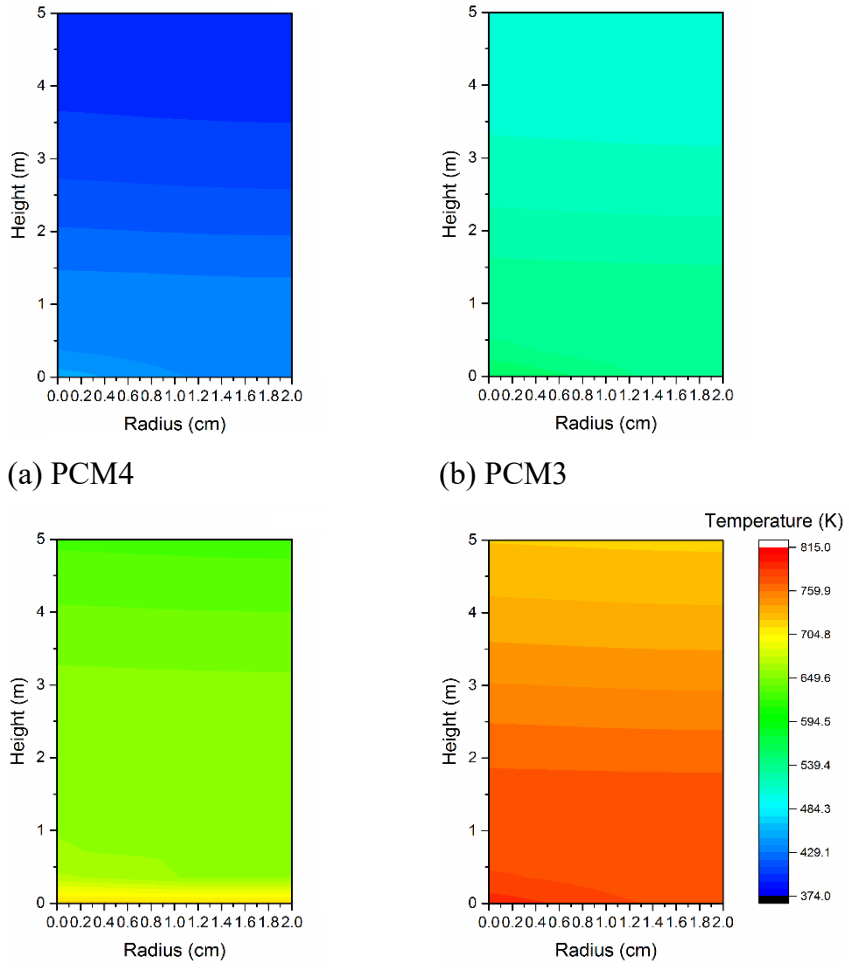

(a) PCM4 (b) PCM3

(c) PCM2 (d) PCM1

Figure 5.14: Temperature distribution of different PCM layers at the end of charging in the load-following operation.

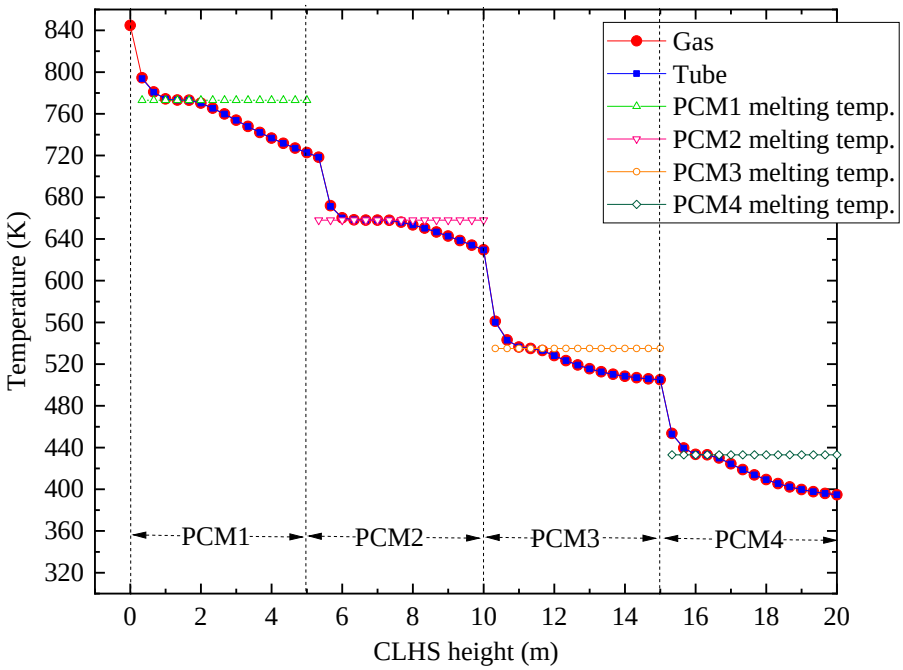

Figure 5.15: Gas and tube temperature after charging process.

Figure 5.14 shows the temperature distribution of different PCM layers at the end of charging in the load-following operation (time=2160s). Compared to the temperature distribution of different PCM layers in the start-up operation (Figure 5.10), the radial temperature difference of each PCM layer is significantly reduced. This is because the charging time is longer and the charging mass flow rate is smaller than that in the start-up operation. Thus, the thermal energy can be more fully transferred from inner side to outer side of the LHS.

Figure 5.15 shows the gas temperature and the inner tube temperature at the end of charging in the load-following operation (time=2160s). Compared to the gas and tube temperature in the start-up operation (Figure 5.11), the temperature difference of them becomes very small because the mass flow rate is much lower than the start-up operation, so the gas temperature could drop faster along the flow direction, see equation 5.3. It can be seen from Figure 5.15 that the gas temperature drops significantly from one PCM to the next PCM. This can be explained by the fact that the latent heat is much higher than sensible heat, so that the PCM temperature keeps at melting point for a long duration. The heat transfer rate relies on the temperature

difference between gas and PCM, the bigger the temperature difference, the more heat will be transferred to PCM and the faster gas temperature will drop.

5.4.2.2 CLHS Standby Process

After charging, the power demand returned to 420 MW, correspondingly the steam turbine output power returned to 135 MW. System load demand remained at 420 MW for 700 seconds. Therefore, the CLHS was on standby from 2160 seconds to 2800 seconds, i.e. neither charging nor discharging during this period. This CLHS is assumed to be an adiabatic system, so the heat transfer from storage system to surroundings is neglected. This study focuses on short term storage, while the heat loss from the store is significant which cannot be ignored, for the long term storage.

Figure 5.16 shows the temperature distribution of different PCM layers at the end of standby process (time=2800s). Although there is no heat transfer with external, the heat conduction still occurs inside the CLHS, thus resulting in a further thermal diffusion in each PCM layer.

The gas and tube temperature after CLHS standby duration is shown in Figure 5.17. The tube temperature difference of each layer becomes smaller compared with Figure 5.15 as the heat conduction is still happening and the heat continues to be transferred to the PCM from the tube. The temperature of part of PCM is equal to phase change temperature, at these area, the material could be liquid, solid or mixed.

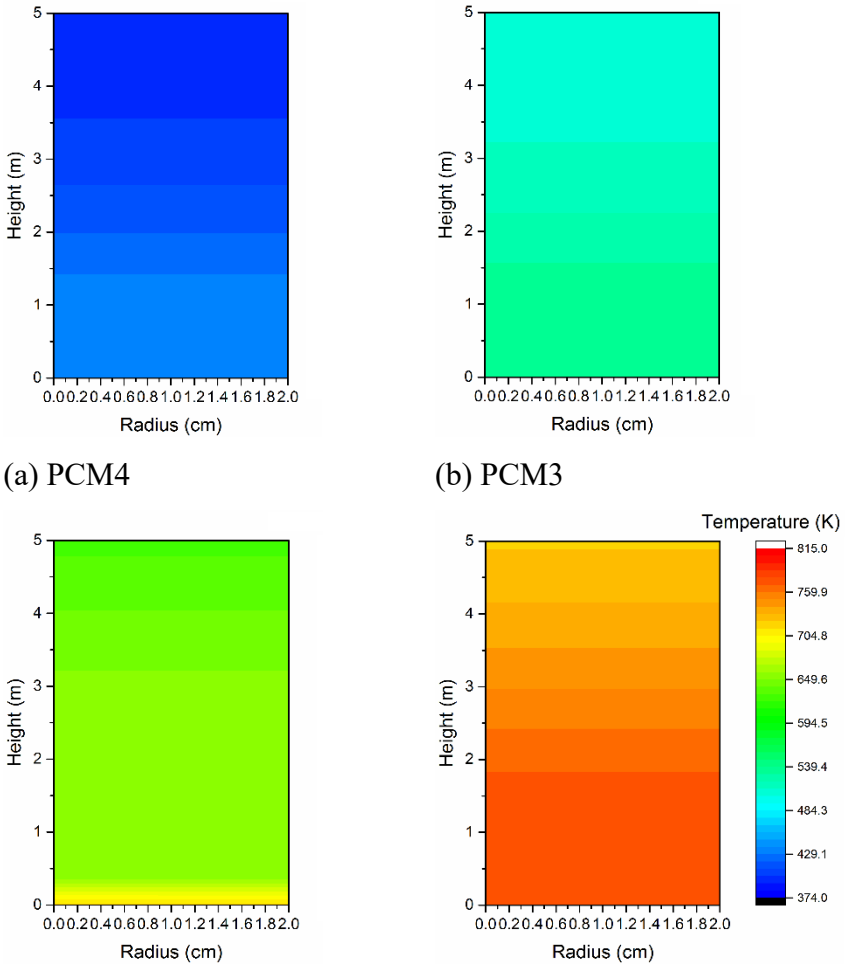

(a) PCM4 (b) PCM3

(c) PCM2 (d) PCM1

Figure 5.16: Temperature distribution of different PCM layers at the end of standby in the load-following operation.

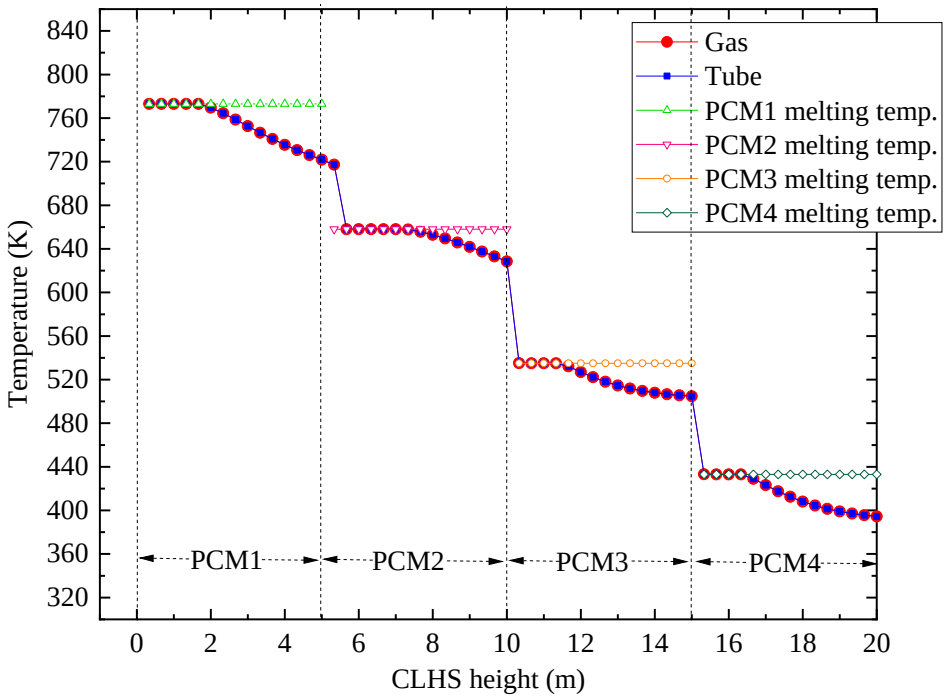

Figure 5.17: Gas and tube temperature after standby.

5.4.2.3 CLHS Discharging Process

At the 2800th second, the load demand increases from 420 MW to 428 MW, correspondingly the steam turbine output power is increased from 135 MW to 143 MW and the gas turbine section is still running at the rated condition. Therefore, additional 10 kg/s of superheated steam should be fed to IPTB that is produced by CLHS. Under discharging conditions, the extracted feed water flows from the top of the CLHS to its bottom, which is the direction along the ascending order of PCMs melting point.

Figure 5.18 shows the temperature distribution of different PCM layers at the end of discharging process in the load-following operation (time=4000s). Compared to the temperature distribution of different PCM layers at the end of standby in the load-following operation (Figure 5.16), the radial temperature is slowly reduced from the right end to the left end at the same height of each PCM layer. This proves

that some amount of heat has been transferred from the PCM layers to the feed water.

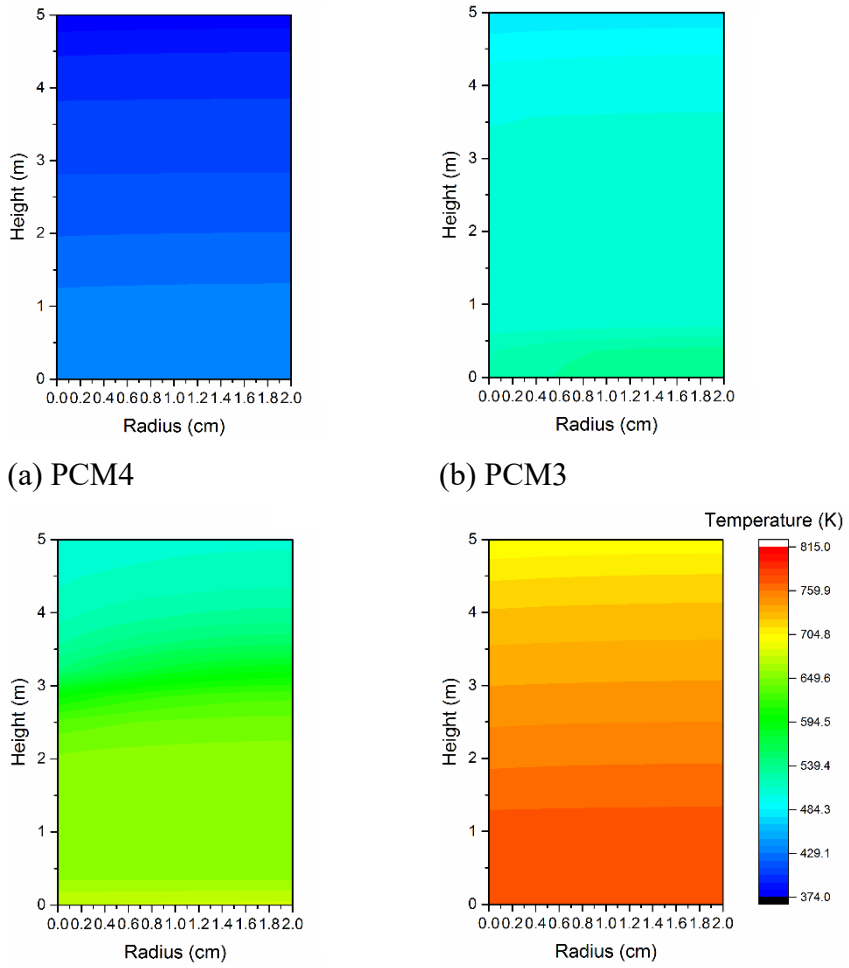

(a) PCM4 (b) PCM3

(c) PCM2 (d) PCM1

Figure 5.18: Temperature distribution of different PCM layers at the end of discharging in the load-following operation.

It can be seen from the simulation results that although the temperature change is small, the amount of stored or released heat is large. This is because the energy density of the latent heat is much higher than the sensible heat. The CLHS system with different melting temperatures can make the temperature difference between the working fluid and PCMs large enough to ensure efficient heat transfer for both charging and discharging processes for a long period of time.

In the proposed system, the water will flow through the same tube in CLHS which the exhaust gas was passed during the charging process. In the real manufacture, the generated steam must not be contaminated, if the proposed system cannot guarantee this, other types of heat exchanger should be considered, such as using two sets of heat transfer tubes in the PCM, using a heat transfer medium, etc.

5.4.2.4 Load Following Dynamics

Figure 5.19 shows the real-time output power of the steam turbines during load-following operation. The steam turbines can correctly respond to the load dynamics with the help of CLHS integration. Whenever the load changes, the steam turbines can respond to them within 6 minutes. The response time satisfies the Secondary Frequency Response requirements of generating units specified in the GB Grid Code [113].

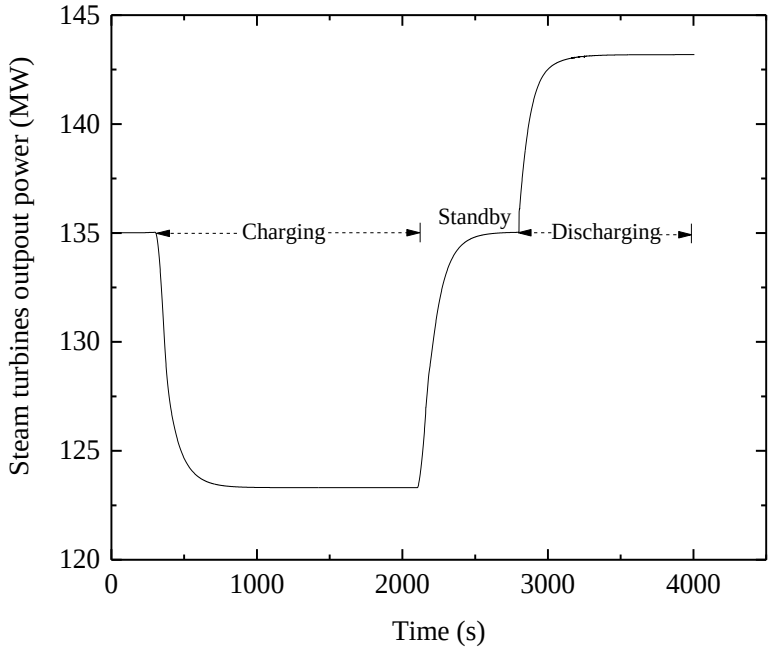

Figure 5.19: Real-time output power of the steam turbines during load-following operation.

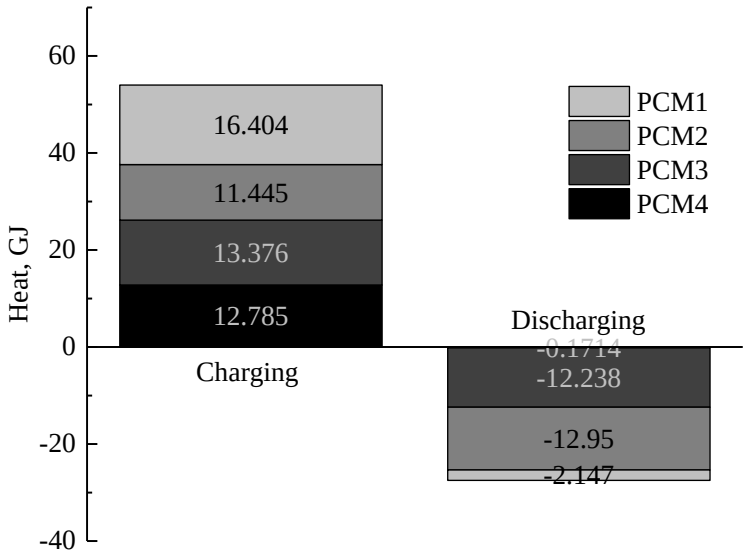

Figure 5.20: Amount of heat stored and released over charging and discharging during load-following operation.

Figure 5. 20 further reveals the amount of stored and released thermal energy over the charging and discharging periods during the load-following operation. According to the calculation, a total of 54 GJ heat is stored in the CLHS system in the 1860 seconds, and a total of 27.5 GJ heat is released to the feed water in the 1200 seconds. It can be seen that each PCM layer stores a relatively equal amount of heat during charging, but that is very different during discharging process. The discharged heat from PCM4 is very small (0.1714 GJ), therefore it is not visible from the figure. This is because heat transfer is mainly determined by the heat sink, which is water for discharging and PCM for charging. At the beginning, the initial temperature of each PCM layer is close to its own phase change temperature. During the charging process, and the phase change occurs gradually throughout the PCM layers, so heat is stored primarily through latent heat of phase change and the thermodynamic reversibility of the process is relatively greater. During the discharging process, the most of the heat is used to evaporate the feed water, however, the evaporation point of the water does not change much, which causes its evaporation to occur in only a few layers. This explanation can also be verified by the results shown in Figure 5.21 and Figure 5.22.

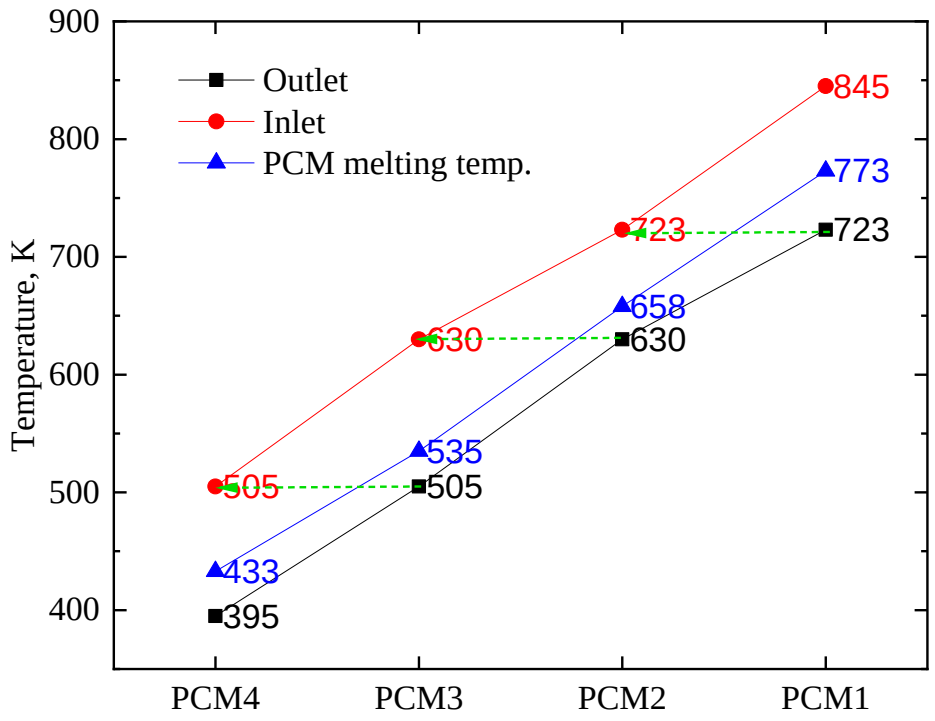

Figure 5.21: Inlet and outlet temperature at each PCM layer at the end of charging during load-following operation.

As can be seen, during the charging process, the temperature of the exhaust gas entering and exiting each PCM layer crosses its phase change temperature (Figure 5.21). However, during the discharging process, only the temperature of the water entering and exiting the PCM2 and PCM3 crosses its phase change temperature (Figure 5.22). Therefore, based on the different thermal properties of PCMs and water, it can be expected that there is an optimal thickness for each phase change layer to maximise the CLHS performance. The layers with the phase change temperature slightly higher than the water evaporation point should be thicker. On the other hand, the layers with the phase change temperature lower than the water evaporation point should be thinner, as well as the layer with the highest phase change temperature. The optimisation target is to use the least amount of PCM but satisfying the requirement of operation, such as the temperature of the produced steam.

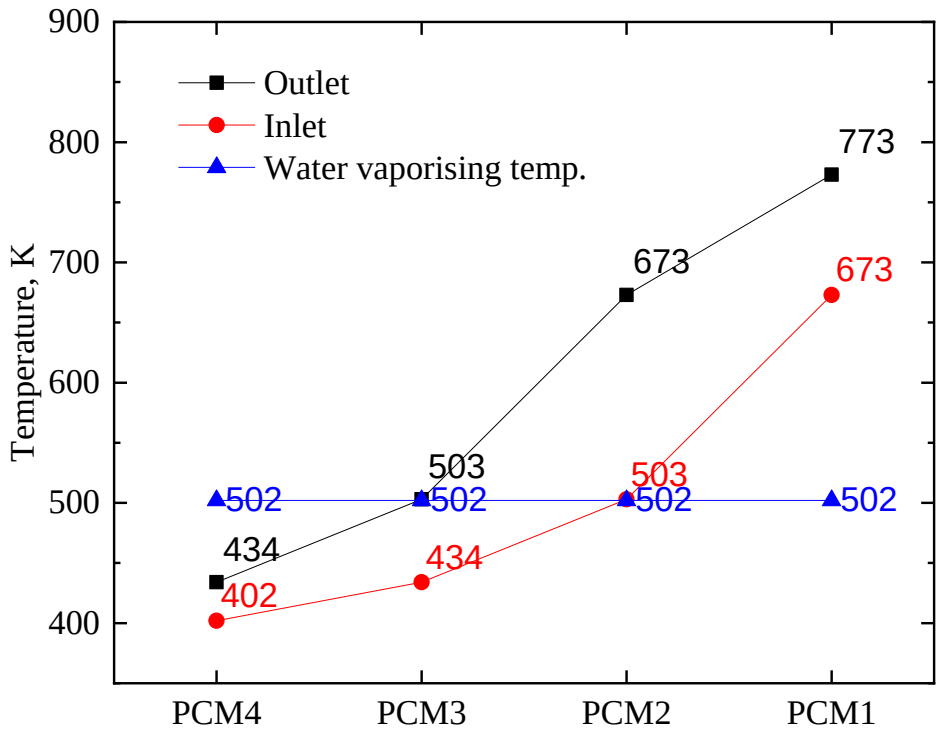

Figure 5.22: Water inlet and outlet temperature at each PCM layer at the end of discharging during load-following operation.

5.4.3 TES Integration Strategy during Plant Standstill for Faster Restart

In the future power grid, the CCGT power plant will experience more frequent shut-down and start-up. According to the initial temperature of the material, the start-up procedure of the CCGT power plant can be divided into: hot, warm and cold start depending on the initial temperature of the material, with standstill for up to 8 hours, 48 hours and 120 hours, respectively [73]. The start-up speed is limited by the thermal stress of the HRSG and steam turbines. The longer the standstill time, the longer start-up time is required unless there a heat preservation measure is adopted. Thus, keeping the HRSG warm is vital for the CCGT power plant to restart faster. In fact, the stored thermal energy can also be used to keep HRSG warm during plant standstill period. As shown in Figure 5.21, during the off-load period, ambient air is fed into the CLHS from top to bottom to produce hot air, which is then sent to

the HRSG to compensate the heat loss of the HRSG, thereby keeping the HRSG in a hot or warm state ready for faster start-up. The potential approach is to keep the HRSG warm using heat from the CLHS instead of maintaining the natural circulation, so the gas turbine and steam turbines can be shut down. This approach does not change the inherent structure of the HRSG and the working fluid, there should be no major technical barrier in the implementation process. In addition, the air flow rate fed into the CLHS is determined by the current temperature drop in the CLHS, and this process can be controlled by a feedback loop. The detailed standstill simulation is beyond the scope of this thesis, which could be considered as a future research direction.

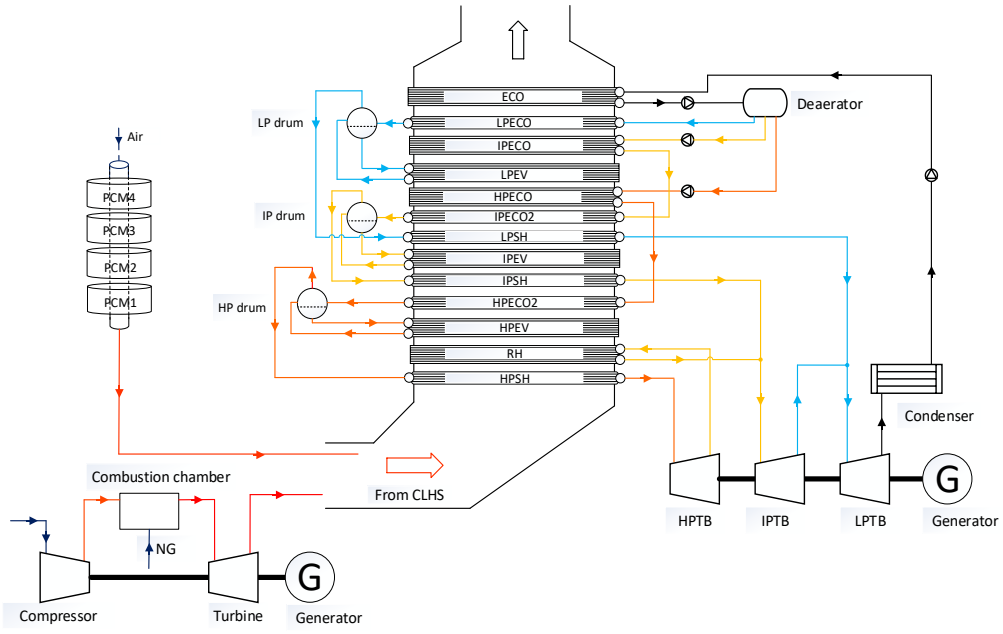

Figure 5.23: CLHS integration strategy for discharging during plant standstill.

5.5 Summary

This chapter describes the dynamic modelling and simulation study for CLHS integration into a 420 MW CCGT power plant for flexible plant operation. The integration strategies during start-up, load-following and standstill operations are proposed and studied. From this study, it is evidenced that:

1. The dynamic simulation results showed that the strategies for CLHS integration with CCGT power plant are technically feasible. With the CLHS integration, the steam turbine section could achieve flexible operation but gas turbine section still operates at rated condition.

2. In the plant start-up processes, 75% of the gas turbine exhaust gas could pass through CLHS before discharged into the atmosphere, and then the waste heat can be captured by CLHS.

3. During the load-following operation, the output power of the CCGT power plant can be reduced by extracting exhaust gas from the gas turbine, the extracted exhaust gas is used to charge the CLHS. The minimum steam turbine power is 66 MW when 363 kg/s exhaust gas by pass to the CLHS for thermal storage. The stored heat can be discharged to produce high-temperature and high-pressure steam for the steam turbine to increase the output power. The maximum steam turbine output power increases to 143 MW. Meanwhile, the gas turbine section is still running at the rated load condition.

4. The HRSG start-up speed is determined by which initial condition is hot, warm or cold. In the plant standstill duration, stored heat can be used to produce hot gas to maintain the HRSG under warm condition to reduce restart-up time.

Chapter 6-Study of CCGT Power Plant Integration with A-CAES

6.1 Introduction

Figure 1.4 describes the general power generation processes of thermal power plants; it shows that the energy undergoes transformation from thermal energy to mechanical energy before being transformed to electrical energy. As introduced in Chapter 3 and Chapter 5, it is a feasible way to integrate TES into thermal power plant to achieve flexible operation. This chapter presents the feasibility study of a CCGT power plant integration with A-CAES for plant flexible operation.

The essential components of a CAES power plant includes pressurised air cavern or tank, compressor, gas turbine and generator, some of them may also have a combustion chamber or TES. Coincidentally, the CCGT power plant contains all of these components except air cavern, which may imply that CCGT power plant integrates with CAES possible.

This chapter starts with a review of CAES systems. The dynamic modelling of a pressurised air cavern, a CLHS and a packed bed sensible heat storage (SHS) are formulated. The latent heat storage and sensible heat storage are combined for formulating thermal storage and this design contributes to the performance of the thermal storage system. Modelling of the hybrid system with CCGT and A-CAES is also proposed in this chapter, and the hybrid system is optimised by a Genetic Algorithm. Then the improvement of operational flexibility of the CCGT power plant is presented in terms of the operating range and response speed. Finally, a case study of CCGT power plant integration with A-CAES to support wind power generation is analysed.

6.2 Review of CAES Technology

CAES is one of the energy storage technologies that could make contributions to improve the flexibility of power generation. This section presents a review of CAES technologies. There are at present two commercial CAES power plants, Huntorf plant and McIntosh plant in operation. The Huntorf plant was built in 1978 in Germany with 290 MW capacity, and the McIntosh plant was built in 1991 in the USA with 110 MW capacity [114].

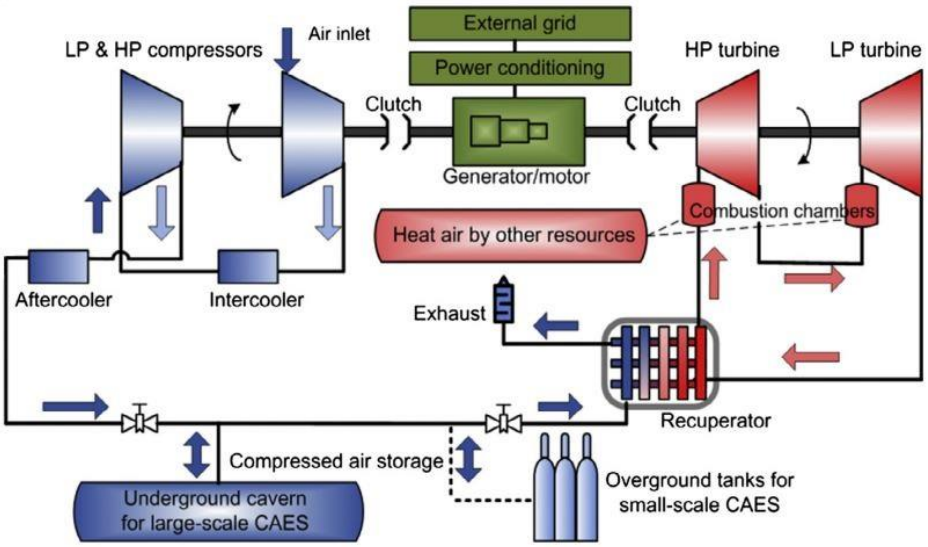

Figure 6.1: Schematic diagram of a CAES plant [7].

The schematic of a CAES plant is plotted in Figure 6.1. Low-cost electricity is used to spin a motor that drives a compressor to produce compressed air for storage in an underground cavern or overground tanks. On the other hand, during periods of high power demand, the stored compressed air is released and heated, and then expands through an expander that drives the generator to produce electricity.

The means of storage for compressed air, such as a cavern or tank, affect the overall performance of a CAES plant. Dynamic modelling of storage units has been extensively studied to understand the dynamic behaviour of the compressed air pressure and temperature in storage units [115, 116]. The storage capacity is an important factor that determines the power capacity for a designed CAES plant. A

larger storage system means more energy can be stored in the form of compressed air. A method to estimate the exergy storage capacity for a known storage volume and the storage volume required for a specific exergy storage capacity was proposed in [114].

Some researchers have focused on CAES plant design and modelling. A dynamic simulation tool for A-CAES plant modelling and transient control was demonstrated in [117]. He et al. [98] developed a detailed modelling framework for A-CAES modelling to analyse the system transient behaviours. A constant-pressure CAES combined with pumped hydro storage was also proposed to overcome the drop of cavern pressure during discharging operation [118]. Recently, a pilot scale A-CAES plant with SHS was built in a mountain tunnel for which the estimated round-trip efficiency achieves around 63-74% [119].

6.3 Dynamic Modelling of the Pressurised Air Cavern and SHS

6.3.1 Pressurised Air Cavern Model

In this study, a fixed volume tank is used to store compressed air. A dynamic model of the compressed air tank is employed to simulate the transient behaviour of the temperature and pressure of the air within the air cavern (see Appendix).

The schematic of a control volume air cavern is shown in Figure 6.2.

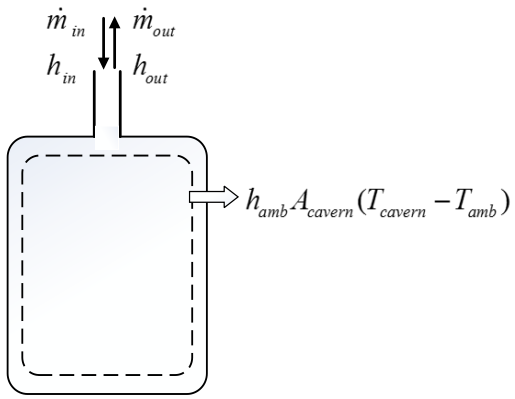

Figure 6.2: Schematic of control volume enclosing the storage bed.

Based on the first law of thermodynamics, the energy balance equation for the control volume can be written as [116, 120]:

$$\frac{d(Mu)}{dt} = \dot{m}_{in} h_{in} - \dot{m}_{out} h_{out} - h_{amb} A_{cavern} (T_{cavern} - T_{amb}), \qquad (6.1)$$

where, M is the mass of air in the cavern, u is the specific internal energy, $\dot{m}_{in}$ is the incoming mass flow rate, $\dot{m}_{out}$ is the outgoing mass flow rate, h_{in} is the specific enthalpy of incoming air, h_{out} is the specific enthalpy of outgoing air, h_{amb} is the heat transfer coefficient between cavern air and cavern wall, A_{cavern} is the area between the air and cavern wall, T_{cavern} is the cavern air temperature, T_{amb} is the cavern wall temperature. The left side of this equation is the change rate of the cavern air internal energy, the first two terms on the right side of the equation represents the rate of incoming and outgoing air enthalpy, and the last term of this equation is the heat transfer from cavern air to cavern surroundings.

For the ideal gas:

$$u = h - \frac{P}{\rho}, \qquad (6.2)$$

$$dh = c_p dT, \qquad (6.3)$$

where, P is the pressure, ρ is the density, c_ρ is the specific heat capacity.

Substituting Equations (6.2) in Equation (6.1) leads to:

$$\frac{dMh_{cavern}}{dt} - \frac{dMP/\rho}{dt} = \dot{m}_{in} h_{in} - \dot{m}_{out} h_{out} - h_{amb} A_{cavern} (T_{cavern} - T_{amb}), \qquad (6.4)$$

then,

$$\frac{dMh_{cavern}}{dt} - \frac{dVP}{dt} = \dot{m}_{in} h_{in} - \dot{m}_{out} h_{out} - h_{amb} A_{cavern} (T_{cavern} - T_{amb}), \qquad (6.5)$$

as V is a constant, yielding:

$$M\frac{dh_{cavern}}{dt}+h_{cavern}\frac{dM}{dt}-V\frac{dP}{dt}=\dot{m}_{in}h_{in}-\dot{m}_{out}h_{out}-h_{amb}A_{cavern}(T_{cavern}-T_{amb})\,. \quad (6.6)$$

Therefore, for the charging process ($\dot{m}_{out}$ is 0):

$$\rho c_p\frac{dT_{cavern}}{dt}+\frac{\dot{m}_{in}}{V}c_p(T_{cavern}-T_{in})-\frac{dP}{dt}+\frac{h_{amb}A_{cavern}}{V}(T_{cavern}-T_{amb})=0\,. \quad (6.7)$$

For the discharging process ($\dot{m}_{in}$ is 0):

$$\rho c_p\frac{dT_{cavern}}{dt}+\frac{\dot{m}_{out}}{V}c_p(T_{out}-T_{cavern})-\frac{dP}{dt}+\frac{h_{amb}A_{cavern}}{V}(T_{cavern}-T_{amb})=0\,. \quad (6.8)$$

The ideal gas state equation is given by:

$$PV=MRT\,, \quad (6.9)$$

where, R is the gas constant.

Based on the energy balance equation and ideal gas state equation, the cavern air temperature and pressure can be calculated. The cavern parameters used in this study are listed in Table 6.1, and the cavern size is same as the Huntorf plant [115].

Table 6.1: Cavern parameters used in the calculation [115].

Parameters	Value, Units
Cavern radius	20 m
Cavern volume	141,000 m^3
Cavern surface area	25,000 m^2
Heat transfer coefficient	30 W m^{-2} K^{-1}

The air tank model is validated by the test data from the Huntorf Plant. The initial conditions are listed in Table 6.2. The air flow rate of the cavern is described in Figure 6.3, the negative value means discharging mass flow rate, and the positive value means charging mass flow rate.

Table 6.2: Initial condition [115].

Parameters	Value, Units
Initial cavern air Temperature	40 ℃
Rock temperature	40 ℃
Initial air pressure in cavern	5.9 MPa

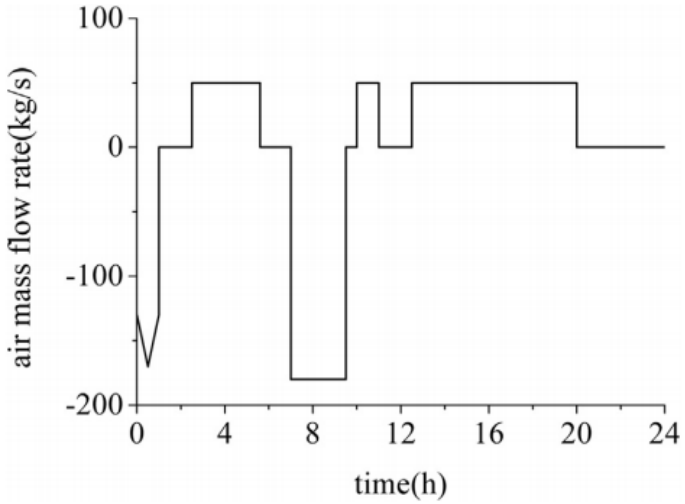

Figure 6.3: Air mass flow rate [115].

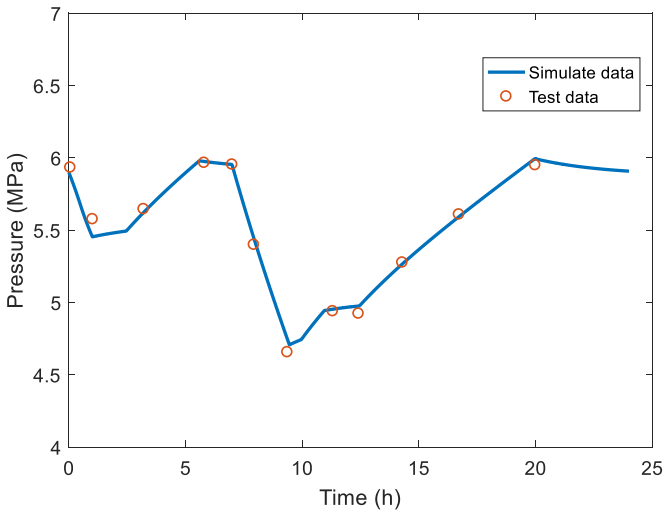

Figure 6.4: Air pressure variation in the cavern of Huntorf plant during the test.

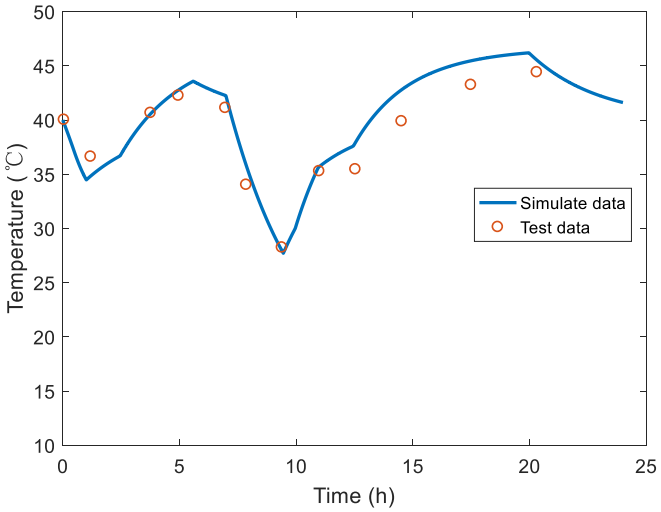

Figure 6.5: Air temperature variation in the cavern of Huntorf plant during the test.

The air pressure variation in the cavern is shown in Figure 6.4, and the air temperature variation is shown in Figure 6.5. The red circle is the test data from [115], and the blue line is the simulation results. The calculated pressure is in excellent agreement with test data, whereas the calculated temperature exhibits slight deviations but still agrees well with the test data. Although the simulation data is slightly different to the test data of the trial operation of the Huntorf plant, the simulated temperature successfully captures the trend of test data. Besides, the simulated results are close to the similar models presented in [114] and [115]. The main difference of the air cavern models presented in [114-116, 121] is the way to calculate the heat transfer between cavern air and cavern wall. The heat transfer coefficient can be assumed as a constant or calculated by the complex heat convection and head conduction equations. Either of them could calculate the cavern air temperature and pressure which are in sound agreement with the test date.

6.3.2 Cascaded Latent Heat Storage Model

This section presents the model for the designed CLHS. The structure of the CLHS is shown in Figure 6.6, and the thermophysical properties of the PCMs are listed in Table 6.3. The details of the mathematical modelling can be found in Section 5.3.

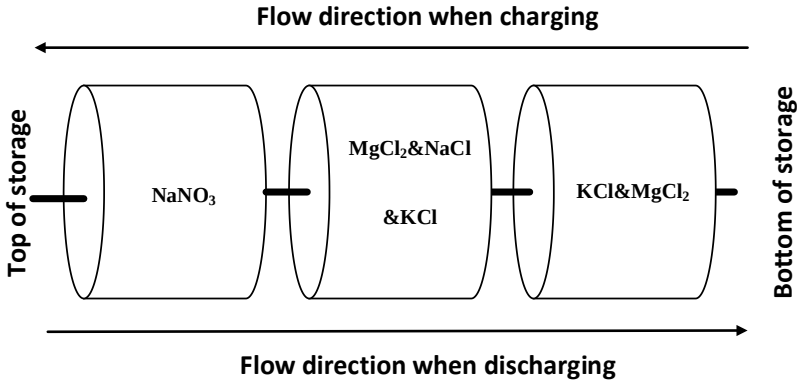

Figure 6.6: Designed CLHS system with 3 PCMs.

Table 6.3: Thermophysical properties of salts compositions extracted from[68, 109].

Material	Composition, wt%	Melting temp., K	Latent heat, J/g	Capacity, J/(g·K)	Density, g/cm^3	Conductivity, W/mK
PCM1	KCl(61)-39$MgCl_2$	708	351	0.96	2.11	0.81
PCM2	$MgCl_2$(63)-22.3NaCl-14KCl	658	461	0.96	2.25	0.95
PCM3	$NaNO_3$	580	172	1.68	2.26	0.5

The physical properties of PCM in each layer are listed in Table 6.3. The dimensions of this CLHS model is same as the one in Section 5.3 except the height which is 9 m and 3 m for each PCM layer, as shown in Figure 6.7.

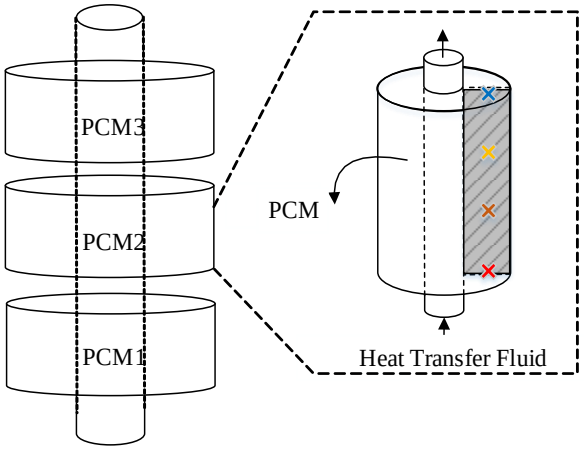

Figure 6.7: Structure of a single CLHS set.

6.3.3 Packed Bed Sensible Heat Storage Model

This section presents the mathematical model of a packed bed sensible (PBS) heat storage model. The main advantages of packed bed (PB) of rocks for TES are [122]: i) rock is an abundant and economical storage material; (ii) rock can be applied in a wide temperature range; (iii) rock is a safe material and without any degradation or chemical instability.

PB thermal storage systems are considered as an attractive storage solution for power plant applications. For concentrated solar power (CSP) plants using air as heat transfer fluid, a PB of rocks was used to provide a solution to overcome the intermittency of solar radiation [94, 123]. The weakness of the packed bed of rock systems is the drop of outlet temperature during the discharging period. Zanganeh et al. [124] proposed a concept of combined sensible and latent heat storage to address the disadvantage of rocks. The PB thermal storage can also be used to improve the cycle efficiency of the compressed air energy storage system [98].

Based on previous studies, a packed bed sensible heat storage model is designed, as shown in Figure 6.8(a), which has a diameter of 10 m, and a height of 10 m. The packed bed column is divided into 50 elements, each containing steatite

(magnesium silicate rock) surrounded by working fluid. The cross-section of one layer is shown in Figure 6.8 (b).

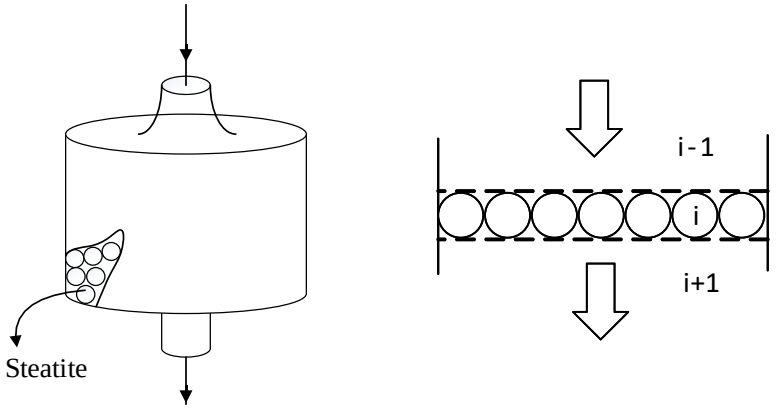

(a) (b)

Figure 6.8: SHS system: (a) Layout of the packed bed SHS; (b) Cross section of a layer.

A one-dimensional two-phase transient model is formulated, which considers heat convection and heat conduction. In this model some assumptions are made: uniformly packed bed of constant solid heat capacity, temperature gradient in the radial direction is neglected, uniform temperature particles, as justified by $Bi \le 1$, radiation heat transfer is neglected, and heat conduction in fluid phase is neglected. Based on the energy balance equation, the governing unsteady energy conservation equations are shown as:

$$\frac{dMu}{dt} = \dot{m}_{in} h_{in} - \dot{m}_{out} h_{out} + \dot{Q} - W \,, \tag{6.10}$$

where, $\dot{Q}$ is the heat transfer rate, and W is the work output.

For the fluid [124]:

$$\varepsilon \rho_{f,i} c_{p,f,i} \frac{dT_{f,i}}{dt} = \frac{1}{V_i}[(\rho_f v h_f \varepsilon A)_{i-1} - (\rho_f v h_f \varepsilon A)_i] - h_{v,i}(T_{f,i} - T_{s,i}) \,, \tag{6.11}$$

where, ε is the void fraction, ρ_f is the fluid density, v is the interstitial speed, h is the enthalpy, A is the surface area, T is the temperature, h_v is the volumetric

convective heat transfer coefficient, the subscript f is the fluid side s is the solid side, and the subscript i is the number of elements.

The left side of the above equation is the fluid internal energy change, the first term in the right side is the convection of energy by flow, and the last term is the convection from fluid to solid.

For the solid [94, 125]:

$$(1-\varepsilon)\rho_s c_{p,s}\frac{dT_{s,i}}{dt} = h_{v,i}(T_{f,i} - T_{s,i}) + (1-\varepsilon)k_s\frac{d^2T_{s,i}}{dx^2}, \qquad (6.12)$$

where, k_s is the thermal conductivity.

The left side of the above equation is the solid internal energy, the first term in the right side is the convection from fluid to solid, and the last term is the thermal dispersion by heat conduction.

The volumetric convective heat transfer between fluid and solid is calculated by [122]:

$$h_v = 700(G/d)^{0.76}, \qquad (6.13)$$

where, G is the mass flow rate per unit cross section, and d is the steatite diameter.

The operational parameters of the packed bed sensible heat storage are presented in Table 6.4.

Table 6.4: Operation data for packed bed sensible heat storage [94].

Parameters	Value
$c_{p,s}$	$1068\ J/(kg\cdot k)$
d	$0.02\ m$
k_s	$2.5\ W/(m\cdot K)$
ε	0.4
ρ_s	$2680\ kg/m^3$

6.4 A-CAES Integration Strategy and Optimisation

This section presents the designed structure and optimisation strategy of the hybrid system. In CCGT power plants, the air flows into a compressor to compress the air to the designed pressure, and then combusts with natural gas in the combustion chamber. The combustion gas goes into the gas turbine where it is expanded and driving the generator to produce electricity. The hot exhaust gas from gas turbine contains a lot of energy, this heat is used by HRSG to produce steam which drives stream turbine for generating additional electricity. Therefore, the total output power of the CCGT power plant (P_{tot}) is calculated by:

$$P_{tot} = P_{gt} - P_c + P_{st}\,, \tag{6.14}$$

where, P_{gt} is the gas turbine output power, P_c is the compressor consumed power and P_{st} is the steam turbine output power.

The power of gas turbine, compressor and steam turbine is in direct proportion to the mass flow rate. In the normal operation, the mass flow rates of gas turbine and steam turbine relies on the compressor mass flow rate. This means that the change of compressor mass flow rate is the only method to control the plant power output. However, the rate of change of the mass flow is limited, which limits the power ramp rate. The compressor has to operate between the choke line and surge line, which also determines the operation rage of the CCGT power plant. The strategy proposed in this chapter is to control both of mass flow rates through the gas turbine and compressor through A-CAES integration to achieve plant flexible operation. The integration strategies for energy storage charging and discharging processes are presented in Figure 6.9 and Figure 6.10, respectively.

In the charging process, a portion of compressed air is extracted from the compressor outlet, which then passes through the CLHS and SHS where the thermal energy is stored. The temperature of compressed air decreases to around 320 K from 700 K, before the compressed air is stored in the storage cavern. In the discharge process, firstly, the compressed air is released and supplied to a booster to raise the

pressure, because the pressure of compressed air drops during the storage. Then the compressed air flows into SHS and CLHS to increase the temperature in the reverse direction of the charging process. Finally, the compressed air from the air cavern mixes with compressed air from the compressor and flows into the combustion chamber.

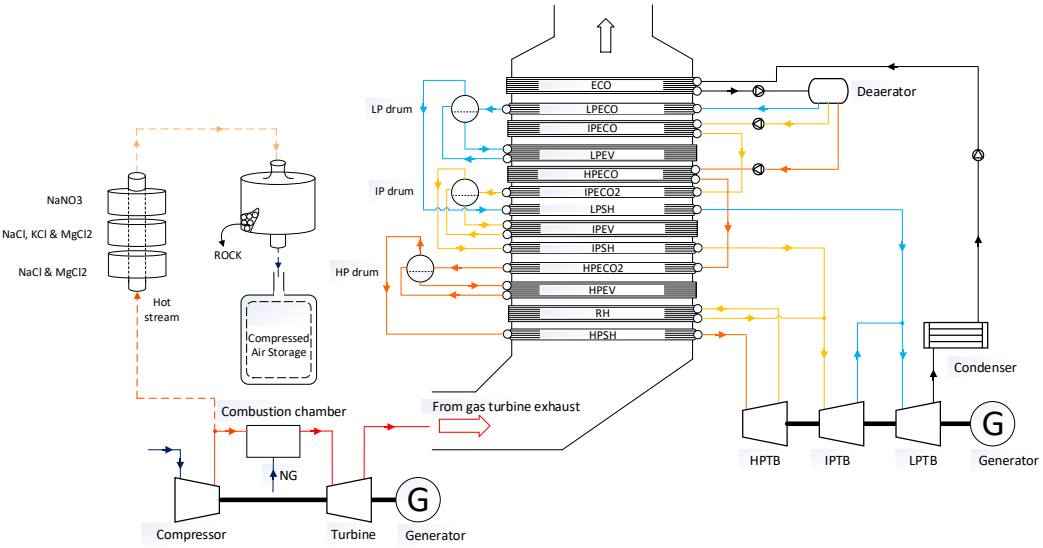

Figure 6.9: Schematic flow diagram of charging process.

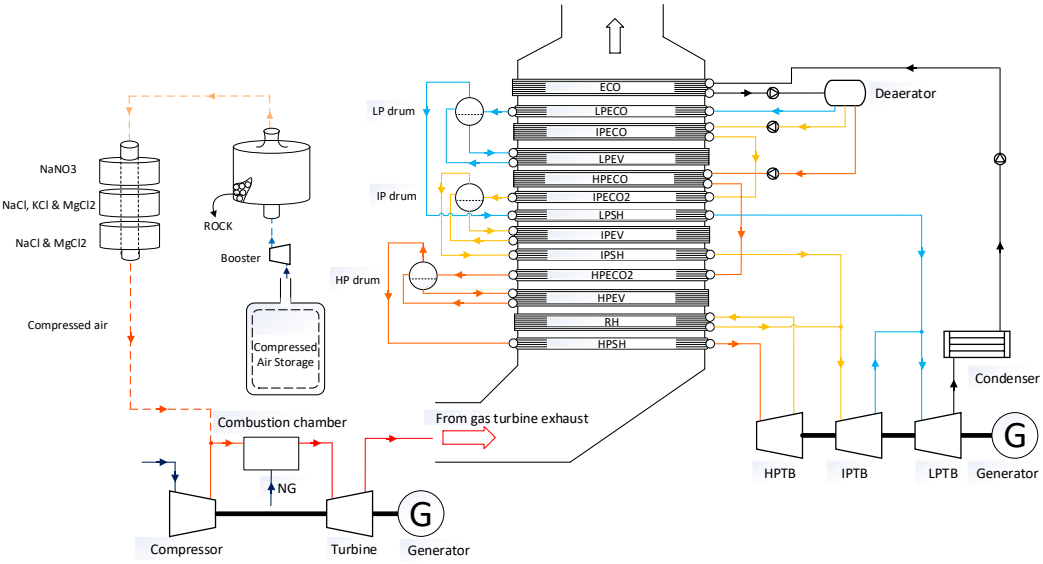

Figure 6.10: Schematic flow diagram of discharging process.

In the designed system, the TES system contains a CLHS module and a packed bed SHS module. The advantages of such a system are:

1. CLHS system can store thermal energy at a higher density based on the latent heat of the material with a small volume requirement.
2. The exergy efficiency of the storage process can be significantly improved using multiple PCMs than single PCM.
3. CLHS system can provide excellent heat transfer rate between PCM and the working fluid.
4. Compared with PCM, the packed bed SHS can operate in a wide temperature range, and expects to have a significantly lower fabrication costs [94].
5. PBS can reduce the compressed air temperature close to the environment temperature during the charging process, and recover the compressed air temperature during the discharging process.

The designed hybrid system generates electricity, thermal energy and mechanical energy at the same time. Therefore, it is a huge challenge to achieve optimal operation of the whole system. In a CHP power plant, the ratio between the losses of power caused by increase in heat generation is called the power loss coefficient, and it is calculated by [126, 127]:

$$\beta = -\frac{\Delta e}{\Delta q} > 0 \,, \tag{6.15}$$

where, $\Delta e = e_{\max} - e$ is the power reduction due to heat generation increase, $\Delta q = q_{\min} - q$ is the increased heat generation. It is important to note that the input fuel is a constant value, under this assumption, the output power reduces to e from $e_{\max}$, and the heat generation increases to q from $q_{\min}$.

Based on this idea, an optimisation method is proposed for this hybrid system of CCGT with A-CAES. The total output power of the CCGT power plant is calculated by Equation 6.14. Therefore, many different combinations of gas turbine power, compressor power, and steam turbine power will meet one particular load demand. In order to find the best value for the mass flow rate of the compressor and gas turbine, the following ratio is formulated to represent the fuel changes against

the compressed air mass flow changes, which must be positive from the practical operation restriction:

$$\alpha = \frac{fuel - fuel_n}{\Delta m} = \frac{\Delta fuel}{\Delta m} \geq 0\,, \tag{6.16}$$

where, α is the ratio between the change of fuel supply ($\Delta fuel$) and the mass flow rate of compressed air for charging (positive) or discharging (negative) processes (Δm), $fuel_n$ is the fuel mass flow rate while the conventional operation strategy applies (without A-CAES integration), and $fuel$ represents the fuel input while the optimised operation strategy is adopted (with A-CAES integration).

For the A-CAES charging process, the optimisation target is to find the minimum value of α, which represents the fuel consumption for the per unit compressed air generation. For the discharge period, on the contrary, the optimisation target is to find the maximum value of α, which is the fuel saving for the per unit compressed air consumption. This optimisation method deal with the hybrid system optimised point for difference load conditions. It should be point out that the time delay of stores and the electricity price would be considered during optimisation, in the electricity market.

The optimisation results are searched by using Genetic Algorithms; the flowchart of the optimisation algorithm is shown in Figure 6.11. Before running the optimisation algorithm, a target output power of the power plant is initialised. Based on the target power, a group of gas turbine power is generated, after that, the steam turbine output power and compressor required power is calculated. According to the operation data of the CCGT power plant, the fuel supply, gas turbine, compressor and air tank mass flow rate are found. There are two conditions used to determine when to stop. The first condition is that the number of iterations reaches the maximum value which is 100. The second condition is that the average relative change in the best fitness function value over Stall generations is less than or equal to Function tolerance which is 10^{-6}. Once one of termination conditions is reached, the current fuel supply, gas turbine and compressor mass flow rates will be output;

otherwise, the loop will be repeated to search the optimised results. At each generation step, a portion of the current solutions is selected to generate the next generation of solutions through a combination of genetic operators: crossover and mutation.

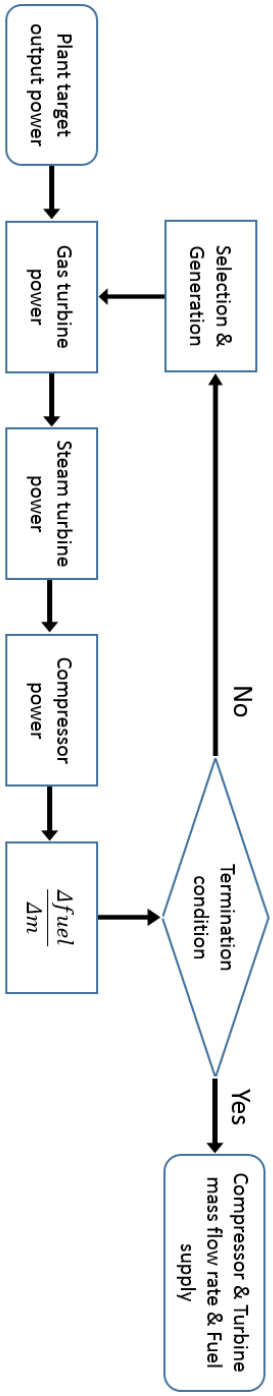

Figure 6.11: Flowchart of the optimization algorithm.

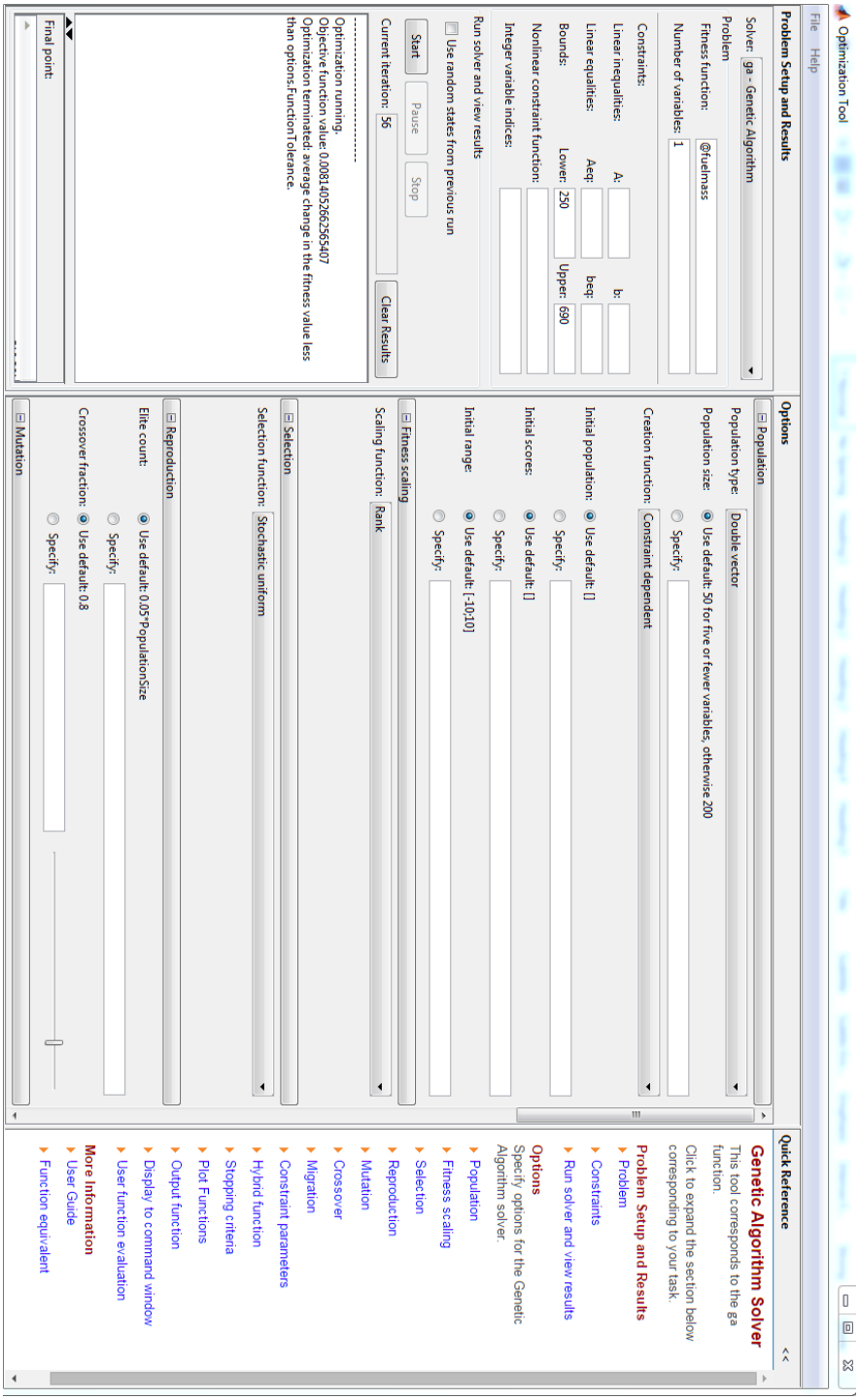

Figure 6. 12: Optimisation toolbox.

The Matlab optimisation toolbox is used to conduct optimisation calculation, as shown in Figure 6.12. The function “fuelmass” is used to calculate the ratio α, and the Genetic Algorithm toolbox is used to search the minimum value of α.

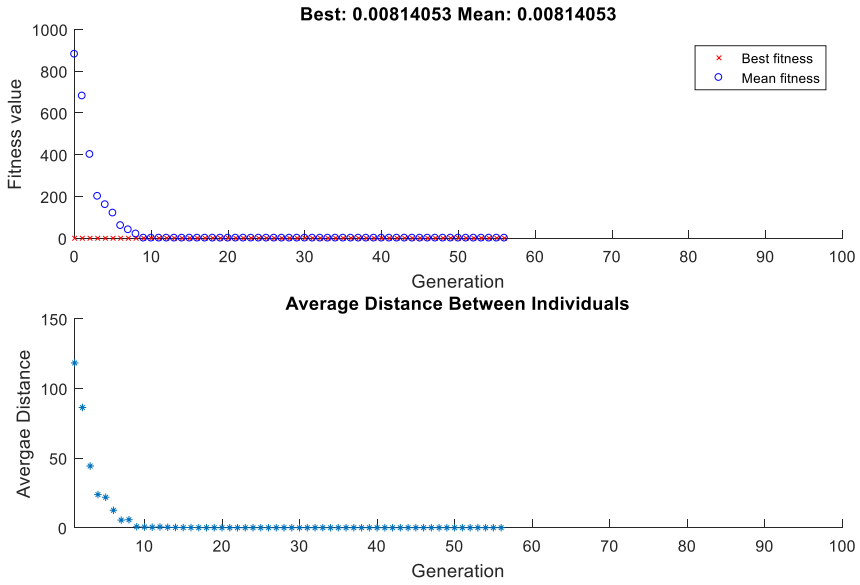

Figure 6.13: Optimization results when load is 350 MW.

Table 6.5: Optimisation results for 350 MW load demand.

Parameters	Value (kg/s)
$fuel$	12.703
$fuel_n$	12.4458
Δm (charging)	31.5851
Compressor mass flow rate	627.0006
Gas turbine mass flow rate	608.1185

An example of the optimisation process is given and the target power is set to be 350 MW. It can be seen from Figure 6.13 that the average difference between individuals is almost zero and the best fitness value is close to the optimised value, after ten times iteration. After 56 times iterations, the termination condition is reached, and the minimum value of α is 0.00814. The optimized results are listed in Table 6.5 when the load demand is 350 MW.

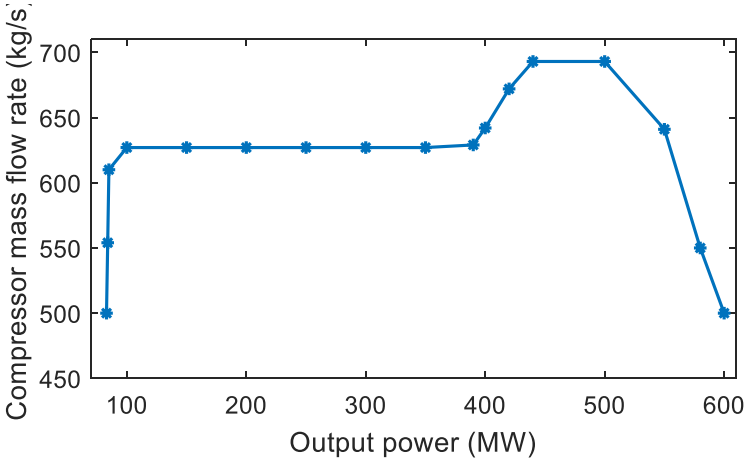

Figure 6.14: Optimized compressor mass flow rate.

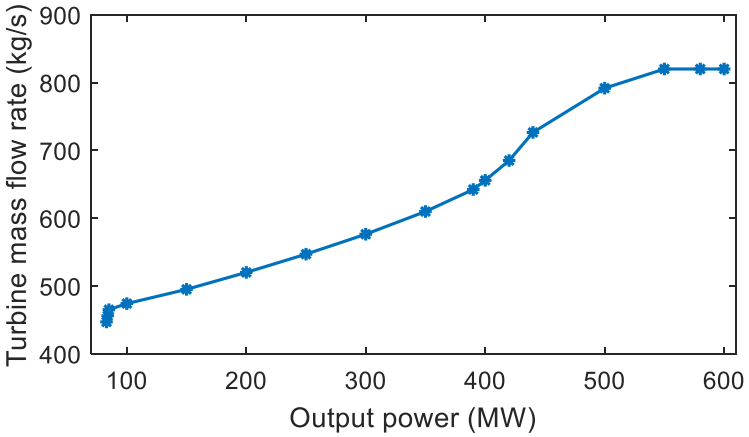

Figure 6.15: Optimized gas turbine mass flow rate.

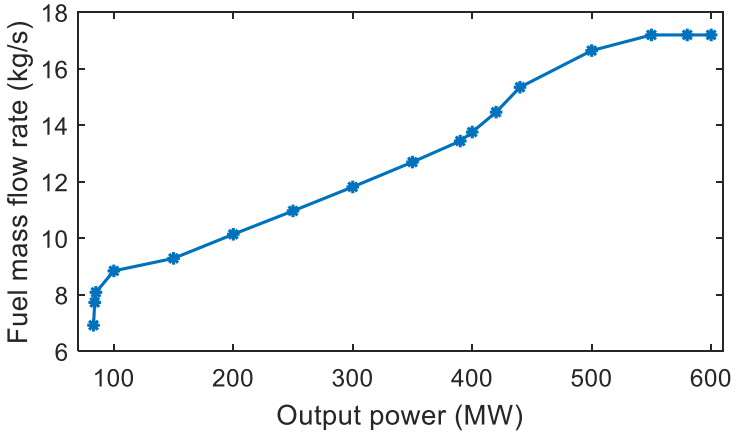

Figure 6.16: Optimized fuel supply.

Repeating the above procedures, the optimal solution for the mass flow rates of the compressor, gas turbine, and fuel supply can be found. The optimised compressor mass flow rate for various load demands is shown in Figure 6.14, the optimised gas turbine mass flow rate is presented in Figure 6.15, and the optimised fuel supply is illustrated in Figure 6.16. It can be seen from the optimised results that the compressor and turbine are tend to operate at high efficiency range. The detailed efficiency curve and formula can be found from Section 4.3.1. As shown in Figure 6.14, the compressor minimum mass flow rate is 500 kg/s and the maximum mass flow rate is 693 kg/s. Since the polytropic efficiency of the compressor is highest when the mass flow rate is 627 kg/s, the optimised compressor mass flow rate is kept at this point for various load conditions. It can be seen from Figure 6.15 that the turbine minimum mass flow rate is 447 kg/s and the maximum mass flow rate is 820 kg/s. The compressor efficiency starts to decline when the mass flow rate is under the 627 kg/s. If the load demand is less than 390 MW, the system is in charging process; if the load demand is between 390 MW and 430 MW, the system is neither charging nor discharging; if the load demand is higher than 430 MW, the system is in discharging process.

In the original operation (without A-CAES), the mass flow rate of the compressor and turbine decreases with the drop of plant output power, which leads to the reduction of the compressor and turbine efficiency. Therefore, with the A-CAES integration, the mass flow rate of the compressor keeps at 627 kg/s when the load demand is between 100 MW and 390 MW. Meanwhile, the mass flow rate of the turbine is higher than the original operation, which brings higher efficiency.

The minimum output power is reached when the compressor operates at the surge point (minimum mass flow rate), and the power generated by the gas turbine is just offset by the required power for compression. Meanwhile, part of the compressed air is shunted to the storage cavern for energy storage and all of the electrical power is generated by the steam turbines. The maximum output power is generated when the compressor consumes the minimum amount of power and the gas turbine generates the maximum amount of power. In this situation, the compressor must

operate at the surge point, and the mass flow rate of the gas turbine must be the maximum value.

6.5 Improvement of Operation Flexibility

This section presents the improvement of the operation flexibility of the CCGT power plant with A-CAES integration. The improvement of operation flexibility is discussed in terms of operating range and ramping rate.

Considering the limitation of compressor and gas turbine mass flow rate, the prototype of the CCGT power plant could work at the range of 200-430 MW. With the A-CAES integration, the hybrid power plant expects to operate in the wider range, from 83 MW to 600 MW, as shown in Figure 6.17.

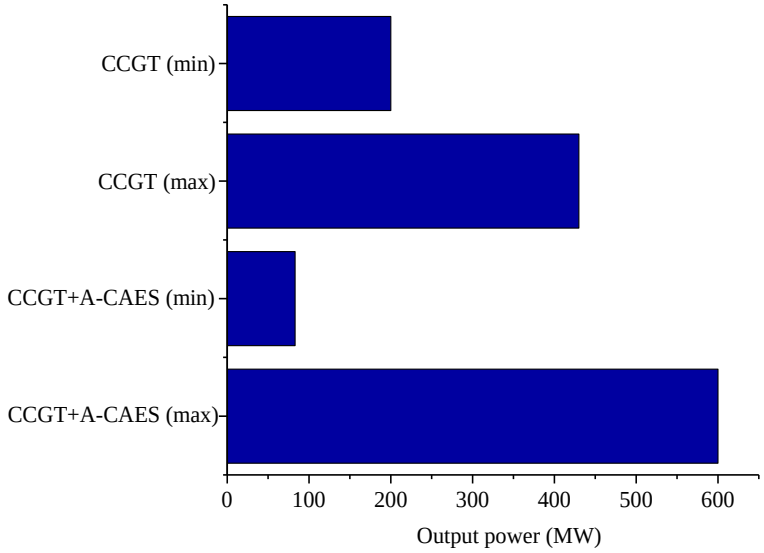

Figure 6.17: CCGT vs CCGT & A-CAES power output.

The dynamic performance of the CCGT power plant with and without A-CAES integration is studied. This subsection can only compare A-CAES charging process with CCGT power plant normal operation, because of the A-CAES discharging process beyond the normal operation rage of the CCGT power plant. The load demand is shown in Figure 6.18, where the initial load demand is 300 MW, and then at 150s the load demand increases to 380 MW. It can be seen from Figure 6.19

(a) that with A-CAES integration the ramping rate of the plant is increased dramatically. The reason is that the changes of fuel supply and components mass flow rate is reduced when the A-CAES is integrated, as shown in Figure 6.19 (b) and Figure 6.19 (c). In operation, the hybrid system follows the optimised scenario presented in Section 6.4, and the charging and discharging mass flow rates of compressed air are presented in Figure 6.20. The hybrid system is under the compressed air charging process, therefore, the discharging mass flow rate is 0, which is the orange dashed line in Figure 6.20.

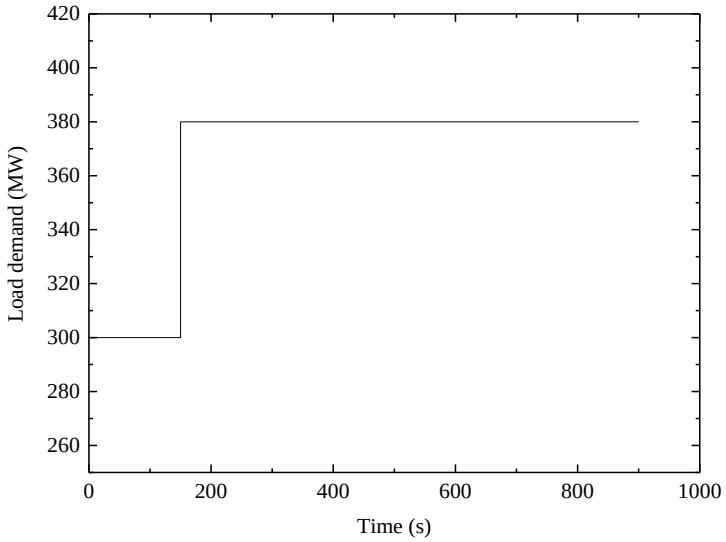

Figure 6.18: Load demand.

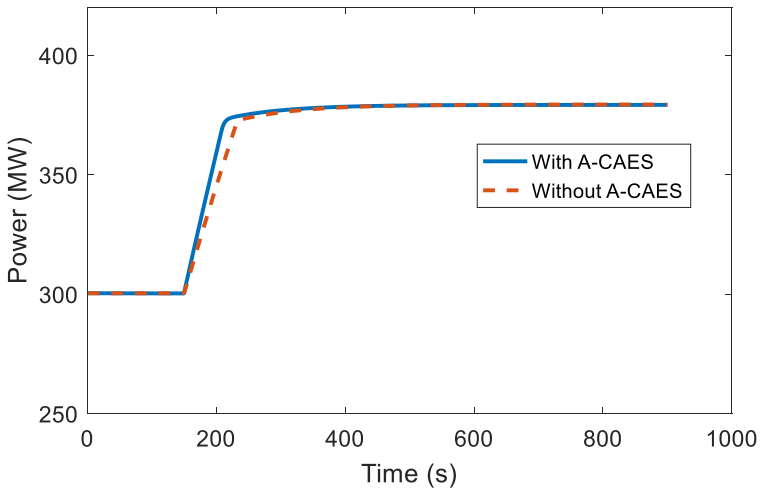

(a)

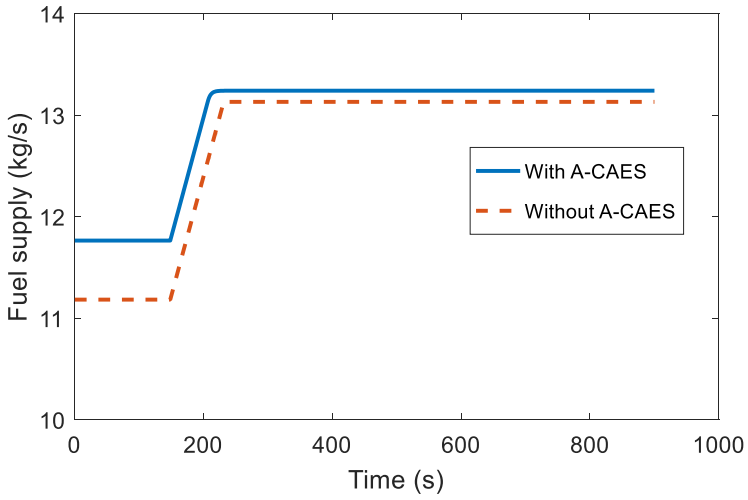

(b)

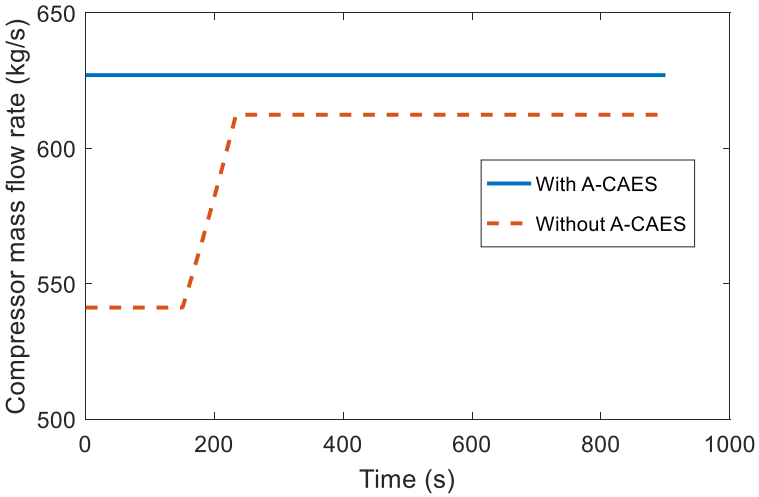

(c)

Figure 6.19: Comparison of two system: (a) output power; (b) Fuel supply; (c) Compressor mass flow rate.

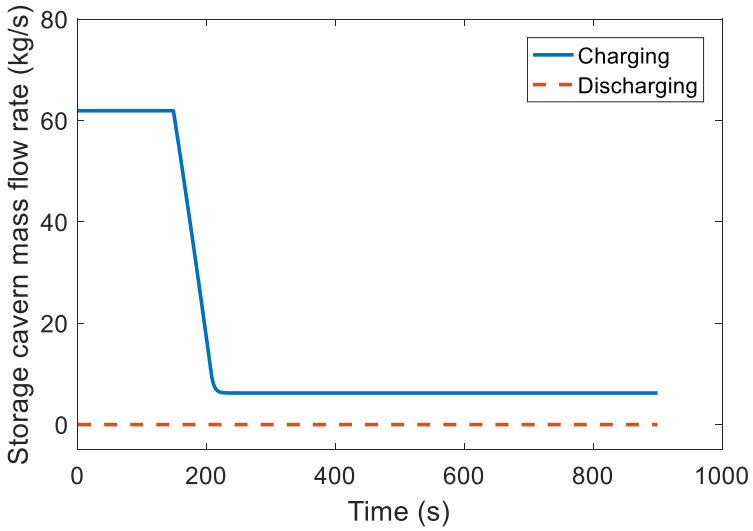

Figure 6.20: Compressed air mass flow rate for the storage cavern.

6.6 Flexible Operation of Hybrid System to Support Wind Power Generation – A Case Study

The mathematical model and integration strategy of the CCGT power plant with A-CAES are introduced to enhance the operation flexibility of CCGT power plants in order to support wind power generation. A case study of the hybrid system flexible operation is presented in this section. The total output power of the hybrid power plant and the wind farm is assumed to be 800 MW. However, the wind farm output power is always varying; thus, the CCGT power plant will generate the power to meet the rest of the load demand with the help of A-CAES. This section presents the dynamic flexible operation of the CCGT power plant with the participation of the A-CAES charging and discharging processes. The simulation results are presented for CCGT power plant dynamics, TES temperature distribution and cavern air temperature and pressure for five hours.

The wind power is downloaded from the database of UK national grid and 10% of it used as the wind farm output power in this study as shown in Figure 6.21. The CCGT power plant has to operate flexibly to match the gap between the load

demand and wind power generation. The CCGT power plant output power is shown in Figure 6.22; the orange hexagram is the load demand and the blue line is the simulated CCGT power plant output power. The gas turbine section takes several seconds to achieve the set value. However, because the thermal inertia of the water steam loop, the steam turbine takes a few minutes to reach the target value. The UK national grid updates wind power every 5 minutes; consequently CCGT power plant will reset its target output power every 5 minutes, as shown in Figure 6.22 (b).

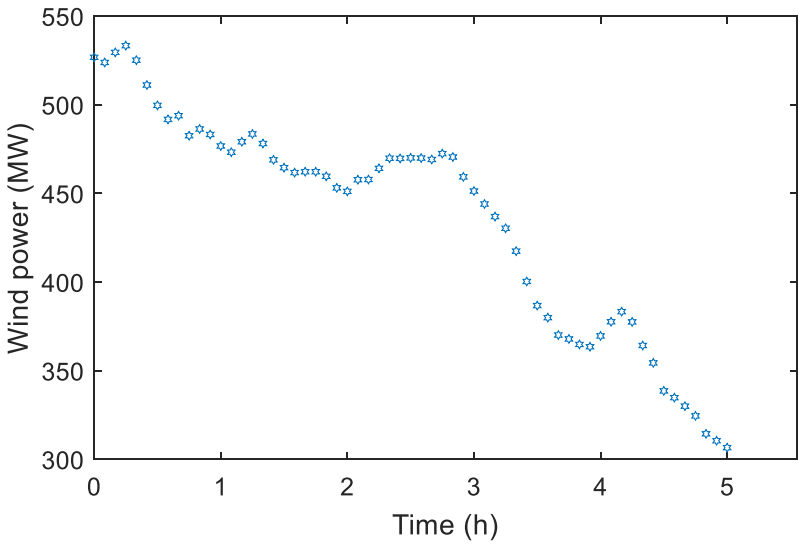

Figure 6.21: Wind farm output power.

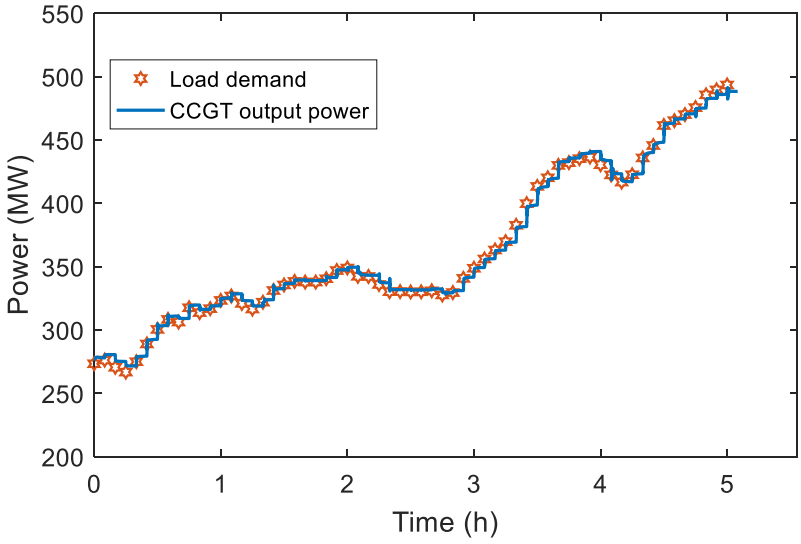

(a)

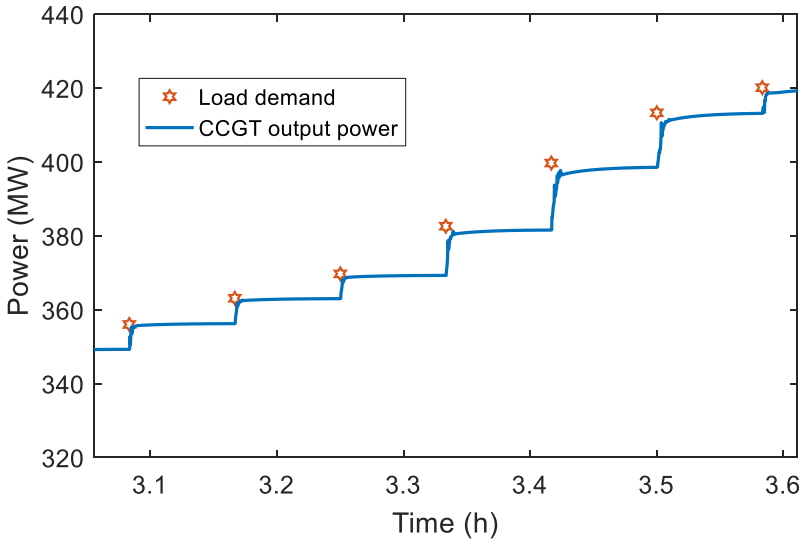

(b)

Figure 6.22: Hybrid system output power and load demand.

In the simulation, the target output power is reset every 5 minutes, then according to the optimised results presented in section 6.4, the mass flow rates of the compressor and gas turbine will be updated every 5 minutes, as shown in Figure 6.23. The blue line is the gas turbine mass flow rate, and the orange line with hexagram is the compressor mass flow rate.

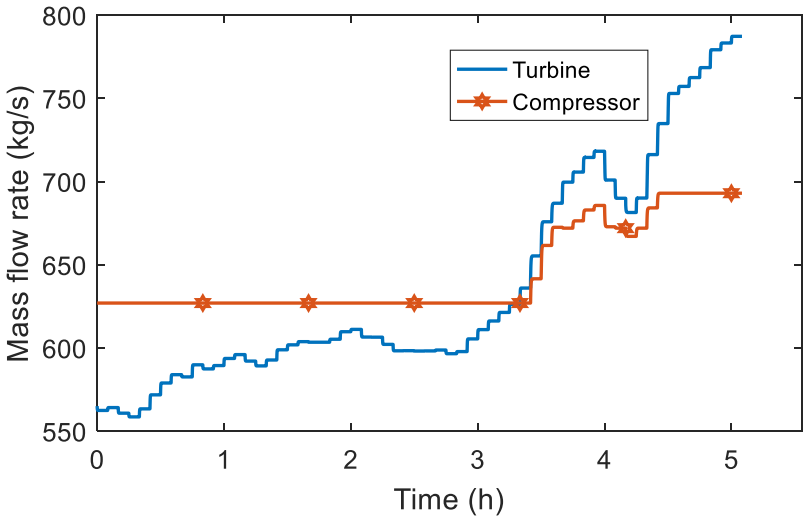

(a)

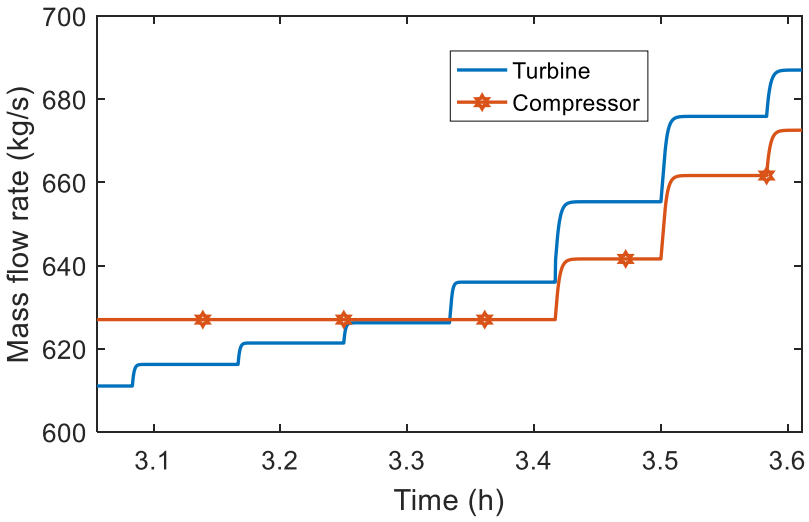

(b)

Figure 6.23: Compressor and gas turbine mass flow rates.

The dynamic mass flow rate of fuel is shown in Figure 6.24 (a). Based on the load demand, the target fuel supply updates every 5 minutes. Considering the components' limitation and safety, the maximum ramp rate of fuel is 0.0235 kg/s, as shown in Figure 6.24 (b).

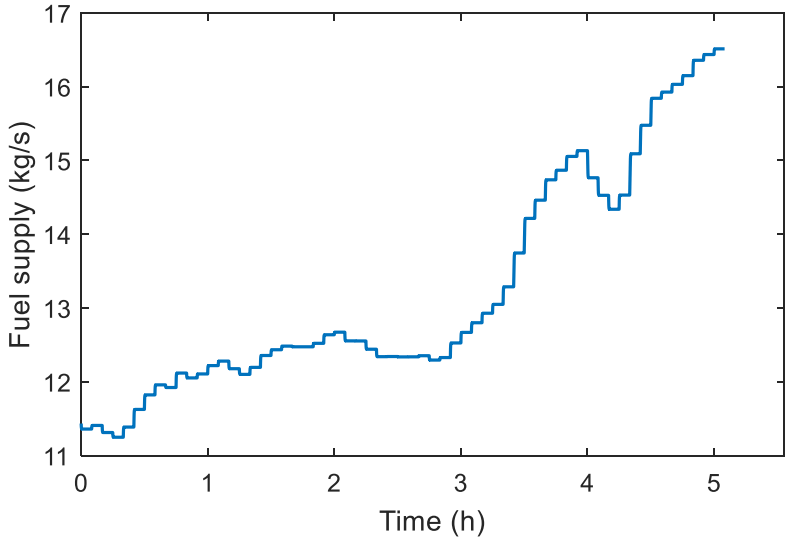

(a)

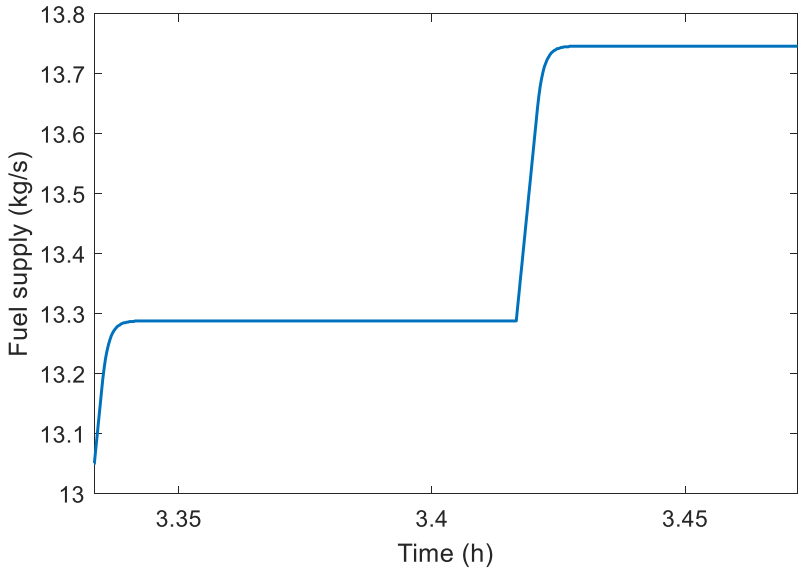

(b)

Figure 6.24: Fuel supply

The charging and discharging mass flow rates of the compressed air are plotted in Figure 6.25. The blue line is the compressed air charging mass flow rate and the orange line with hexagram is the discharging mass flow rate. As shown in Figure 6.25, the charging and discharging mass flow rate of compressed air is 0 kg/s from 3.417 hour to 3.667 hour and from 4.167 hour to 4.25 hour, because the CCGT output power is close to the rated condition, in those two periods.

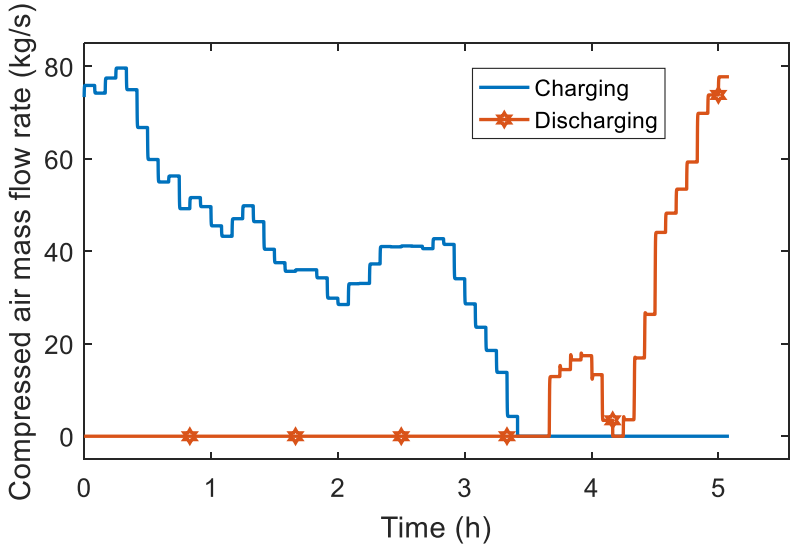

(a)

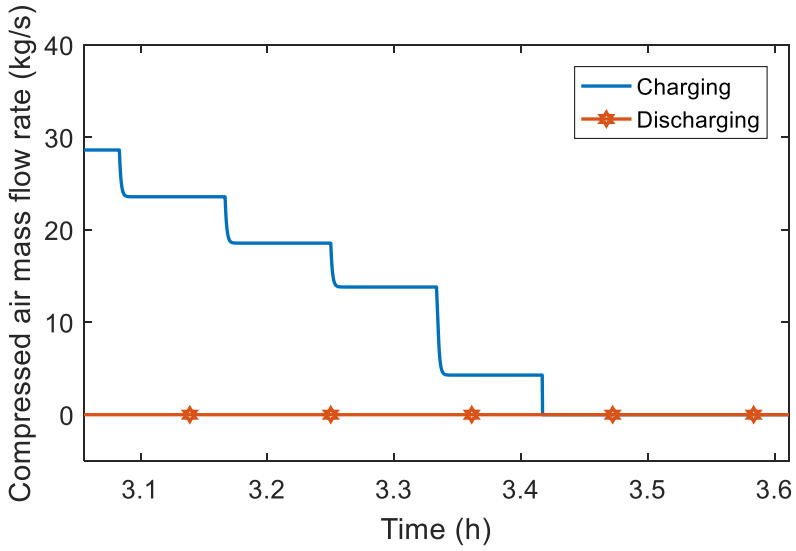

(b)

Figure 6.25: Charging and discharging mass flow rates.

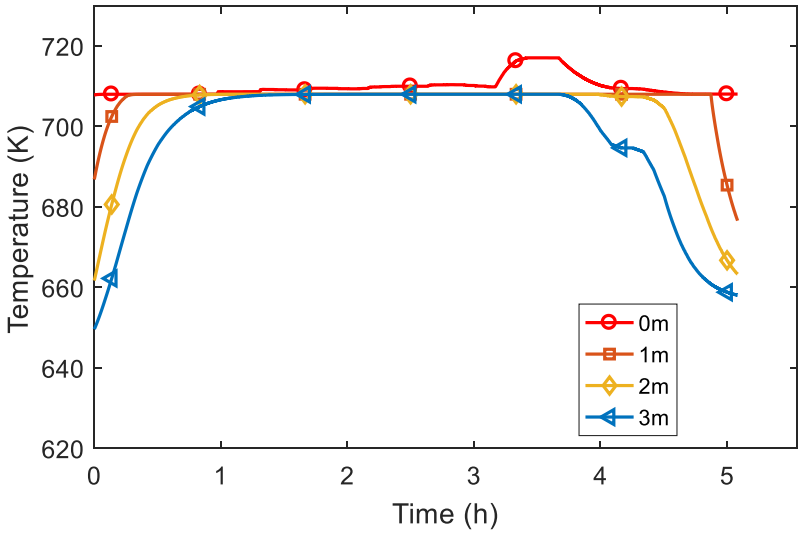

Figure 6.26: KCl & $MgCl_2$ temperatures for various heights.

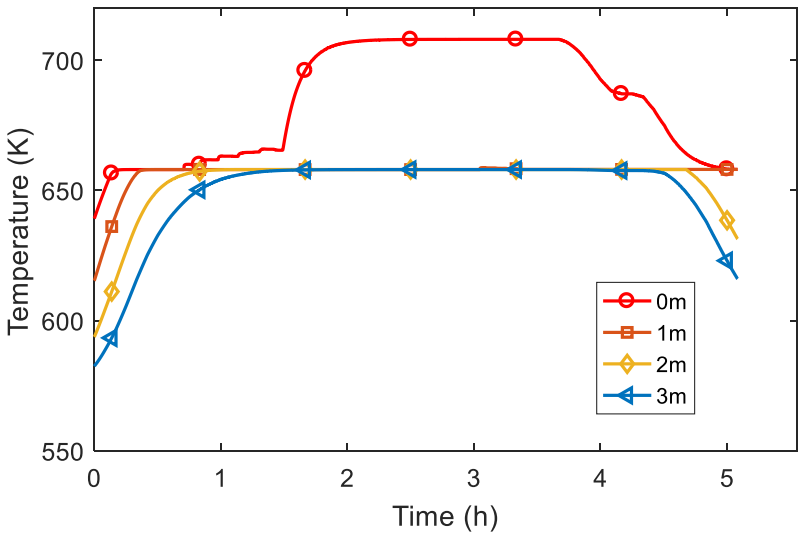

Figure 6.27: $MgCl_2$, NaCl & KCl temperatures for various heights.

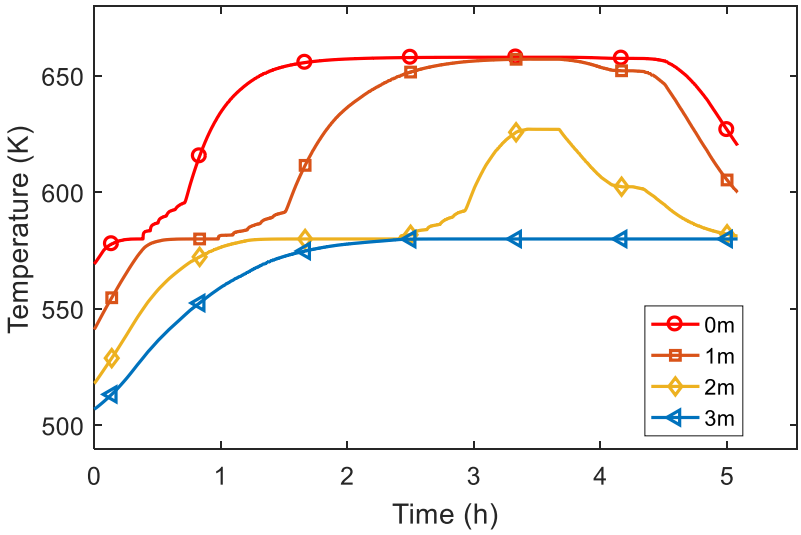

Figure 6.28: $NaNO_3$ temperatures for various heights.

The CLHS temperatures for three materials at four points are shown in Figure 6.26, Figure 6.27 and Figure 6.28, respectively. These four points are at the height of 0 m, 1 m, 2 m and 3 m which are marked in Figure 6.7. It can be seen from the above three figures that the PCMs undergoes several stages during operations of charging, storage and discharging. For instance, the red line with circle in Figure 6.27:

1. From 0 hour to 0.273 hour, the temperature of PCM increases to the phase change temperature.

2. From 0.273 hour to 0.71 hour, the material undergoes a phase change from solid to liquid, and in this stage, the temperature keeps at melting point (658 K).

3. From 0.71 hour to 1.488 hour, the temperature increases slowly, due to the phase of the top side and right side of the measurement point is still solid. Although a lot of heat is transferred to the measurement point, the vast majority of the heat is used to melt surroundings.

4. From 1.488 hour to 2.562 hour, the temperature of measurement point rapidly increases to 708K from 665K.

5. From 2.562 hour to 3.671 hour, since the temperature of PCM is close to the HTF, the temperature stays at 708 K.

6. From 3.671 hour to the end, the temperature of PCM is dropping down. The falling rate of the temperature is low, at about 4.167 hour, because the discharging mass flow rate is small or none. In the end, the temperature maintains at melting point (658 K) and the PCM begins to solidify.

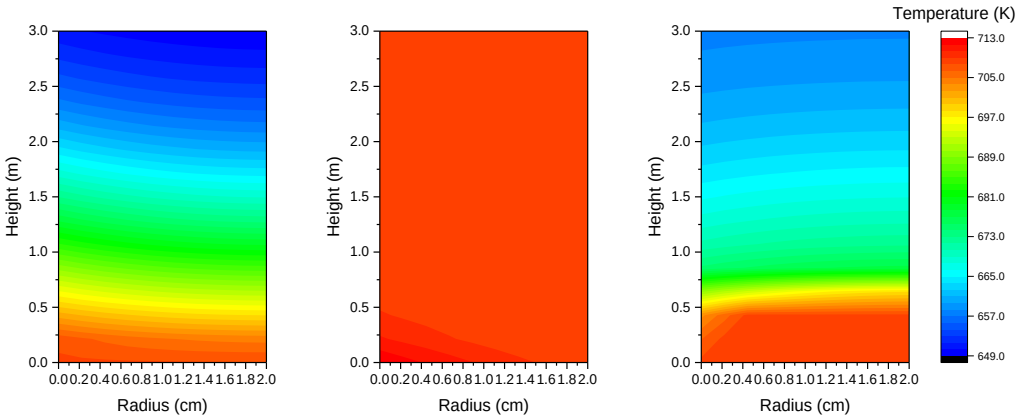

(a) (b) (c)

Figure 6.29: KCl & MgCl2 temperature distribution: (a) initial temperature; (b) temperature at 2.778 hour; (c) temperature at the end.

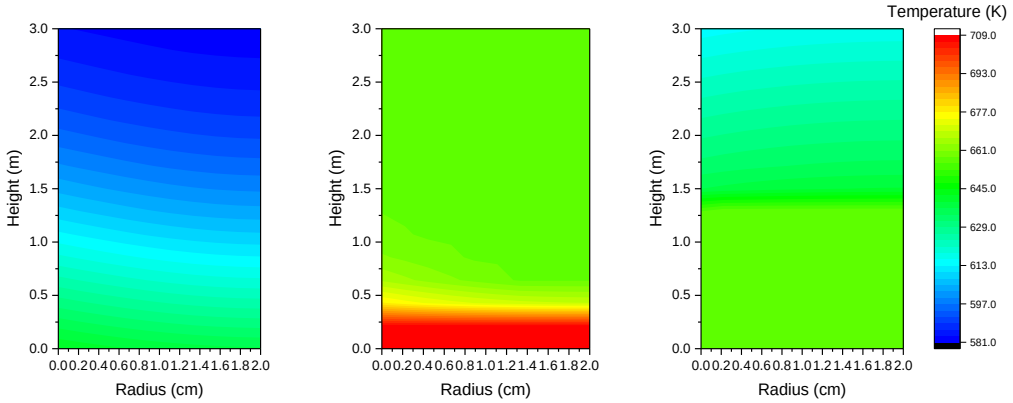

(a) (b) (c)

Figure 6.30: MgCl2, NaCl & KCl temperature distribution: (a) initial temperature; (b) temperature at 2.778 hour; (c) temperature at the end.

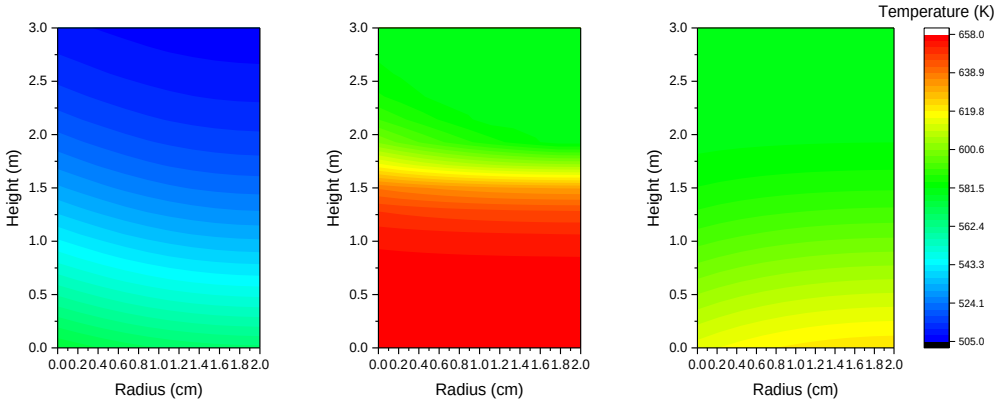

(a) (b) (c)

Figure 6.31: NaNO3 temperature distribution: (a) initial temperature; (b) temperature at 2.778 hour; (c) temperature at the end.

Due to the parallel structure of the CLHS system, the temperature of each set of the canister is assumed to be same at the same height of the CLHS. The plotted temperature profile is the grey shaded area in Figure 6.7. The two-dimensional temperature profiles of PCMS are plotted in Figure 6.29, Figure 6.30 and Figure 6.31 for KCl & $MgCl_2$, $MgCl_2$, NaCl & KCl and $NaNO_3$, respectively. In the above three figures, (a) is the initial temperature of PCMs, (b) is the temperature in the middle of charging process, and (c) is the temperature in the end.

The temperature of compressed air and inner tube are plotted in Figure 6.32. Figure 6.32 (a) is the temperature at 2.778 hour (charging process), and Figure 6.32 (b) is the temperature at the end (discharging process). It can be seen that the compressed air temperature decreases dramatically when it flows into the next PCM from Figure 6.32 (a). At the beginning, the compressed air flows into PCM1 and the temperature decrease to just above 708 K which is the phase change temperature of PCM1. Then the air temperature maintains at this level for a long distance, until the air flows into next PCM-PCM2. This is because the phase change temperature of PCM 2 is much lower than the one of PCM1 and the capacity of latent heat is much higher than sensible heat; therefore, the PCMs absorb a larger amount of heat isothermally. The same is true for the discharging process (Figure 6.32 (b)). For the discharging process, the air flows from right side to left side in order of PCM3, PCM2 and PCM1. As shown in Figure 6.32 (b), there is a sharp change in the middle of PCM2, where air temperature increases dramatically and the tube temperature is close to the melting point of PCM2. If the PCM temperature is lower than melting point, it will heat air by using sensible heat, which relies on temperature change. Therefore, in this process the temperature of PCM drops rapidly, which is the reason for this sharp change.

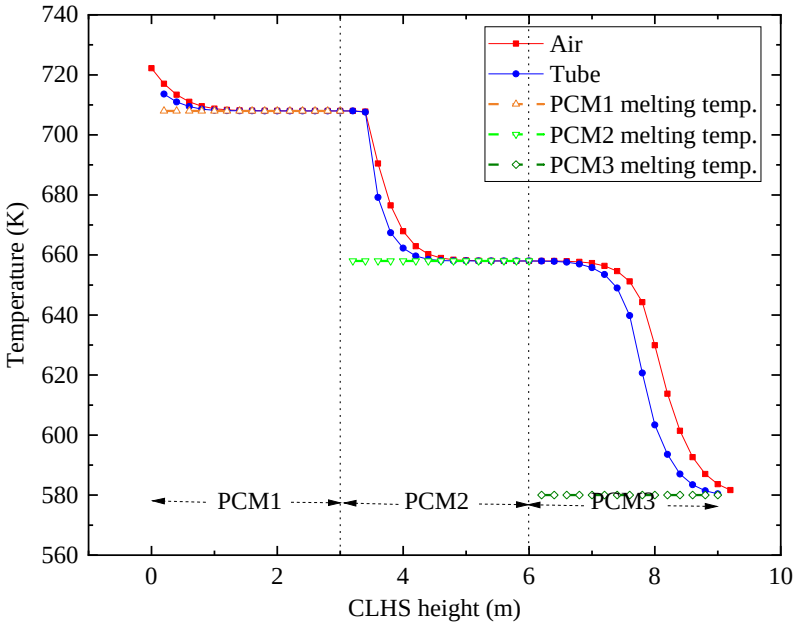

(a)

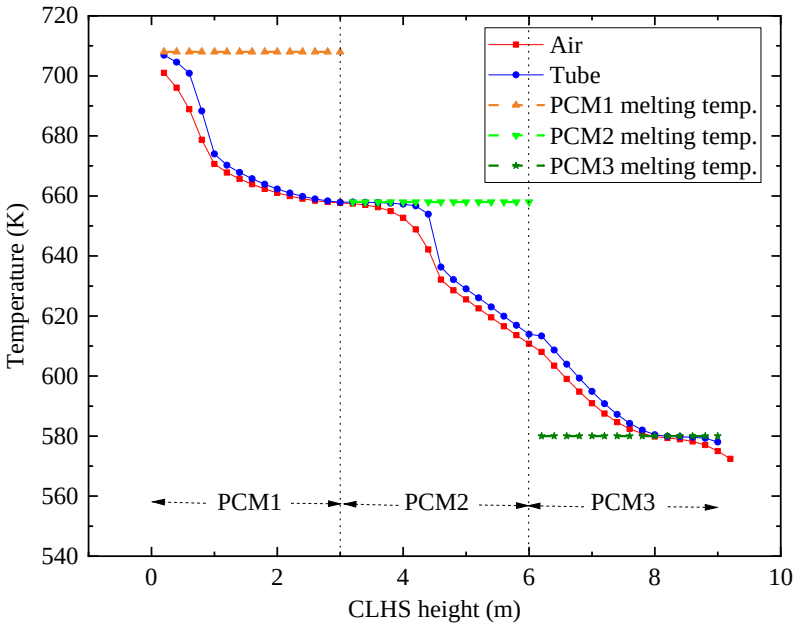

(b)

Figure 6.32: The temperature of compressed air and inner tube: (a) at 2.778 hour; (b) at the end.

The melting temperature of PCM3 is 580 K, so the inlet temperature of SHS is less than 580 K at the beginning of charging. Before the compressed air is stored in the cavern, the temperature of compressed air is expected to drop to around 300 K to 320 K. In order to achieve the these target, the initial temperatures of SHS and cavern air were established. At the cycle simulation initiation, the steatite temperatures are 300, 301, 319, 433, and 501 K for 2 to 10 meters, respectively. The initial conditions of the cavern are listed in Table 6.6, where the initial cavern air temperature and pressure are 27.4 ℃ and 13.2 bar, and the surrounding temperature is set to be 40 ℃, respectively. The cavern specifications are listed in Table 6.1.

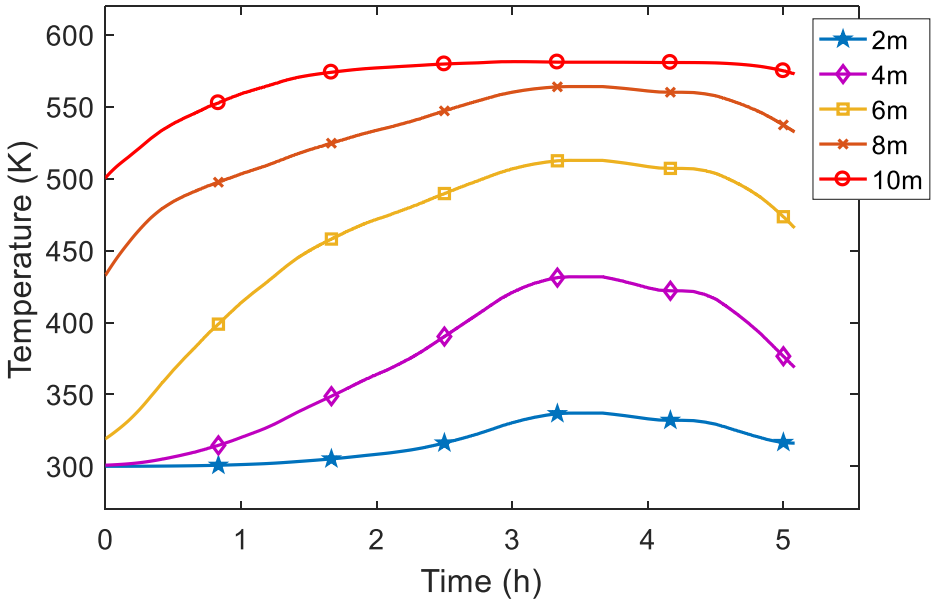

Figure 6.33: SHS temperature for various heights.

The SHS temperatures for various heights are shown in Figure 6.33. The steatite temperatures show a rising trend from the beginning to around 3.333 hour; the steatite temperatures have changed little from 3.333 hour to around 4.444 hour because the air mass flow rate is small or zero; after that, the steatite temperatures begin to decline significantly. According to the simulation results, the SHS temperature variation trend follows the operations of CAES charging, storage and discharging which is plotted in Figure 6.25 (a).

Table 6.6: Initial conditions of cavern.

Parameters	Value, Units
Steatite temperature	40 ℃
Initial air temperature in cavern	27.4 ℃
Initial air pressure in cavern	13.2 bar

The simulated cavern air temperature and pressure are plotted in Figure 6.34 and 6.35, respectively. The initial pressure is 13.2 bar and the initial temperature is 300.6 K. Cavern wall temperature is assumed as a constant. At the beginning and

end of the simulation, the temperature of cavern air is lower than the cavern wall, therefore, heat is transferred to the air within the cavern from the wall. At the middle of the simulation, the temperature of the air is higher than the wall, thus heat is transferred to surroundings from air.

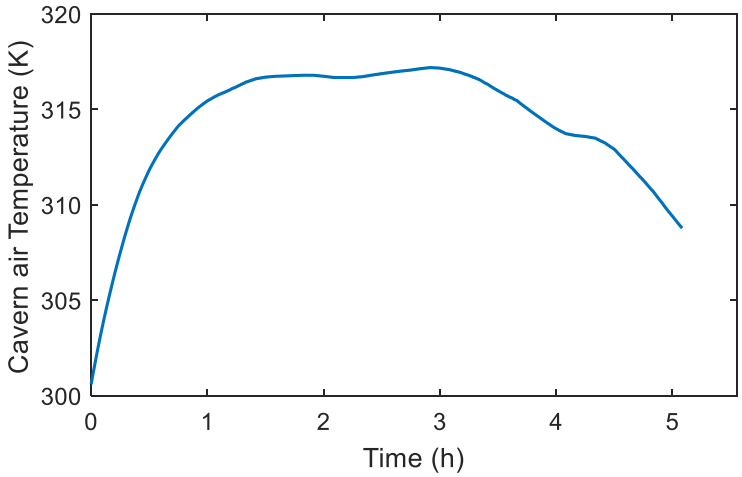

Figure 6.34: Cavern air temperature.

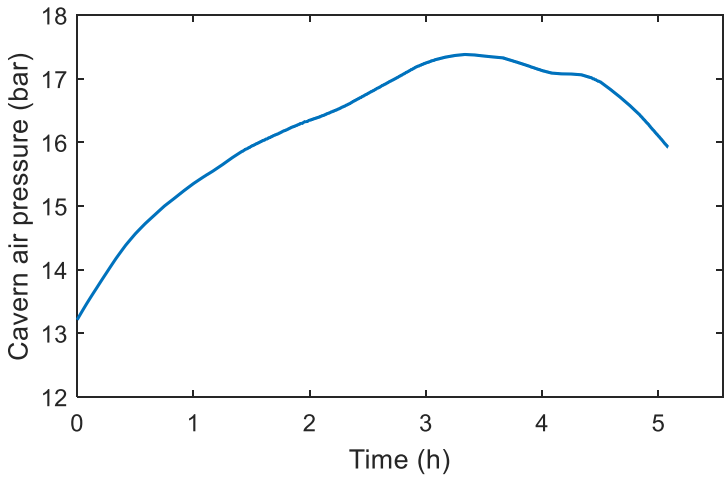

Figure 6.35: Cavern air pressure.

6.7 Summary

In summary, this chapter presents the modelling and simulation study for CCGT power plant integration with A-CAES for power plant flexible operation. The

integration strategies are proposed, and the system is optimised by using a Genetic Algorithms. A case study is performed to demonstrate how the CCGT power plant integration with A-CAES supports wind power generation. The simulation results indicate the following:

1. The integration of CCGT power plant and A-CAES is technically feasible. During the off-peak time, compressed air is separated into two parts: one part for combustion, the remainder for energy storage. During the peak time, the stored compressed air is released to the combustion chamber for power generation. The charging and discharging compressed air mass flow rate should be controlled to guarantee the stability of compressor and turbine. In this chapter, the amounts of stored or released compressed air is analysed and optimised by using Genetic Algorithms according to the ratio between compressed air mass flow rate and fuel consumption.

2. The operation flexibility of CCGT power plants is significantly improved via A-CAES integration. The operation range of the CCGT power plant studied in this chapter is extended to 83-600 MW from 200-430 MW. With the A-CAES integration, the ramp rate of CCGT power plant is enhanced through compressed air charging and discharging processes.

3. The dynamic simulation of a CCGT power plant with A-CAES integration to support wind power generation is performed in this chapter. The simulation results show that the hybrid system bridges the gap between the load demand and wind power generation variations. Based on the wind power generation, the target power output of the hybrid system is updated every 5 minutes. Then the mass flow rates of the compressor and gas turbine are reset according to the optimised results.

4. The proposed system should be placed near the salt cavern, otherwise an over ground tank is needed for compressed air storage. The size of storage system should match the operation requirements, which can be considered as a future research direction.

Chapter 7-Conclusions and Suggested Future Research

The research investigated suitable integration strategies of the thermal power plant with energy storage and identify the performance of power plants while the energy storage system is charging or discharging.

Two types of power plants, supercritical coal-fired power plant and CCGT power plant, were studied to investigate the feasibility of their integration with energy storage for flexible operation. A simulation platform, SimuEngine, developed by Tsinghua University with the collaboration of the University of Warwick is used for supercritical coal-fired power plant dynamic simulation. A commercial software, Aspen Plus, is used for CCGT power plant dynamic modelling and simulation.

This chapter summarises the completed work and its contribution. Some suggestions for future research directions are presented.

7.1 Conclusions

1. The power plant flexible operation causes a significant reduction of lifetime, which is due to the thermo-mechanical fatigue and creep. With the TES integration, the electrical power output can be regulated via controlling thermal energy output for power generation while maintaining the constant thermal generation for both types of power plants. The A-CAES integration provides a mechanism for CCGT power plants to regulate the mechanical energy output for power generation. The thermal and compressed air energy storage can be used as an energy buffer in the energy conversion cycle of thermal power plants.

2. The flexible operation of a 600 MW supercritical coal-fired power plant is carried out by using SimuEngine. The study presents some new TES integration strategies to improve the flexibility of the power plant and to avoid excessive investments. In the proposed system, all that is needed is a TES system which is a relatively cheap section compared with a power plant. The ramping rate of coal-fired power plants is limited by significant delay of energy transfer from coal combustion to water-steam loop. The thesis points out that introducing TES into the water-steam loop of

the power plant is a feasible method to quickly regulate the supercritical coal-fired power plant power generation. With the TES integration, the supercritical coal-fired power plant shows faster dynamic responses to the load demand changes and performs better in the service of grid frequency control.

3. For the TES charging processes, the amount of steam extraction needs to be restricted to a feasible range in order to maintain a stable power output. The first TES charging strategy is to extract steam from the IPTB inlet and loop steam back to the condenser. The second TES strategy is to extract steam from the LPTB inlet and loop steam back to the condenser. The third TES charging strategy is to extract steam from the IPTB inlet and loop steam back to the LPTB inlet. The minimum output power of the first, second and third TES charging strategy is 520 MW, 561 MW and 576.5 MW, respectively. On the other hand, the first TES discharging strategy is to use the stored thermal energy to generate additional steam for the LPTB. The second TES discharging strategy is to use the TES to heat the feed water instead of preheaters. The maximum output power of the first and second TES discharging strategy is 644.4 MW and 634MW, respectively. The first TES charging and discharging strategies lead to the lowest and highest output power. These two strategies are recommended when power plants are required to operate in a wider range.

4. A mathematical model that describes main dynamic features of a 420 MW CCGT power plant developed in Aspen Plus. Under the rated condition, the CCGT power plant combusts 14.46 kg/s natural gas to produce 420 MW power, where 285 MW of the power generated by the gas turbine, and 135 MW of the power generated by steam turbines. The water-steam cycle consists of three pressure levels steam (HP, IP and LP); each level of steam drives one level stream turbine. In comparison with previous Aspen Plus models, all of the earlier models developed in Aspen Plus were steady-state models. In the thesis, a novel modelling approach is proposed to conduct whole system dynamic modelling and simulation in Aspen Plus by defining a “Tear variable” in “calculator”. The modelling strategies and solutions presented in this thesis are also available to convert other Aspen Plus models into dynamic models.

5. With the developed CCGT power plant and CLHS models, the integration strategies during the plant start-up, load-following and standstill processes are proposed and studied. In order to avoid the energy losses of the exhaust gas during the plant start-up process, the excess exhaust gas will pass through the CLHS for thermal storage before discharging into the atmosphere. During the load-following operation, the output power of the CCGT power plant can be controlled by the CLHS charging and discharging processes; meanwhile, the gas turbine section is still operating at the rated load condition. During the off-peak time, part of exhaust gas can be extracted for thermal storage to reduce steam turbine output power. In contrast, the stored heat can be discharged to produce high-temperature and high-pressure steam for the steam turbine to increase the output power. In the plant standstill duration, stored heat can also be used to produce hot gas to maintain the HRSG under the warm condition to reduce the restart-up time.

6. The integration strategy of the CCGT power plant with A-CAES is proposed and studied. The main idea is to decouple the mass flow rate of the compressor and gas turbine with the support of A-CAES integration. In the charging process, a portion of compressed air is separated from the compressor outlet which is then passed through a thermal storage system and finally stored in the storage cavern. In the discharge process, the stored compressed air is released and supplied into a booster to raise the pressure. After that, it flows into a thermal storage system to increase its temperature. Finally, this compressed air mix with the compressed air from the compressor and flows into the combustion chamber for power generation. The compressor and gas turbine mass flow rate is optimised by the Genetic Algorithms for various load demands. The operation flexibility of the CCGT power plant is significantly improved via the A-CAES integration. The operation range of the CCGT power plant is extended to 83-600 MW from 200-430 MW. With the A-CAES integration, the ramp rate of the CCGT power plant is enhanced through the A-CAES charging and discharging processes.

7. A study of a CCGT power plant integration with the A-CAES to support wind power generation is performed. The simulation results descripted the dynamic performance of the whole system including the system power output, the turbine

and compressor mass flow rates, the dynamic temperature profiles of the thermal storage system and the dynamic temperature and pressure of the cavern air. Through the case study, the simulation results illustrate how the hybrid system bridges the gap between the load demand and wind power generation variations. Through the case study, this hybrid system presents the capability to support renewable generation and balance the power generation and load demand.

7.2 Recommendation of Future Research

Apart from the achievements that have been presented in the thesis, there are a lot of challenging topics for future research and further development in this area. From the research conducted, the following recommendations can be made for further research:

1. The integration strategies of the supercritical coal-fired power plant with TES is proposed to improve the flexibility of the power plant. However, it is suggested to include the exergy analysis for each component in the water-steam loop. Moreover, the detailed T-s diagram of power generation processes for each proposed method is suggested to plot, which contributes to a better understanding of the influences on the plant dynamics in the flexible operation.

2. A CCGT power plant dynamic model is developed in Aspen Plus, which is only used for load following simulation study. It is suggested that the model should be extended for the simulation of plant start-up and shut-down procedures. The validated model allows the designers to optimise the plant start-up and shut-down procedures. Besides, only few researchers have developed a detailed physical model to simulate the CCGT power plant start-up and shut-down processes, especially the temperature variation of HRSG.

3. To further improve the TES performance under various operating conditions, efforts could be directed to its optimisation design. It is suggested that the height of each CLHS layer should be optimised according to the heat accumulation rate. Also, the heat transfer efficiency can be regarded as a solution to improve the system

performance, such as replacing PCMs by graphite foams infiltrated PCMs or metal foams embedded PCMs.

4. The hybrid power plant with the CCGT power plant, A-CAES and renewables is suggested to have more attention and research. Such plants can offer significant benefits in terms of the flexibility in matching a fluctuating load demand. Compared with other solutions, such plants may have advantages of energy and cost saving. Last but not least, the maturity of this hybrid power plant may promote the development of the utilisation of renewable sources for power generation.

References

[1] UK Government, "Electricity," E.I.S. Business, Ed., ed, 2018, p. 117.

[2] A. S. Brouwer, M. van den Broek, A. Seebregts, and A. Faaij, "Operational flexibility and economics of power plants in future low-carbon power systems," *Applied Energy*, vol. 156, pp. 107-128, 2015.

[3] Y. Zhao, C. Wang, M. Liu, D. Chong, and J. Yan, "Improving operational flexibility by regulating extraction steam of high-pressure heaters on a 660 MW supercritical coal-fired power plant: A dynamic simulation," *Applied Energy*, vol. 212, pp. 1295-1309, 2018.

[4] M. Razmara, G. Bharati, D. Hanover, M. Shahbakhti, S. Paudyal, and R. Robinett III, "Building-to-grid predictive power flow control for demand response and demand flexibility programs," *Applied Energy*, vol. 203, pp. 128-141, 2017.

[5] C. C. Lin, D. J. Deng, W. Y. Liu, and L. Chen, "Peak load shifting in the internet of energy with energy trading among end-users," *IEEE Access*, vol. 5, pp. 1967-1976, 2017.

[6] M. Huebel, C. Gierow, J. H. Prause, S. Meinke, and E. Hassel, "Simulation of Ancillary Services in Thermal Power Plants in Energy Systems With High Impact of Renewable Energy," in *ASME 2017 Power Conference Joint With ICOPE-17 collocated with the ASME 2017 11th International Conference on Energy Sustainability, the ASME 2017 15th International Conference on Fuel Cell Science, Engineering and Technology, and the ASME 2017 Nuclear Forum*, 2017: American Society of Mechanical Engineers, pp. V002T08A008-V002T08A008.

[7] X. Luo, J. Wang, M. Dooner, and J. Clarke, "Overview of current development in electrical energy storage technologies and the application potential in power system operation," *Applied energy*, vol. 137, pp. 511-536, 2015.

[8] S. Rehman, L. M. Al-Hadhrami, and M. M. Alam, "Pumped hydro energy storage system: A technological review," *Renewable and Sustainable Energy Reviews*, vol. 44, pp. 586-598, 2015.

[9] M. Budt, D. Wolf, R. Span, and J. Yan, "A review on compressed air energy storage: Basic principles, past milestones and recent developments," *Applied Energy*, vol. 170, pp. 250-268, 2016.

[10] P. Chaudhary and M. Rizwan, "Energy management supporting high penetration of solar photovoltaic generation for smart grid using solar forecasts and pumped hydro storage system," *Renewable Energy*, vol. 118, pp. 928-946, 2018.

[11] B. S. Pali and S. Vadhera, "A novel pumped hydro-energy storage scheme with wind energy for power generation at constant voltage in rural areas," *Renewable Energy*, vol. 127, pp. 802-810, 2018.

[12] C. Krupke, J. Wang, J. Clarke, and X. Luo, "Modeling and experimental study of a wind turbine system in hybrid connection with compressed air energy storage," *IEEE Transactions on Energy Conversion*, vol. 32, no. 1, pp. 137-145, 2017.

[13] U. Pelay, L. Luo, Y. Fan, D. Stitou, and M. Rood, "Thermal energy storage systems for concentrated solar power plants," *Renewable and Sustainable Energy Reviews*, vol. 79, pp. 82-100, 2017.

[14] T. Fang and R. Lahdelma, "Optimization of combined heat and power production with heat storage based on sliding time window method," *Applied energy*, vol. 162, pp. 723-732, 2016.

[15] D. Li and J. Wang, "Study of supercritical power plant integration with high temperature thermal energy storage for flexible operation," *Journal of Energy Storage*, vol. 20, pp. 140-152, 2018.

[16] J. Wojcik and J. Wang, "Technical feasibility study of thermal energy storage integration into the conventional power plant cycle," *Energies*, vol. 10, no. 2, p. 205, 2017.

[17] W. Jing, C. H. Lai, W. S. Wong, and M. D. Wong, "A comprehensive study of battery-supercapacitor hybrid energy storage system for standalone PV

power system in rural electrification," *Applied Energy*, vol. 224, pp. 340-356, 2018.

[18] M. T. Lawder *et al.*, "Battery Energy Storage System (BESS) and Battery Management System (BMS) for Grid-Scale Applications," *Proceedings of the IEEE*, vol. 102, no. 6, pp. 1014-1030, 2014.

[19] H. Hesse, M. Schimpe, D. Kucevic, and A. Jossen, "Lithium-ion battery storage for the grid—a review of stationary battery storage system design tailored for applications in modern power grids," *Energies*, vol. 10, no. 12, p. 2107, 2017.

[20] P. Breeze, "An Introduction to Electricity Generation," in *Power Generation Technologies*, 2014, ch. 1, pp. 1-13.

[21] P. Breeze, "An Introduction to Coal-Fired Power Generation," in *Coal-Fired Generation*, 2015, ch. 1, pp. 1-7.

[22] H. Termuehlen and W. Emsperger, "Evolutionary development of coal-fired power plants," in *Clean and Efficient Coal-Fired Power Plants*: ASME Press, 2003.

[23] D. A. Tillman, "The Overarching Issues," in *Coal-Fired Electricity and Emissions Control*, D. A. Tillman Ed., 2018, ch. 1, pp. 1-27.

[24] D. K. Sarkar, "Pulverized Coal-Fired Boilers," in *Thermal Power Plant*, D. K. Sarkar Ed., 2015, ch. 4, pp. 139-158.

[25] A. Di Gianfrancesco, "The fossil fuel power plants technology," in *Materials for ultra-supercritical and advanced ultra-supercritical power plants*: Elsevier, 2017, pp. 1-49.

[26] H. Kimura, T. Sato, C. Bergins, S. Imano, and E. Saito, "Development of technologies for improving efficiency of large coal-fired thermal power plants," *Hitachi review*, vol. 60, no. 7, p. 365, 2011.

[27] P. Breeze, "An Introduction to Gas-Fired Power Generation," in *Gas-turbine power generation*, P. Breeze Ed.: Academic Press, 2016, ch. 1, pp. 1-7.

[28] F. Díaz-González, M. Hau, A. Sumper, and O. Gomis-Bellmunt, "Participation of wind power plants in system frequency control: Review of

grid code requirements and control methods," *Renewable and Sustainable Energy Reviews*, vol. 34, pp. 551-564, 2014.

[29] D. Sarkar, "Gas Turbine and Heat Recovery Steam Generator," in *Thermal power plant: design and operation*: Elsevier, 2015, ch. 7, pp. 239-283.

[30] P. Breeze, "Gas-Fired Power Generation Technology," in *Gas-turbine power generation*, P. Breeze Ed.: Academic Press, 2016, ch. 3, pp. 21-29.

[31] P. Breeze, "Natural Gas–fired Gas Turbines and Combined Cycle Power Plants," in *Power generation technologies*, P. Breeze Ed.: Newnes, 2014, ch. 4, pp. 67-91.

[32] P. Breeze, "Gas Turbines," in *Gas-turbine power generation*, P. Breeze Ed.: Academic Press, 2016, ch. 4, pp. 31-42.

[33] J. Hentschel and H. Spliethoff, "A parametric approach for the valuation of power plant flexibility options," *Energy Reports*, vol. 2, pp. 40-47, 2016.

[34] P. Breeze, "Coal-fired Power Plants," in *Power Generation Technologies*, 2014, ch. 3, pp. 29-65.

[35] A. Ohji and M. Haraguchi, "Steam turbine cycles and cycle design optimization: The Rankine cycle, thermal power cycles, and IGCC power plants," in *Advances in Steam Turbines for Modern Power Plants*: Elsevier, 2017, ch. 2, pp. 11-40.

[36] Y. Tan, L. Jia, Y. Wu, and E. Anthony, "Experiences and results on a 0.8 MWth oxy-fuel operation pilot-scale circulating fluidized bed," *Applied Energy*, vol. 92, pp. 343-347, 2012.

[37] Z. Guo, Q. Wang, M. Fang, Z. Luo, and K. Cen, "Thermodynamic and economic analysis of polygeneration system integrating atmospheric pressure coal pyrolysis technology with circulating fluidized bed power plant," *Applied Energy*, vol. 113, pp. 1301-1314, 2014.

[38] S. Rezvani, Y. Huang, D. McIlveen-Wright, N. Hewitt, and J. D. Mondol, "Comparative assessment of coal fired IGCC systems with CO2 capture using physical absorption, membrane reactors and chemical looping," *Fuel*, vol. 88, no. 12, pp. 2463-2472, 2009.

[39] F. Emun, M. Gadalla, T. Majozi, and D. Boer, "Integrated gasification combined cycle (IGCC) process simulation and optimization," *Computers & chemical engineering*, vol. 34, no. 3, pp. 331-338, 2010.

[40] M. S. Forsthoffer, "Gas Turbines," in *More Best Practices for Rotating Equipment*: Butterworth-Heinemann, 2017, ch. 6, pp. 287-332.

[41] A. Chaibakhsh and A. Ghaffari, "Steam turbine model," *Simulation Modelling Practice and Theory*, vol. 16, no. 9, pp. 1145-1162, 2008.

[42] M. Topel, R. Guédez, and B. Laumert, "Impact of increasing steam turbine flexibility on the annual performance of a direct steam generation tower power plant," *Energy Procedia*, vol. 69, pp. 1171-1180, 2015.

[43] C. Wang, Y. Zhao, M. Liu, Y. Qiao, D. Chong, and J. Yan, "Peak shaving operational optimization of supercritical coal-fired power plants by revising control strategy for water-fuel ratio," *Applied Energy*, vol. 216, pp. 212-223, 2018.

[44] F. Alobaid, R. Postler, J. Ströhle, B. Epple, and H.-G. Kim, "Modeling and investigation start-up procedures of a combined cycle power plant," *Applied Energy*, vol. 85, no. 12, pp. 1173-1189, 2008.

[45] Y. Yoshida, T. Yoshida, Y. Enomoto, N. Osaki, Y. Nagahama, and Y. Tsuge, "Start-Up Optimization of Combined Cycle Power Plants: A Field Test in a Commercial Power Plant," *Journal of Engineering for Gas Turbines and Power*, vol. 141, no. 3, p. 031002, 2019.

[46] A. Nannarone and S. A. Klein, "Start-Up Optimization of a CCGT Power Station Using Model Based Gas Turbine Control," in *ASME Turbo Expo 2018: Turbomachinery Technical Conference and Exposition*, 2018: American Society of Mechanical Engineers, pp. V003T06A011-V003T06A011.

[47] J. D. Wojcik and J. Wang, "Feasibility study of Combined Cycle Gas Turbine (CCGT) power plant integration with Adiabatic Compressed Air Energy Storage (ACAES)," *Applied Energy*, vol. 221, pp. 477-489, 2018.

[48] D. Li, Y. Hu, W. He, and J. Wang, "Dynamic modelling and simulation of a combined-cycle power plant integration with thermal energy storage," in

Automation and Computing (ICAC), 2017 23rd International Conference on, 2017: IEEE, pp. 1-6.

[49] L. Barelli and A. Ottaviano, "Supercharged gas turbine combined cycle: An improvement in plant flexibility and efficiency," *Energy,* vol. 81, pp. 615-626, 2015.

[50] T. Nuytten, B. Claessens, K. Paredis, J. Van Bael, and D. Six, "Flexibility of a combined heat and power system with thermal energy storage for district heating," *Applied Energy,* vol. 104, pp. 583-591, 2013.

[51] K. M. Powell and T. F. Edgar, "Modeling and control of a solar thermal power plant with thermal energy storage," *Chemical Engineering Science,* vol. 71, pp. 138-145, 2012.

[52] M. Johnson, J. Vogel, M. Hempel, A. Dengel, M. Seitz, and B. Hachmann, "High temperature latent heat thermal energy storage integration in a co-gen plant," *Energy Procedia,* vol. 73, pp. 281-288, 2015.

[53] J. Freeman, I. Guarracino, S. A. Kalogirou, and C. N. Markides, "A small-scale solar organic Rankine cycle combined heat and power system with integrated thermal energy storage," *Applied Thermal Engineering,* vol. 127, pp. 1543-1554, 2017.

[54] R. Yuan, J. Ye, J. Lei, and T. Li, "Integrated combined heat and power system dispatch considering electrical and thermal energy storage," *Energies,* vol. 9, no. 6, p. 474, 2016.

[55] M. Bianchi, A. De Pascale, and F. Melino, "Performance analysis of an integrated CHP system with thermal and Electric Energy Storage for residential application," *Applied Energy,* vol. 112, pp. 928-938, 2013.

[56] K. Nithyanandam and R. Pitchumani, "Cost and performance analysis of concentrating solar power systems with integrated latent thermal energy storage," *Energy,* vol. 64, pp. 793-810, 2014.

[57] S. Guo, "Model Based Analysis of Power Plant Integrated with a Post Combustion Carbon Capture Process," University of Warwick, 2015, PhD thesis.

[58] B. Tashtoush, M. Molhim, and M. Al-Rousan, "Dynamic model of an HVAC system for control analysis," *Energy,* vol. 30, no. 10, pp. 1729-1745, 2005.

[59] S. Quoilin, R. Aumann, A. Grill, A. Schuster, V. Lemort, and H. Spliethoff, "Dynamic modeling and optimal control strategy of waste heat recovery Organic Rankine Cycles," *Applied energy,* vol. 88, no. 6, pp. 2183-2190, 2011.

[60] M. Draganescu *et al.*, "Generalized predictive control for superheated steam temperature regulation in a supercritical coal-fired power plant," *CSEE Journal of Power and energy Systems,* vol. 1, no. 1, pp. 69-77, 2015.

[61] M. Draganescu, "Study of Supercritical Coal-Fired Power Plant Dynamic Responses and Control for Grid Code Compliance," University of Warwick, 2015, PhD thesis.

[62] M. Ameri, P. Ahmadi, and A. Hamidi, "Energy, exergy and exergoeconomic analysis of a steam power plant: A case study," *International Journal of Energy Research,* vol. 33, no. 5, pp. 499-512, 2009.

[63] I. H. Aljundi, "Energy and exergy analysis of a steam power plant in Jordan," *Applied thermal engineering,* vol. 29, no. 2-3, pp. 324-328, 2009.

[64] B. Cárdenas and N. León, "High temperature latent heat thermal energy storage: Phase change materials, design considerations and performance enhancement techniques," *Renewable and sustainable energy reviews,* vol. 27, pp. 724-737, 2013.

[65] T. Yan, R. Wang, T. Li, L. Wang, and I. T. Fred, "A review of promising candidate reactions for chemical heat storage," *Renewable and Sustainable Energy Reviews,* vol. 43, pp. 13-31, 2015.

[66] S. Kuravi, J. Trahan, D. Y. Goswami, M. M. Rahman, and E. K. Stefanakos, "Thermal energy storage technologies and systems for concentrating solar power plants," *Progress in Energy and Combustion Science,* vol. 39, no. 4, pp. 285-319, 2013.

[67] F. Agyenim, N. Hewitt, P. Eames, and M. Smyth, "A review of materials, heat transfer and phase change problem formulation for latent heat thermal

energy storage systems (LHTESS)," *Renewable and sustainable energy reviews,* vol. 14, no. 2, pp. 615-628, 2010.

[68] M. M. Kenisarin, "High-temperature phase change materials for thermal energy storage," *Renewable and Sustainable Energy Reviews,* vol. 14, no. 3, pp. 955-970, 2010.

[69] Y. Tian and C.-Y. Zhao, "A review of solar collectors and thermal energy storage in solar thermal applications," *Applied energy,* vol. 104, pp. 538-553, 2013.

[70] W. Murrell, L. Ran, and J. Wang, "Modelling UK power system frequency response with increasing wind penetration," in *Innovative Smart Grid Technologies-Asia (ISGT Asia), 2014 IEEE*, 2014: IEEE, pp. 1-6.

[71] V. Knap, S. K. Chaudhary, D.-I. Stroe, M. Swierczynski, B.-I. Craciun, and R. Teodorescu, "Sizing of an energy storage system for grid inertial response and primary frequency reserve," *IEEE Transactions on Power Systems,* vol. 31, no. 5, pp. 3447-3456, 2016.

[72] Y. Huang, G. Mu, L. Li, G. Yan, J. Liu, and Z. Wang, "Method of obtaining the sensitive disturbances of frequency control system including AGC by analyzing the frequency-response trajectory," in *Innovative Smart Grid Technologies-Asia (ISGT Asia), 2012 IEEE*, 2012: IEEE, pp. 1-5.

[73] N. Mertens, F. Alobaid, T. Lanz, B. Epple, and H.-G. Kim, "Dynamic simulation of a triple-pressure combined-cycle plant: Hot start-up and shutdown," *Fuel,* vol. 167, pp. 135-148, 2016.

[74] F. Alobaid, S. Pfeiffer, B. Epple, C.-Y. Seon, and H.-G. Kim, "Fast start-up analyses for Benson heat recovery steam generator," *Energy,* vol. 46, no. 1, pp. 295-309, 2012.

[75] T. Adams and N. Mac Dowell, "Off-design point modelling of a 420 MW CCGT power plant integrated with an amine-based post-combustion CO2 capture and compression process," *Applied Energy,* vol. 178, pp. 681-702, 2016.

[76] E. Pihl, S. Heyne, H. Thunman, and F. Johnsson, "Highly efficient electricity generation from biomass by integration and hybridization with

combined cycle gas turbine (CCGT) plants for natural gas," *Energy,* vol. 35, no. 10, pp. 4042-4052, 2010.

[77] R. Canepa and M. Wang, "Techno-economic analysis of a CO2 capture plant integrated with a commercial scale combined cycle gas turbine (CCGT) power plant," *Applied Thermal Engineering,* vol. 74, pp. 10-19, 2015.

[78] A. Mathisen, H. Sørensen, M. C. Melaaen, and G.-I. Müller, "Investigation into optimal CO2 concentration for CO2 capture from aluminium production," 2013.

[79] J. François *et al.*, "Estimation of the energy efficiency of a wood gasification CHP plant using Aspen Plus," *Chemical engineering transactions,* vol. 29, pp. 769-774, 2012.

[80] W. Ma, Y. Liu, M. Su, and N. Yu, "Multi-stage axial flow compressors characteristics estimation based on system identification," *Energy conversion and management,* vol. 49, no. 2, pp. 143-150, 2008.

[81] S. M. H. Mahmood, M. G. Turner, and K. Siddappaji, "Flow characteristics of an optimized axial compressor rotor using smooth design parameters," in *ASME Turbo Expo 2016: Turbomachinery Technical Conference and Exposition*, 2016: American Society of Mechanical Engineers, pp. V02CT45A018-V02CT45A018.

[82] M. Ameri, P. Ahmadi, and S. Khanmohammadi, "Exergy analysis of a 420 MW combined cycle power plant," *International Journal of Energy Research,* vol. 32, no. 2, pp. 175-183, 2008.

[83] M. T. Mansouri, P. Ahmadi, A. G. Kaviri, and M. N. M. Jaafar, "Exergetic and economic evaluation of the effect of HRSG configurations on the performance of combined cycle power plants," *Energy Conversion and Management,* vol. 58, pp. 47-58, 2012.

[84] N. Zhang and R. Cai, "Analytical solutions and typical characteristics of part-load performances of single shaft gas turbine and its cogeneration," *Energy Conversion and Management,* vol. 43, no. 9-12, pp. 1323-1337, 2002.

[85] C. Day, M. Stephan, and L. Oellrich, "A new flow calorimeter for the measurement of the isobaric enthapy increment and the isenthalpic Joule–Thomson effect. Results for methane and (methane+ ethane)," *The Journal of Chemical Thermodynamics,* vol. 29, no. 9, pp. 949-971, 1997.

[86] P. M. Mathias, H. C. Klotz, and J. M. Prausnitz, "Equation-of-state mixing rules for multicomponent mixtures: the problem of invariance," *Fluid Phase Equilibria,* vol. 67, pp. 31-44, 1991.

[87] W. Wagner and A. Pruß, "The IAPWS formulation 1995 for the thermodynamic properties of ordinary water substance for general and scientific use," *Journal of physical and chemical reference data,* vol. 31, no. 2, pp. 387-535, 2002.

[88] *Aspen Properties,* A. Technology, 2012.

[89] Y. You and L. Li, "Sequential Modular Approach in the Simulation of Gas Transmission Station," in *2012 Spring Congress on Engineering and Technology*, 2012: IEEE, pp. 1-3.

[90] M. Pan *et al.*, "Application of optimal design methodologies in retrofitting natural gas combined cycle power plants with CO2 capture," *Applied energy,* vol. 161, pp. 695-706, 2016.

[91] Z. Liu and I. A. Karimi, "Simulating combined cycle gas turbine power plants in Aspen HYSYS," *Energy conversion and management,* vol. 171, pp. 1213-1225, 2018.

[92] A. Benato, S. Bracco, A. Stoppato, and A. Mirandola, "Dynamic simulation of combined cycle power plant cycling in the electricity market," *Energy Conversion and Management,* vol. 107, pp. 76-85, 2016.

[93] J. Xu, R. Wang, and Y. Li, "A review of available technologies for seasonal thermal energy storage," *Solar Energy,* vol. 103, pp. 610-638, 2014.

[94] M. Hänchen, S. Brückner, and A. Steinfeld, "High-temperature thermal storage using a packed bed of rocks–heat transfer analysis and experimental validation," *Applied Thermal Engineering,* vol. 31, no. 10, pp. 1798-1806, 2011.

[95] P. Goli, S. Legedza, A. Dhar, R. Salgado, J. Renteria, and A. A. Balandin, "Graphene-enhanced hybrid phase change materials for thermal management of Li-ion batteries," *Journal of Power Sources,* vol. 248, pp. 37-43, 2014.

[96] F. Ascione, N. Bianco, R. F. De Masi, F. de'Rossi, and G. P. Vanoli, "Energy refurbishment of existing buildings through the use of phase change materials: Energy savings and indoor comfort in the cooling season," *Applied Energy,* vol. 113, pp. 990-1007, 2014.

[97] H. Tian, L. Du, X. Wei, S. Deng, W. Wang, and J. Ding, "Enhanced thermal conductivity of ternary carbonate salt phase change material with Mg particles for solar thermal energy storage," *Applied Energy,* vol. 204, pp. 525-530, 2017.

[98] W. He *et al.*, "Study of cycle-to-cycle dynamic characteristics of adiabatic Compressed Air Energy Storage using packed bed Thermal Energy Storage," *Energy,* vol. 141, pp. 2120-2134, 2017.

[99] H. Ji *et al.*, "Enhanced thermal conductivity of phase change materials with ultrathin-graphite foams for thermal energy storage," *Energy & Environmental Science,* vol. 7, no. 3, pp. 1185-1192, 2014.

[100] S. Yu, X. Wang, and D. Wu, "Microencapsulation of n-octadecane phase change material with calcium carbonate shell for enhancement of thermal conductivity and serving durability: synthesis, microstructure, and performance evaluation," *Applied Energy,* vol. 114, pp. 632-643, 2014.

[101] R. Elbahjaoui and H. El Qarnia, "Transient behavior analysis of the melting of nanoparticle-enhanced phase change material inside a rectangular latent heat storage unit," *Applied Thermal Engineering,* vol. 112, pp. 720-738, 2017.

[102] H. Eslamnezhad and A. B. Rahimi, "Enhance heat transfer for phase-change materials in triplex tube heat exchanger with selected arrangements of fins," *Applied Thermal Engineering,* vol. 113, pp. 813-821, 2017.

[103] A. Sciacovelli, F. Gagliardi, and V. Verda, "Maximization of performance of a PCM latent heat storage system with innovative fins," *Applied Energy,* vol. 137, pp. 707-715, 2015.

[104] D. Lefebvre and F. H. Tezel, "A review of energy storage technologies with a focus on adsorption thermal energy storage processes for heating applications," *Renewable and Sustainable Energy Reviews,* vol. 67, pp. 116-125, 2017.

[105] K. Lafdi, O. Mesalhy, and A. Elgafy, "Graphite foams infiltrated with phase change materials as alternative materials for space and terrestrial thermal energy storage applications," *Carbon,* vol. 46, no. 1, pp. 159-168, 2008.

[106] S. Patankar, *Numerical heat transfer and fluid flow*. CRC press, 1980.

[107] P. Verma and S. Singal, "Review of mathematical modeling on latent heat thermal energy storage systems using phase-change material," *Renewable and Sustainable Energy Reviews,* vol. 12, no. 4, pp. 999-1031, 2008.

[108] N. Vyshak and G. Jilani, "Numerical analysis of latent heat thermal energy storage system," *Energy conversion and management,* vol. 48, no. 7, pp. 2161-2168, 2007.

[109] A. Gil *et al.*, "State of the art on high temperature thermal energy storage for power generation. Part 1—Concepts, materials and modellization," *Renewable and Sustainable Energy Reviews,* vol. 14, no. 1, pp. 31-55, 2010.

[110] A. Pasha, "Combined cycle power plant start-up effects and constraints of the HRSG," in *ASME 1992 International Gas Turbine and Aeroengine Congress and Exposition*, 1992: American Society of Mechanical Engineers, pp. V004T11A016-V004T11A016.

[111] T. Kim, D. Lee, and S. Ro, "Analysis of thermal stress evolution in the steam drum during start-up of a heat recovery steam generator," *Applied Thermal Engineering,* vol. 20, no. 11, pp. 977-992, 2000.

[112] W. Zhao, D. M. France, W. Yu, T. Kim, and D. Singh, "Phase change material with graphite foam for applications in high-temperature latent heat storage systems of concentrated solar power plants," *Renewable Energy,* vol. 69, pp. 134-146, 2014.

[113] X. Luo *et al.*, "Review of Voltage and Frequency Grid Code Specifications for Electrical Energy Storage Applications," *Energies,* vol. 11, no. 5, p. 1070, 2018.

[114] W. He *et al.*, "Exergy storage of compressed air in cavern and cavern volume estimation of the large-scale compressed air energy storage system," *Applied Energy,* vol. 208, pp. 745-757, 2017.

[115] C. Xia, Y. Zhou, S. Zhou, P. Zhang, and F. Wang, "A simplified and unified analytical solution for temperature and pressure variations in compressed air energy storage caverns," *Renewable Energy,* vol. 74, pp. 718-726, 2015.

[116] M. Raju and S. K. Khaitan, "Modeling and simulation of compressed air storage in caverns: a case study of the Huntorf plant," *Applied Energy,* vol. 89, no. 1, pp. 474-481, 2012.

[117] X. Luo *et al.*, "Feasibility study of a simulation software tool development for dynamic modelling and transient control of adiabatic compressed air energy storage with its electrical power system applications," *Applied energy,* vol. 228, pp. 1198-1219, 2018.

[118] Y. Kim, D. Shin, and D. Favrat, "Operating characteristics of constant-pressure compressed air energy storage (CAES) system combined with pumped hydro storage based on energy and exergy analysis," *Energy,* vol. 36, no. 10, pp. 6220-6233, 2011.

[119] L. Geissbühler *et al.*, "Pilot-scale demonstration of advanced adiabatic compressed air energy storage, Part 1: Plant description and tests with sensible thermal-energy storage," *Journal of Energy Storage,* vol. 17, pp. 129-139, 2018.

[120] I. Arsie, V. Marano, G. Nappi, and G. Rizzo, "A model of a hybrid power plant with wind turbines and compressed air energy storage," in *ASME 2005 Power Conference*, 2005: American Society of Mechanical Engineers, pp. 987-1000.

[121] R. Kushnir, A. Dayan, and A. Ullmann, "Temperature and pressure variations within compressed air energy storage caverns," *International Journal of Heat and Mass Transfer,* vol. 55, no. 21-22, pp. 5616-5630, 2012.

[122] G. Zanganeh, A. Pedretti, A. Haselbacher, and A. Steinfeld, "Design of packed bed thermal energy storage systems for high-temperature industrial process heat," *Applied Energy*, vol. 137, pp. 812-822, 2015.

[123] G. Zanganeh, A. Pedretti, S. Zavattoni, M. Barbato, and A. Steinfeld, "Packed-bed thermal storage for concentrated solar power–Pilot-scale demonstration and industrial-scale design," *Solar Energy*, vol. 86, no. 10, pp. 3084-3098, 2012.

[124] G. Zanganeh, M. Commerford, A. Haselbacher, A. Pedretti, and A. Steinfeld, "Stabilization of the outflow temperature of a packed-bed thermal energy storage by combining rocks with phase change materials," *Applied thermal engineering*, vol. 70, no. 1, pp. 316-320, 2014.

[125] H. Peng, R. Li, X. Ling, and H. Dong, "Modeling on heat storage performance of compressed air in a packed bed system," *Applied energy*, vol. 160, pp. 1-9, 2015.

[126] D. Gvozdenac, B. G. Urošević, C. Menke, D. Urošević, and A. Bangviwat, "High efficiency cogeneration: CHP and non-CHP energy," *Energy*, vol. 135, pp. 269-278, 2017.

[127] A. Verbruggen, "The merit of cogeneration: Measuring and rewarding performance," *Energy Policy*, vol. 36, no. 8, pp. 3069-3076, 2008.

Appendix

A.1 Compressor efficiency

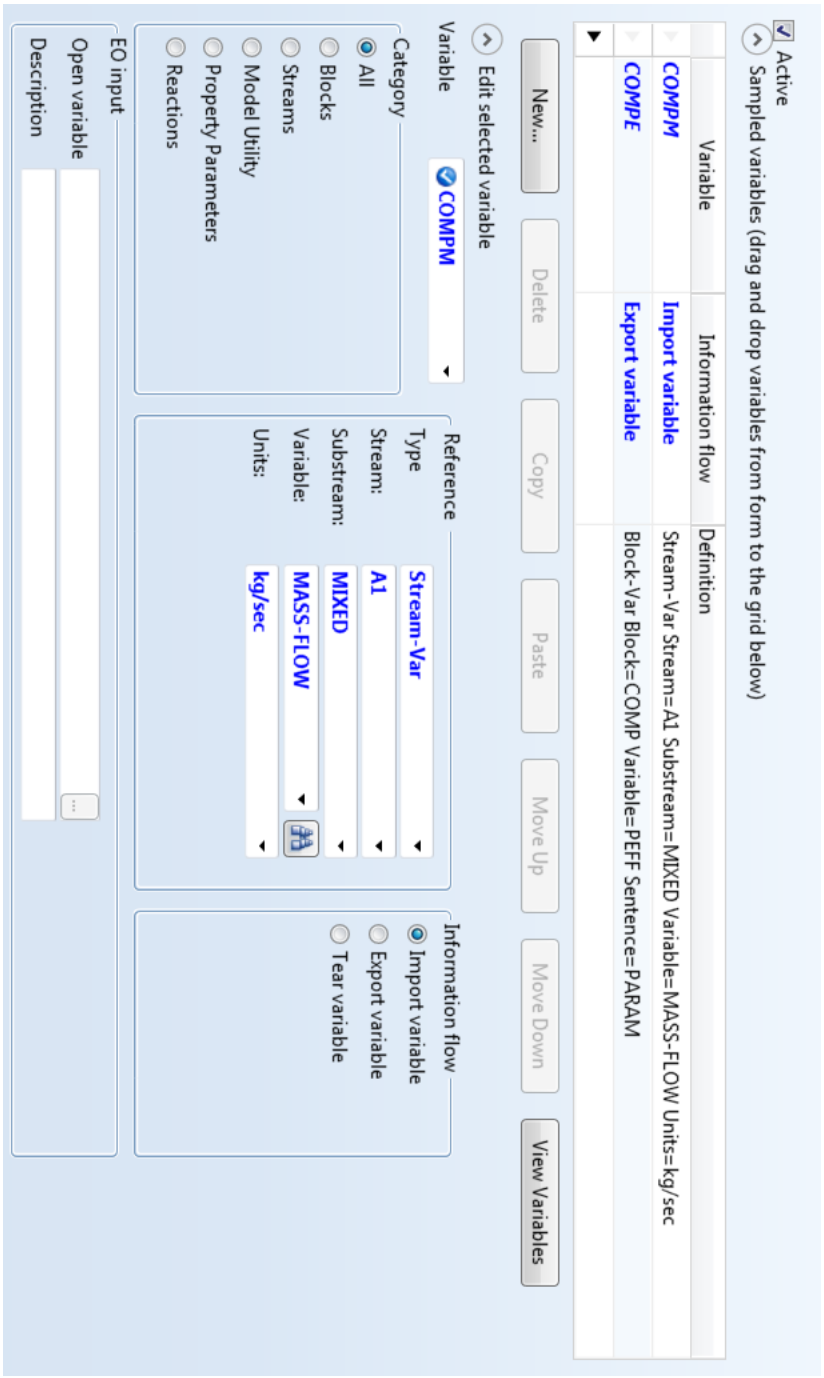

Figure A.1: Define import and export variables.

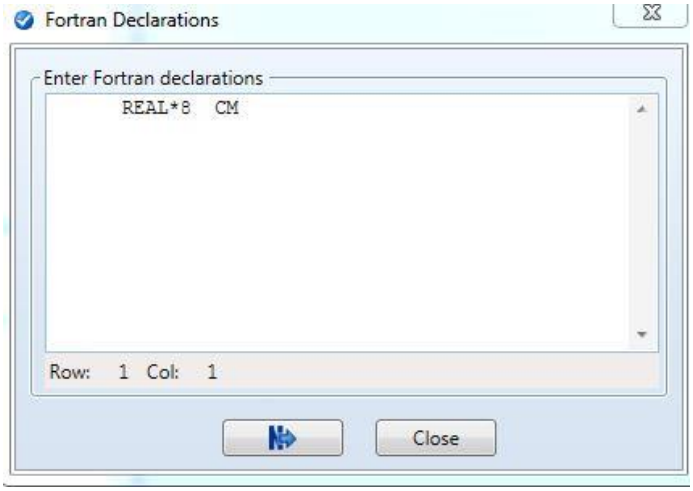

Figure A.2: Define parameter.

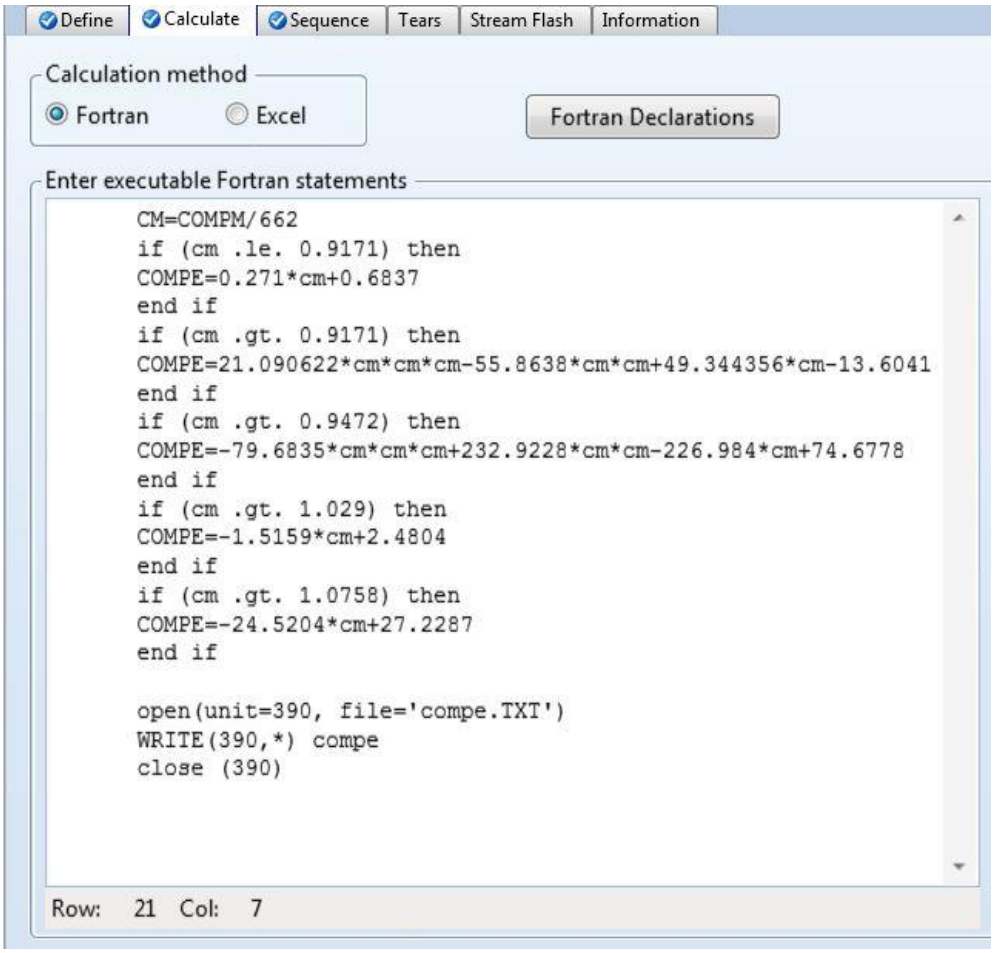

Figure A.3: Fortran code in calculator.

A.2 Define tear variables and heat exchanger model

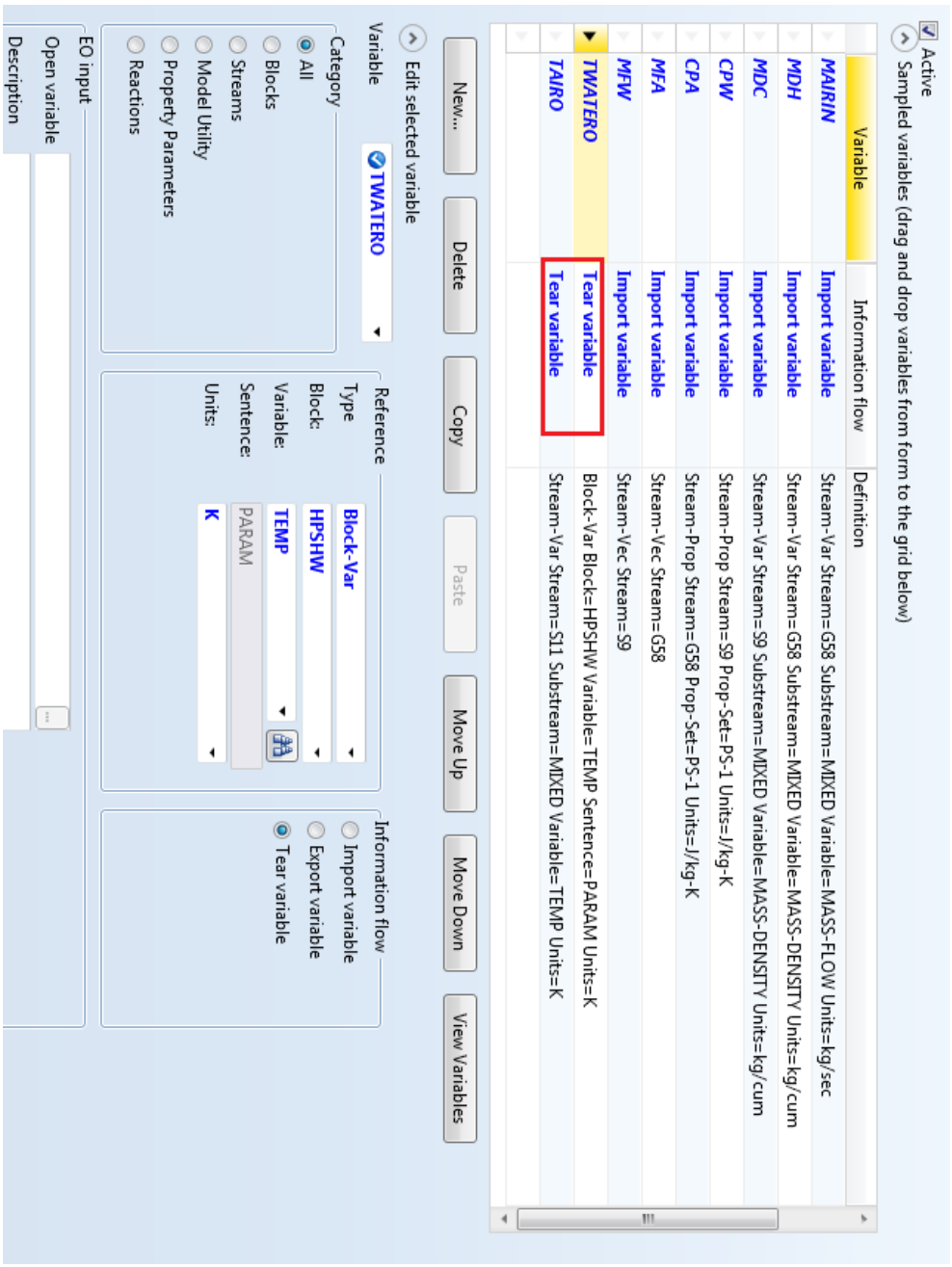

Figure A.4: Define tear variables

This is the Fortran code for heat exchanger model

```
      n=15
      rhowater=MDC
      cpwater=CPW
      rhoair=MDH
      cpair=CPA
      khex=800*( MWATERIN /84)**0.7
      Atot=1000
      A=Atot/n
      Vtot=30
      V=Vtot/n
      dx=0.01
      nu=8
      DO j=1,n+1
      T(j)=TWATERIN
      END DO
      DO j=n+2,2*n+2
      T(j)=TAIRIN
      END DO
      open (unit=10, file ='C4HPSH.txt')
      read(10,*) T
      close (10)
      T(n+1)=TWATERIN
      T(n+2)=TAIRIN
      YA(1)=MFA(1)/MFA(nu+1)
      YA(2)=MFA(2)/MFA(nu+1)
      YA(3)=MFA(4)/MFA(nu+1)
      YA(4)=MFA(5)/MFA(nu+1)
      YA(5)=MFA(6)/MFA(nu+1)
      IDXA(1)=1
      IDXA(2)=2
      IDXA(3)=4
      IDXA(4)=5
      IDXA(5)=6
      IDXW(1)=4
      KDIAG=4
      KBASE=1
      KPHI=3
      KH=3
      KS=3
      KV=3
      NN=5
      NW=1
      PA=MFA(nu+3)
      PW=MFW(nu+3)
      MFAA=MFA(nu+1)
      DO J=1,100
      DO i=1,n
      TW=T(i)
      PW=MFW(nu+3)-(n-i+1)*5000/15
      IDXW(1)=4
      call PPMON_VTHRM (TW,PW,NW,IDXW,NBOPST,KDIAG,KBASE,KPHI,KH,KS
     +,KG,KV,PHIW,H,S,G,VV,DPHIW,DH,DS,DG,DV,KER)
      cpwater=DH(1)*MFW(nu+1)/MWATERIN
      rhowater=18.015/VV(1)
```

```
  B=1/(rhowater*cpwater*V)
  dT(i)=B*(cpwater*MWATERIN*(T(i+1)-T(i))+khex*A*(T(i+n+2)-T(i)))
  T(i)=T(i)+dT(i)*dx
 end do
 OPSETT='PR-BM'
 HENRYY=''
 CHEMM=''
 ITRUEE=1
 FREEWW='STEAMNBS'
 ISOLUU=3
 CALL PPUTL_PPSWOP (OPSETT,HENRYY,CHEMM,ITRUEE,FREEWW,
+ISOLUU, IERRR)
 call PPUTL_GOPSET (NBOPSTT,NAMEE)
 DO i=n+3,2*n+2
 TA=T(i)
 YA(1)=MFA(1)/MFA(nu+1)
 YA(2)=MFA(2)/MFA(nu+1)
 YA(3)=MFA(4)/MFA(nu+1)
 YA(4)=MFA(5)/MFA(nu+1)
 YA(5)=MFA(6)/MFA(nu+1)
 IDXA(1)=1
 IDXA(2)=2
 IDXA(3)=4
 IDXA(4)=5
 IDXA(5)=6
 PA=MFA(nu+3)-(i-n+2)*200/15
 call PPMON_VMTHRM (TA,PA,YA,NN,IDXA,NBOPSTT,0,KBASE,KPHI,KH,KS
+,KG,KV,PHI,HMX,SMX,GMX,VMX,DPHI,CPMX,DSMX,DGMX,DVMX,KER)
 cpair=CPMX*MFAA/MAIRIN
 rhoair=28.5095/VMX
 BB= 1/(rhoair*cpair*V)
 dT(i)=BB*(cpair*MAIRIN*(T(i-1)-T(i))-khex*A*(T(i)-T(i-n-2)))
 T(i)=T(i)+dT(i)*dx
 end do
 END DO
 TWATERO=T(1)
 TAIRO=T(32)
 open(unit=60, file='c4hpsh.TXT')
 write(60,*) T
 close (60)
 open(unit=170, file='SSEEEDDE.TXT')
 write(170,*) T(1)
```

A.3 Air cavern model

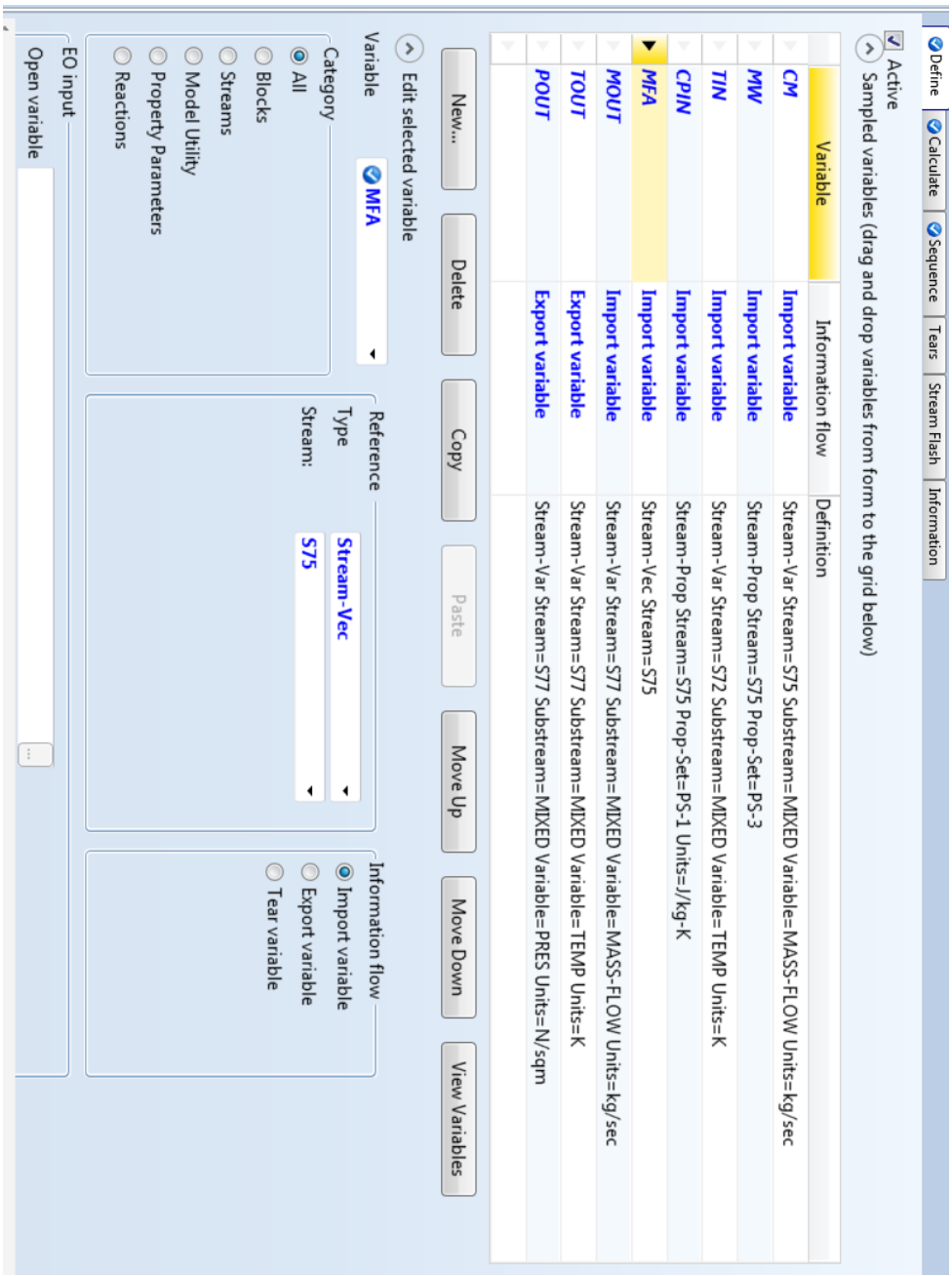

Figure A.5: Import and export variables of cavern model.

This is the Fortran code for cavern model

```
      nu=8
      R=8.314
      V=141000
      open(unit=300, file='CAESPT.TXT')
      read(300,*) PA,Tcav
      close (300)
      KBASE=1
      KPHI=3
      KH=3
      KS=3
      KV=3
      IDXA(1)=1
      IDXA(2)=2
      IDXA(3)=5
      IDXA(4)=6
      YA(1)=MFA(1)/MFA(nu+1)
      YA(2)=MFA(2)/MFA(nu+1)
      YA(3)=MFA(5)/MFA(nu+1)
      YA(4)=MFA(6)/MFA(nu+1)
      NA=4
      OPSETT='PR-BM'
      HENRYY=''
      CHEMM=''
      ITRUEE=1
      FREEWW='STEAMNBS'
      ISOLUU=3
      CALL PPUTL_PPSWOP (OPSETT,HENRYY,CHEMM,ITRUEE,FREEWW,
     +ISOLUU, IERRR)
      call PPUTL_GOPSET (NBOPSTT,NAMEE)
      call PPMON_VMTHRM (Tcav,PA,YA,NA,IDXA,NBOPSTT,0,KBASE,KPHI,KH,KS
     +,KG,KV,PHI,HMX,SMX,GMX,VMX,DPHI,CPMX,DSMX,DGMX,DVMX,KER)
      rho=MW/VMX
      cpcav=CPMX/MW
      R=R*1000/MW
      heff=25000*30/141000
      Tamb=313.15
      dT=((R*Tcav*(CM-mout)/V)-(CM*cpcav*(Tcav-Tin)/V)-heff*(Tcav-Tamb))
     + /(cpcav*rho-rho*R-R *(CM-mout)/V)
      dP=(R*Tcav*(CM-MOUT)/V)+rho*R*dT+dT* R *(CM-mout)/V
      PA=PA+dP
      Tcav=Tcav+dT
      Tout=Tcav
      Pout=PA
      open(unit=300, file='CAESPT.TXT')
      write(300,*) PA,Tcav
      close (300)
      open(unit=320, file='CAESRESULTS.csv')
      WRITE(320,*) PA,',',Tcav
```